The Philosophical Magazine

FIRST PUBLISHED IN 1798

A Journal of Theoretical Experimental and Applied Physics

Vol. 3 November 1958 No. 35
Eighth Series

£1 5s. 0d., plus postage
Annual Subscription £13 10s. 0d., payable in advance

Printed and Published by
TAYLOR & FRANCIS LTD
RED LION COURT, FLEET STREET, LONDON, E.C.4

THE PHILOSOPHICAL MAGAZINE

Authors wishing to submit papers for publication in the Journal should send manuscripts directly to the Publishers.

Manuscripts should be typed in *double* spacing on one side of quarto (8×10 in.) paper, and authors are urged to aim at absolute clarity of meaning and an attractive presentation of their texts.

References should be listed at the end in alphabetical order of authors and should be cited in the text in terms of author's name and date. Diagrams should normally be in Indian ink on white card, with lettering in soft pencil, the captions being typed on a separate sheet.

A leaflet giving detailed instructions to authors on the preparation of papers is available on request from the Publishers.

Authors are entitled to receive 25 offprints of a paper in the Journal free of charge, and additional offprints can be obtained from the Publishers.

The *Philosophical Magazine* and its companion journal, *Advances in Physics*, will accept papers for publication in experimental and theoretical physics. The *Philosophical Magazine* publishes contributions describing new results, letters to the editor and book reviews. *Advances in Physics* publishes articles surveying the present state of knowledge in any branch of the science in which recent progress has been made. The editors welcome contributions from overseas as well as from the United Kingdom, and papers may be published in English, French and German.

Observations of K⁻-Meson Interactions in Nuclear Emulsion†

By G. B. Chadwick, S. A. Durrani, P. B. Jones,
J. W. G. Wignall and D. H. Wilkinson
Cavendish Laboratory, Cambridge, and
Clarendon Laboratory, Oxford

[Received June 28, 1958]

Abstract

23·6 metres of K⁻-meson track in nuclear emulsion have yielded unbiased samples of 815 absorptions at rest and 106 in flight. The corresponding interaction mean free path is $21{\cdot}5^{+2{\cdot}3}_{-1{\cdot}9}$ cm for K⁻-mesons of energy below 90 Mev. Observations are reported on the disintegration stars themselves and on the charged hyperons produced. It is in particular noted that the angular correlation between hyperon and pion in two-pronged stars is closely that expected for a system without any nuclear interaction in the final state. It is shown that this and other aspects of the situation are most simply explained if the K⁻-meson is absorbed in the tenuous outer surface of the nucleus from a high Bohr orbit according to the model of Jones, and is not absorbed uniformly throughout the nuclear volume as is usually assumed. This surface absorption model allows of a strong hyperon–nucleon interaction such as appears to be indicated by a variety of other evidence and which would be inconsistent with the volume absorption model.

§ 1. Introduction

Investigations so far indicate that the K⁻-meson interacts with nuclear matter by two distinct processes : absorption by one nucleon with the production of a hyperon and a π-meson; and secondly, absorption by two nucleons which have high relative momentum owing to correlations in the nuclear ground state wave function. Such interactions provide a source of information about the fundamental K⁻-meson interaction, and may also be used to study the properties of the capturing nucleus. Hornbostel and Salant (1956) have outlined the characteristics to be expected of K⁻-meson absorption, and they and many others (Alles *et al.* 1957 a, Bacchella *et al.* 1958, Barkas *et al.* 1957, Fry *et al.* 1957, Gilbert *et al.* 1957, Haskin *et al.* 1956, Hornbostel and Zorn 1958, and Lohrmann *et al.* 1958) have investigated the absorption of K⁻-mesons in nuclear emulsion. A body of work as yet unpublished has been presented at recent conferences (Dilworth 1957, Alles *et al.* 1957 b, Bhowmik *et al.* 1957, Hoang *et al.* 1957, and Webb *et al.* 1957).

Unfortunately the absorption reaction appears to be so complicated that only qualitative deductions can be made, and these must be based

† Communicated by the Authors. This work was begun at Cambridge and finished at Oxford.

on a particular model. It has, so far, usually been assumed that a slow K^--meson is initially captured by the electrostatic field of the nucleus and that it then cascades by electromagnetic transitions through a series of Bohr orbits until finally absorption by the nucleus occurs. One of the present authors (Jones 1958) has investigated such a mechanism and has concluded that the absorption probability, deduced from the observed K^--proton scattering and absorption cross sections, is so large that most of the K^--mesons will be removed from rather high circular Bohr orbits, the absorption taking place in the surface of the nucleus in a region of low nucleon density. However, evidence has been presented recently (Gilbert and White 1958), which seems to favour an absorption probability more uniform throughout the nucleus. It is important to be able to choose the better of the two models, viz. surface or volume absorption.

Owing to the scarcity of statistically significant data on K^--meson interactions, we felt it advisable to make a completely systematic study of K^--meson capture stars in nuclear emulsion in order to obtain the widest variety of information. By finding K^--meson tracks where they enter the emulsion stack and following them until they are ultimately absorbed we obtain an unbiased selection of stars, as well as a value for the mean free path of K^--mesons in emulsion. These stars are an abundant source of hyperons some of whose characteristics can be studied. The importance of the branching ratios and angular correlations of the decay products is already well known.

In § 2, the experimental procedures used to find and examine the K^--meson interactions are described. The determination of the mean free path for K^--mesons in nuclear emulsion, the characteristics of K^- capture stars and observations on the interaction and decay of the Σ-hyperons produced are all described in § 3. The results obtained are discussed in § 4. In particular, it is shown that the observed Σ and π production angular correlation in the laboratory system of coordinates for 2-prong stars having a $\Sigma^{\pm}$-hyperon, a $\pi^{\pm}$-meson and no visible nuclear excitation, provides strong evidence for the surface absorption model. The consistency of the model, and the form of the effective nucleon momentum distribution it predicts for K^--meson absorption by a heavy nucleus receive some discussion. The relative production of Σ^--hyperons in the absorption of K^--mesons by bound neutrons and protons is determined.

§ 2. Experimental Details

A stack of 125 sheets of 400 micron thick Ilford G.5 nuclear photographic emulsion, 15 × 15 cm, was exposed to the September 1956 K^- beam of the Bevatron at the Berkeley Radiation Laboratory of the University of California. This beam was almost completely separated from π^--meson contamination by an energy degrader which reduced the K^- momentum

from 430 to 300 MeV/c and left only μ^--mesons of the latter momentum, after a second momentum analysis. The integrated K^- and μ^- meson fluxes were 70 and 2×10^5 per cm^2 respectively.

In order to make a completely unbiased selection of K^--meson capture stars and interactions in flight, and to obtain a value for the mean free path in nuclear emulsion, tracks having a normalized blob density in the range 2·1 to 2·8 were picked up near the beam entrance edge of the stack and followed in until some interaction occurred. All K^--mesons coming to rest, including zero prong stars, were then identified by a comparison of range with initial grain density. Interactions in flight were identified by multiple scattering versus grain density measurements close to the star. In this way the energy of the K^--meson at the point of interaction was obtained.

The stars were analysed by following to rest all prongs with normalized blob density $\geqslant 2{\cdot}0$. This limit corresponds to a proton energy of 175 MeV and to a Σ hyperon energy of about 220 MeV. The minimum plateau blob density in the stack was in the range 14–16 blobs per 100 microns only, and so it was difficult and in many cases impossible to follow minimum ionizing tracks ; further, such tracks are very likely to leave the stack. Consequently no systematic attempt was made to obtain a π-meson energy spectrum or charge ratio.

Each K^--meson ending was examined carefully for minimum ionizing tracks, as were the endings of those prongs followed. With such a low minimum blob density, it was impossible to estimate the scanning loss for fast π-mesons. The frequency of π-meson emission from our K^--meson stars is close to the generally accepted value but the number of single prong stars in flight may be rather low. We have avoided estimating any quantities which require a knowledge of the efficiency for detecting minimum ionizing tracks.

Systematic identification of zero prong Σ^--hyperon capture stars by Auger electron emission was not possible because of a heavy slow electron contamination of the stack. Decays of Σ^+-hyperons in flight to protons were ascertained to be kinematically consistent with the momentum of the decaying particle as determined by grain density measurement.

§ 3. Results

3.1. *The Mean Free Path and Related Matters*

The interaction mean free path of K^--mesons in nuclear emulsion, found from events occurring along 23·56 metres of K^--meson track scanned, is shown in table 1. The 110 interactions are divided into three groups according to the K^- energy at interaction. For this determination, all possible decays in flight (stars with one light prong and no sign of nuclear excitation), and interactions with free protons were excluded. Inelastic scatters on nuclei, however, were included in the reaction cross section.

Table 1. The Mean Free Path of K^--mesons in Nuclear Emulsion is Shown as a Function of Energy

Energy interval	5–30	30–60	60–90 MeV
Track length	430	1070	856 cm
No. of absorptions	18	46	42
No. of inelastic scatters	0	1	3
Mean free paths	$22{\cdot}8^{+7{\cdot}2}_{-4{\cdot}5}$	$22{\cdot}8^{+3{\cdot}9}_{-2{\cdot}9}$	$19{\cdot}0^{+3{\cdot}2}_{-2{\cdot}4}$ cm
Overall mean free path $21{\cdot}5^{+2{\cdot}3}_{-1{\cdot}9}$ cm			

In rejecting 11 interactions in flight with only one light prong, we have probably rejected some true interactions. Since 4·4% of all K^- capture stars have one light prong only, the number of true interactions rejected could well be 5 in the present case. However, the length of track scanned corresponds to a proper time of $1{\cdot}9 \times 10^{-7}$ sec, and so we would expect to see about 14 decays in flight if we accept the lifetime of the K^--meson to be $1{\cdot}3 \times 10^{-8}$ sec as reported at the Venice–Padua Conference. These numbers are not inconsistent but may suggest some scanning bias against finding the very fastest particles. This has little effect on the evaluation of the mean free path, and the resulting figure of $21{\cdot}5^{+2{\cdot}3}_{-1{\cdot}9}$ cm is in good agreement with $23{\cdot}4 \pm 0{\cdot}7$ cm, a figure representing the weighted average of the results referred to in § 1†.

Only one elastic scatter, and no absorptions of fast K^--mesons, were seen on free protons. Such a result is not inconsistent with an average cross section for elastic scattering on protons of 40 mb (Alles *et al.* 1957 a, Bhowmik *et al.* 1957, and Glasser *et al.* 1958), which would lead us to expect 3 such scatters.

Data on the inelastic scattering of the K^--mesons are presented in table 2.

Table 2. Inelastic Scattering of K^--Mesons on Emulsion Nuclei. The Data are for the Laboratory System of Coordinates

Incident K^--meson energy	Angle of scatter	Energy loss
87 MeV	47 degrees	48 MeV
84	17	24
80	104	61
35	97	8

† This mean free path is considerably shorter than the geometrical mean free path of about 30 cm. This is possible because the K^--meson can be absorbed on a *single* nucleon and so can be caught in the tenuous nucleon atmosphere outside the main body of the nucleus (cf. $\bar{p}$). Contrast the situation for the π-meson which must find *two* nucleons to be absorbed and which shows a mean free path close to the geometrical.

The fraction of inelastic scattering events is about 4% of all interactions in flight, in agreement with the figure of 1–4% quoted by Goldhaber (1957 a) at the Venice–Padua Conference. The energy loss is in general large as was first pointed out by Alles *et al.* (1957 a).

3.2. *Characteristics of K⁻-Meson Absorption Stars*

As the mechanism for the absorption of a fast K^--meson by a nucleus is very different from that for absorption of a captured K^--meson, we have divided the absorption stars found into these two classes. Their characteristics are presented in tables 3 and 4.

Table 3. Characteristics of 815 K^--Meson Capture Stars are Shown

No. of prongs	No. of stars	$\pi^\pm$	HF	All identified Σ^+	Σ^-	$\Sigma^\pm$	$\pi\Sigma^+$	$\pi\Sigma^-$
0	140	0	0	0	0	0	0	0
1	141	36	1	5	8	0	0	0
2	195	93	2	22	11	4	21	7
3	161	51	7	6	5	5	4	3
4	82	25	10	3	3	0	1	0
5	56	18	4	1	3	1	0	0
6	28	5	3	1	1	1	0	0
7	12	2	1	0	0	0	0	0
Totals	815	230	28	38	31	11	26	10
Percentages	100·0	28·2	3·4	4·7	3·8	1·4	3·2	1·2

The stars are divided into categories according to the total number of prongs. Columns 3 to 7 show the total numbers of $\pi^\pm$-mesons, hyperfragments and Σ-hyperons in each category. Columns 8 and 9 show the total number of stars in each category which have both a Σ-hyperon and a π-meson.

In these tables, an identified hyperon is one with charge determined by its mode of decay or interaction at rest, or in some cases by conservation of charge if the same star gave a π-meson which could be followed to rest. In a systematic study of 2-prong stars, Gilbert *et al.* (1957) found no cases in which both Σ-hyperon and π-meson from such stars had the same charge. This result is confirmed by our data for cases in which it was possible to identify the hyperon by its decay or interaction. The columns labelled $\Sigma^\pm$ contain the decays in flight, $\Sigma^\pm \rightarrow n + \pi^\pm$, for which the sign of the hyperon is unknown. The column labelled Σ^- contains Σ^- capture stars with $\geqslant 1$ prong only.

Non-mesonic hyperfragments could not generally be identified because of their short range, but in some cases charge conservation is useful in

Table 4. Characteristics of 106 Fast K^--Meson Absorption Stars are Shown. The Form of the Table is the Same as that of Table 3

No. of prongs	No. of stars	$\pi^\pm$	HF	All identified Σ^+	Σ^-	$\Sigma^\pm$	$\pi\Sigma^+$	$\pi\Sigma^-$
0	17	0	0	0	0	0	0	0
1	12	0†	0	0	1	0	0	0
2	25	7	1	0	3	0	1	2
3	20	6	1	2	1	0	1	0
4	16	1	1	0	1	0	0	0
5	8	1	1	0	0	0	0	0
6	4	1	0	0	0	0	0	0
7	4	0	1	0	0	0	0	0
Totals	106	16	5	2	6	0	2	2
Percentages	100·0	15·0	4·7	1·9	5·7	0·0	1·9	1·9

† See earlier comment in discussion of mean free path.

distinguishing between Σ^--hyperon capture stars and true hyperfragments. Figure 1 shows a range distribution of all possible hyperfragments, and we conclude from this and the Σ^--hyperon energy spectrum of fig. 2 that no significant number of these ' hyperfragments ' are actually Σ^- capture stars.

Fig. 1

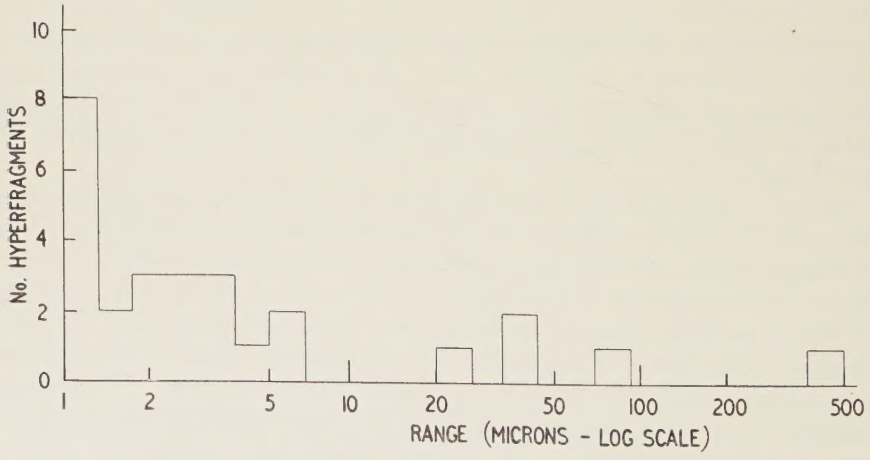

Range distribution of 28 hyperfragments emitted from 815 K^--meson captures at rest.

The probabilities for hyperon production which can be inferred from table 3 for capture stars, are 0·047 and 0·038 for identified Σ^+- and Σ^--hyperons respectively, rather lower than those usually quoted (see the references of § 1). Such a situation may result from larger scanning loss, or more strict criteria for identification of events. In order to check this, we can determine the branching ratio of the Σ^+-hyperon decay. The best estimate will be that determined from Σ^+ decays at rest. The ratio $(n\pi^+)/(p\pi^\circ) = 13/10$. This ratio is consistent with the figure of $1{\cdot}15 \pm 0{\cdot}29$ derived from the hydrogen bubble chamber data (Goldhaber 1957 b) and we feel that this is an indication that scanning losses will not invalidate conclusions drawn from the present investigation†.

From table 3 it is seen that the ratio of the number of stars having both a Σ^+-hyperon and a π^--meson to the total number of stars with Σ^+-hyperons is $26/38 = 0{\cdot}68$, whereas the proportion of all capture stars having $\pi^\pm$-mesons is 0·28. An approximate comparison of these figures is possible if we assume that about 15% of all K^- absorptions occur through the two-nucleon mechanism (see later), and that the nucleus is self-conjugate and the interactions charge independent. Using the theorem of Watson (1952, eqns. 20–22), it is seen that the average escape probability for $\pi^\pm$-mesons from all capture stars is about 0·50. This figure includes the scanning loss and takes into account both Σ- and Λ°-hyperon production. The difference between these two figures, though hardly statistically significant, can be understood using either the surface or the volume absorption model if the absorptions leading to the $\Sigma\pi$ class of events occur further from the centre of the nucleus than in the average case.

The energy spectra of the Σ-hyperons emitted from the K^- capture stars are shown in fig. 2. The energy spectra for Σ^+, Σ^- and $\Sigma^\pm$-hyperons are shown in parts (*a*), (*b*) and (*c*) respectively. A fairly clear group of high energy hyperons appears above 60 MeV (see fig. 2), which can be taken as evidence for the capture of K^--mesons by two nucleons. This interpretation is also suggested by the fact that only one of these fast hyperons is accompanied by a π-meson. The lower energy hyperons will then result from the single nucleon absorption process with a small contribution from the two nucleon process owing to scattering of the hyperons by the residual nucleus. In the absence of knowledge of the hyperon–nucleon cross sections we can only assume that such a contribution is small; consequently we infer that the ratio of two-nucleon to single-nucleon processes producing escaping hyperons is $0{\cdot}14 \pm 0{\cdot}05$.

Σ^+- and Σ^--hyperons are scattered and absorbed equally in a self-conjugate nucleus if the interactions are charge symmetric. In this case, as pointed out by Gilbert *et al.* (1957), the spectra of figs. 2 (*a*) and 2 (*b*) should

† No Dalitz electron–positron pairs were observed, although from 815 stars we would expect about 3 π°-mesons to have decayed in this way. However, no case of such a pair has been reported by other groups from a total of several thousand K^- stars, indicating that the apparent non-occurrence of this mode may be significant.

be displaced in opposite senses by the Coulomb potential of the nucleus. The total shift of the two spectra will then be approximately twice the average Coulomb potential V_C effective in the region of capture. Such a shift is obvious in the figures, and leads to an estimate of this Coulomb potential of $V_C \simeq 6 \pm 4$ Mev, in agreement with Gilbert *et al.*

Fig. 2

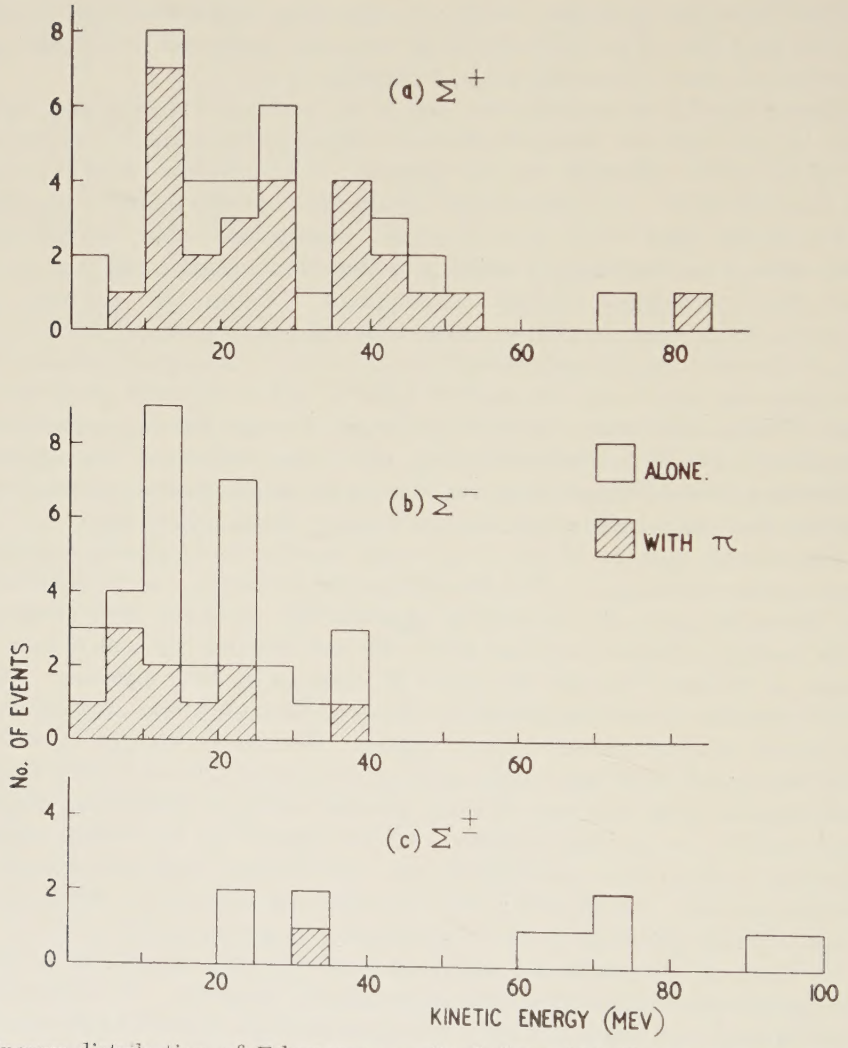

Energy distribution of Σ-hyperons emitted from 815 K⁻-meson captures at rest. (*a*) Identified Σ^+-hyperons ; (*b*) identified Σ^--hyperons ; (*c*) Σ-hyperon mesic decays in flight, unidentifiable charge. Cross hatching indicates emission in association with a π-meson.

Figure 3 shows the distribution of the angle χ between the initial directions of the hyperons and π-mesons from capture stars with no visible prongs other than these. In the histogram, we have distinguished between the contributions from positive and negative hyperons, but since the origin of the correlation is almost entirely kinematical they appear on one diagram. The curves in the figure show distributions of χ which would be expected if the production of hyperons and π-mesons is isotropic in their centre of mass system, assuming two effective momentum distributions for the capturing proton and no interaction of either particle with the parent nucleus. The solid curve assumes a Gaussian momentum distribution for

Fig. 3

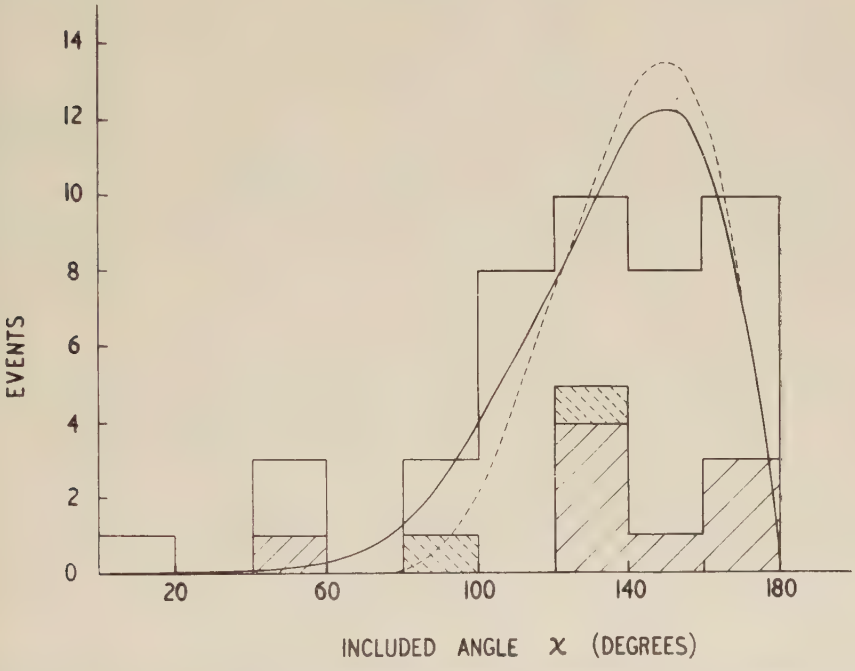

Distribution of the angle χ between initial directions of Σ-hyperons and π-mesons emitted together from 815 K^- captures at rest. Solid cross hatching indicates Σ^--hyperons, broken cross hatching, $\Sigma^\pm$, no hatching, Σ^+. The solid curve is the distribution predicted for a Gaussian momentum distribution for the capturing proton, the broken curve that for a Fermi gas distribution.

the proton with average kinetic energy 19 MeV (Brueckner *et al.* 1955); the broken curve, a Fermi distribution with cut-off at 20 MeV. As can be seen, the correlation is remarkably insensitive to the assumed distribution, and either fits the data rather well (the validity of assuming such types of effective nucleon momentum-distribution is discussed in § 4).

In fig. 4 is presented the energy spectrum of all protons greater than 50 MeV in energy from the 815 K -meson captures at rest. These protons are the result of π-meson absorption and of the two nucleon capture process. There do not appear to be any distinct groups, but the spectrum is given for general interest.

Fig. 4

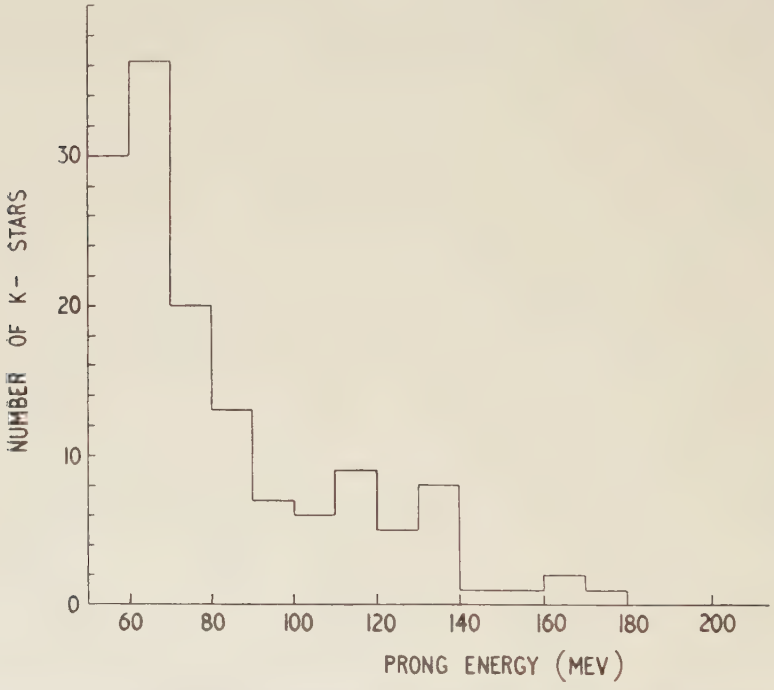

Energy distribution of all protons of energy greater than 50 MeV emitted from 815 K^--meson captures at rest.

3.3. *Characteristics of the* Σ*-hyperons*

The decay branching ratio $(n\pi^+)/(p\pi^\circ)$ of the Σ^+-hyperon was estimated from our data in the preceding subsection to be 1.3.

The lifetimes of the hyperons, and their mean free path for interaction and scattering are so sensitive to scanning biases and so dependent on details of interpretation that we do not consider nuclear emulsion a reliable tool for their estimation in quantitative terms.

It is possible to search for non-invariance of the Σ-hyperon decay interaction under the operations of parity and of charge conjugation, as the effect sought should be independent of scanning biases. We must look for an asymmetry in the emission of π-mesons with respect to the direction of polarization of the hyperon. A strong asymmetry has been observed for Λ°-hyperons in bubble chambers (Feld 1957), but not for

charged Σ-hyperons. Gatto (1957) has suggested that the capture of K⁻-mesons by nuclei may produce polarized hyperons because the Fermi motion of the nucleons within the nucleus can provide a preferred direction to define a polarization. In 2-prong stars with only a hyperon and a π-meson visible, the direction of motion of the capturing proton is defined by the momenta of the hyperon and meson. Thus any polarization of the hyperon will be perpendicular to the plane defined by the initial directions of the hyperon and the meson, provided that parity is conserved in the strong hyperon-producing interaction. An asymmetry in the direction of the decay π-meson owing to parity violation in the decay process will therefore occur about the plane determined by the Σ–π production.

In presenting the results of these measurements, we use the convention

$$\cos\omega' = \frac{(\mathbf{P}_\Sigma \wedge \mathbf{P}_\pi) \cdot \mathbf{P}_{\pi D}}{|\mathbf{P}_\Sigma \wedge \mathbf{P}_\pi \cdot \mathbf{P}_{\pi D}| \sin\chi}$$

as suggested by Smith and Inman (private communication). $\mathbf{P}_\Sigma$ and $\mathbf{P}_\pi$ are the initial momenta in the laboratory system of the associated Σ-hyperon and π-meson respectively, while $\mathbf{P}_{\pi D}$ is the initial momentum of the π-meson from the decay of the Σ-hyperon in the hyperon centre of mass system. Table 5 shows the distribution of this angle.

Table 5. The Distribution of $\cos\omega'$ is Shown for the Different Decay Modes at Rest (r) and in Flight (f)

	$\cos\omega' > 0$	$\cos\omega' < 0$
$\Sigma^+ \to p + \pi^\circ$ (r)	3	3
$\Sigma^+ \to p + \pi^\circ$ (f)	7	7
$\Sigma^+ \to n + \pi^+$ (r)	7	4
$\Sigma^\pm \to n + \pi^\pm$ (f)	4	2

It is important to note that failure to observe an asymmetry in ω' may well be attributable to a lack of polarization of the Σ-hyperons with respect to the plane of production. Such polarization could not occur for an s-state capture of the K⁻-meson by the proton in the nucleus and the lack of asymmetry could be considered to be evidence for this possibility. In such a case, the suggestion of Treiman (1956), that the spin of the Σ-hyperon may be investigated by looking for an anisotropy in the direction of the decay π-meson (in the hyperon centre of mass system) with respect to the initial hyperon direction, may be expected to be valid. This latter angle, θ', may be also investigated for an asymmetry about $\theta' = 90^\circ$ which

would possibly occur if the parity doublet theory of Lee and Yang (1956) were correct. The distribution of $\cos\theta'$ found for all hyperons is shown in table 6.

Table 6. The Distribution of $\cos\theta'$ is Shown. $\cos\theta'$ is Divided into Intervals of 0·500

$\cos\theta'$	1·0–0·5	0·5–0·0	0·0–(−0·5)	−0·5–(−1·0)
$\Sigma^+\rightarrow p+\pi^\circ$ (r)	4	4	0	4
$\Sigma^+\rightarrow p+\pi^\circ$ (f)	6	2	5	6
$\Sigma^+\rightarrow n+\pi^+$ (r)	3	5	3	6
$\Sigma^\pm\rightarrow n+\pi^\pm$ (f)	1	6	3	2

Fig. 5

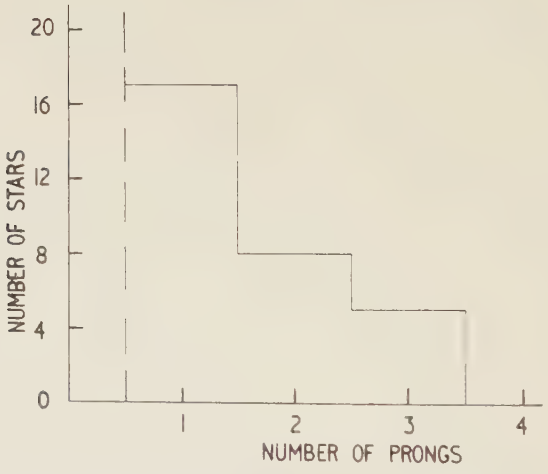

Prong number distribution from 30 Σ^--hyperon captures at rest. No estimate of the number of zero prong stars is made.

Finally, the Σ^--hyperon capture stars may be mentioned. For the reasons given in § 2 and in the discussion of § 4, we have not attempted to determine the number of zero prong capture stars; we merely record the characteristics of identified Σ^--hyperon stars. In fig. 5 the prong number distribution is shown. Figure 6 shows the energy distribution for particles of charge $Z=1$ (assumed to be protons) emitted from the capture stars.

Fig. 6

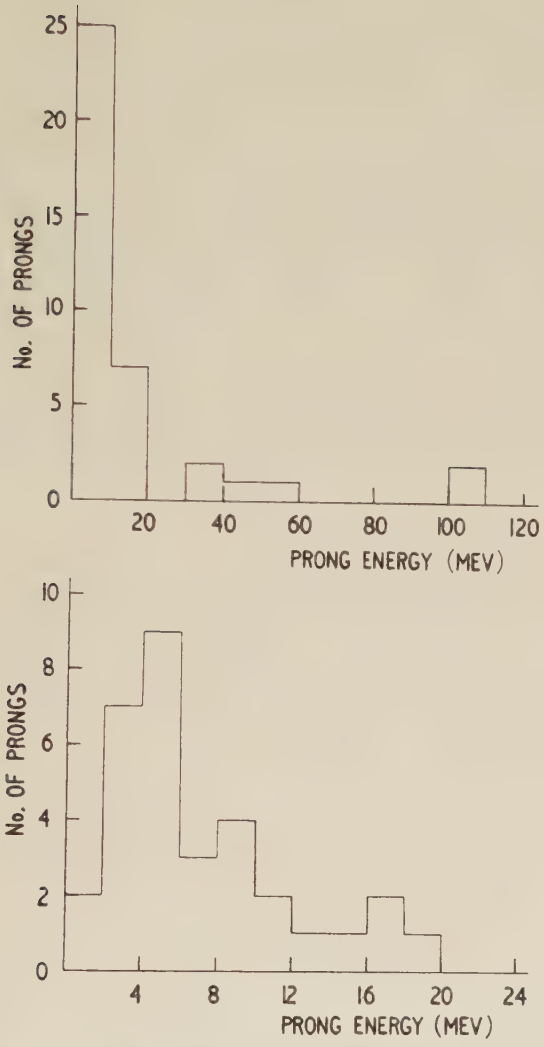

Energy distribution for particles of $Z=1$ (assumed to be protons) emitted from 30 Σ^--hyperon capture stars.

§ 4. Discussion

A problem much discussed in the literature is the determination of the branching ratios for production of the various hyperons in the K^--meson absorption process. The difficulty lies in the identification of Σ^--hyperons by their endings, an unknown fraction of which produce zero prong stars. A further complication is the ordinary scanning loss for all types of events, especially those involving the emission of fast $\pi^{\pm}$-mesons. We can estimate the ratio, S, of the number of Σ^--hyperons produced by the reaction

$$K^- + n \rightarrow \Sigma^- + \pi^0 \quad \ldots\ldots (1)$$

to the number produced by

$$K^- + p \rightarrow \Sigma^- + \pi^+ \quad \ldots\ldots (2)$$

with some rigour by making scanning loss (due both to individual observers and to zero prong events) cancel out, and also any correlation in direction of emission of the particles.

Let $N(+)$ be the number of Σ^+-hyperons seen, $N(+\pi)$ the number of $\Sigma^+ + \pi^-$, $N(-)$ the number of Σ^-, $N(-\pi)$ the number of $\Sigma^- + \pi^+$. For each particle, i, we can define a quantity $x(i)$, being the probability of escape of particle i from the nucleus, and another, $s(i)$, the scanning efficiency for that particle. These last quantities may be found through observations of the reaction

$$K^- + p \rightarrow \Sigma^+ + \pi^- \quad \ldots\ldots (3)$$

which, if we exclude those from the two nucleon interaction by their energy, is the only source of Σ^+-hyperons. The number of Σ^+-hyperons seen is then

$$N(+) = P(3)x(\Sigma^+)s(\Sigma^+)$$

and

$$N(+\pi) = P(3)x(\Sigma^+)s(\Sigma^+)x(\pi^-)s(\pi^-)F(+)$$

where $P(3)$ is the probability of reaction (3) occurring and $F(+)$ is a factor depending on the angular correlation of the hyperon and π-meson in the laboratory system of coordinates. The last factor allows for correlations which would be important if K^--meson absorption takes place in the nuclear surface. Thus

$$x(\pi^-)s(\pi^-)F(+) = N(+\pi)/N(+).$$

Similar considerations of reactions (1) and (2), which occur with probabilities $P(1)$ and $P(2)$, lead to

$$\frac{N(-\pi)}{N(-)} = \frac{P(2)x(\Sigma^-)s(\Sigma^-)x(\pi^+)s(\pi^+)F(-)}{[P(1)+P(2)]x(\Sigma^-)s(\Sigma^-)}.$$

We now assume that $x(\pi^-)s(\pi^-)F(+) = x(\pi^+)s(\pi^+)F(-)$, which is reasonable to the extent that π-meson interactions are charge symmetric, scanning losses for $\pi^\pm$-mesons are independent of their charge, and that the correlation is kinematic in origin. Combining these results we have

$$1 + P(1)/P(2) = N(+\pi)N(-)/N(+)N(-\pi) = 1 + S.$$

If the Σ-nucleon interaction is charge symmetric, it is easy to see that the contributions to $N(+)$ and $N(-)$ by charge exchange processes approximately cancel. The weighted mean value of S, compounded from the results of each individual observer, is $0{\cdot}9 \pm 0{\cdot}7$, which may be compared with the value $S = 0{\cdot}87$ calculated, assuming charge independence, from the results of the isotopic spin analysis of Alvarez *et al.* (1957) on the absorption of K^--mesons in a hydrogen bubble chamber. This figure takes into account capture by both light and heavy nuclei in the ratio 3/7,

and the fact that the heavy nuclei have $N \neq Z$. As Alvarez *et al.* point out, however, in this case it is not known whether the absorption takes place from the 1s or 2p Bohr orbit, and so the comparison could be meaningless. The value for S found by Dilworth (1957) for all nuclear emulsion data available at that time, and using similar methods is 0·6.

We now propose to discuss the results of § 3 which have a bearing upon the absorption of K$^-$-mesons by nuclei, and try to show that they favour the K$^-$ surface absorption model. As was mentioned in the introduction, the calculations of Jones (1958) indicate that absorption of K$^-$-mesons captured in Bohr orbits by the Coulomb potential of heavy nuclei should take place for well defined large orbital angular momenta, if these orbits are circular ($l = 4$ for Ag and Br; as low as $l = 2$ for the light elements). Experiments designed to observe x-rays from the K$^-$-meson electromagnetic transitions on this model should not show transitions involving Bohr orbits with angular momentum below about $l = 4$ for medium–heavy nuclei. In addition, the very short mean free path of K$^-$-mesons in nuclear matter implied by the scattering and absorption of fast K$^-$-mesons makes it *a priori* unlikely that any mechanism could introduce them far into the nuclear volume.

The probability of absorption at a distance r from the centre of the nucleus is approximately $P(r) = \text{const.}\ r^2 |\psi|^2 \rho(r)$, where ψ is the perturbed K$^-$ wave function and $\rho(r)$ is the nucleon density distribution. $P(r)$ has been calculated for two nuclei representative of light and heavy elements, for different values of the complex nuclear potential V, and for several different values of l†. The best estimate of V is $\text{Re}(V) = -20$ Mev, and $\text{Im}(V) = -50$ Mev. The resulting distributions are plotted for the bromide ($l = 4$) and for carbon ($l = 2$) in fig. 7. We take $\rho(r)$ to be identical with the proton density distribution determined by high energy electron scattering experiments (Hofstadter 1956). V_c is the Coulomb potential. $P(r)$ has been plotted for the most likely set of the possible parameters because the result is insensitive to reasonable variations of these.

Absorption of the K$^-$-meson in a region relatively remote from the nucleus immediately explains the observed correlation displayed in fig. 3 between the directions of Σ-hyperons and π-mesons from capture stars: if the hyperons were produced inside the nucleus, the strong scattering to be expected of the hyperons would destroy the correlation. The relatively large probability of both hyperon and meson escaping the nucleus, suggested by the large proportion (0·68) of Σ^+-hyperons seen with π^--mesons is also hard to understand on the basis of the volume absorption model. Finally, the absence of observed Σ^--hyperons in association with π^--mesons indicates that the charge exchange reaction

† The calculation of $P(r)$ was made by Mr. J. M. Charap of Trinity College, Cambridge, with the kind permission of Dr. M. V. Wilkes of the Cambridge University Mathematical Laboratory, using the EDSAC 2 digital computer. Details of such calculations will be published soon by Mr. Charap.

Fig. 7

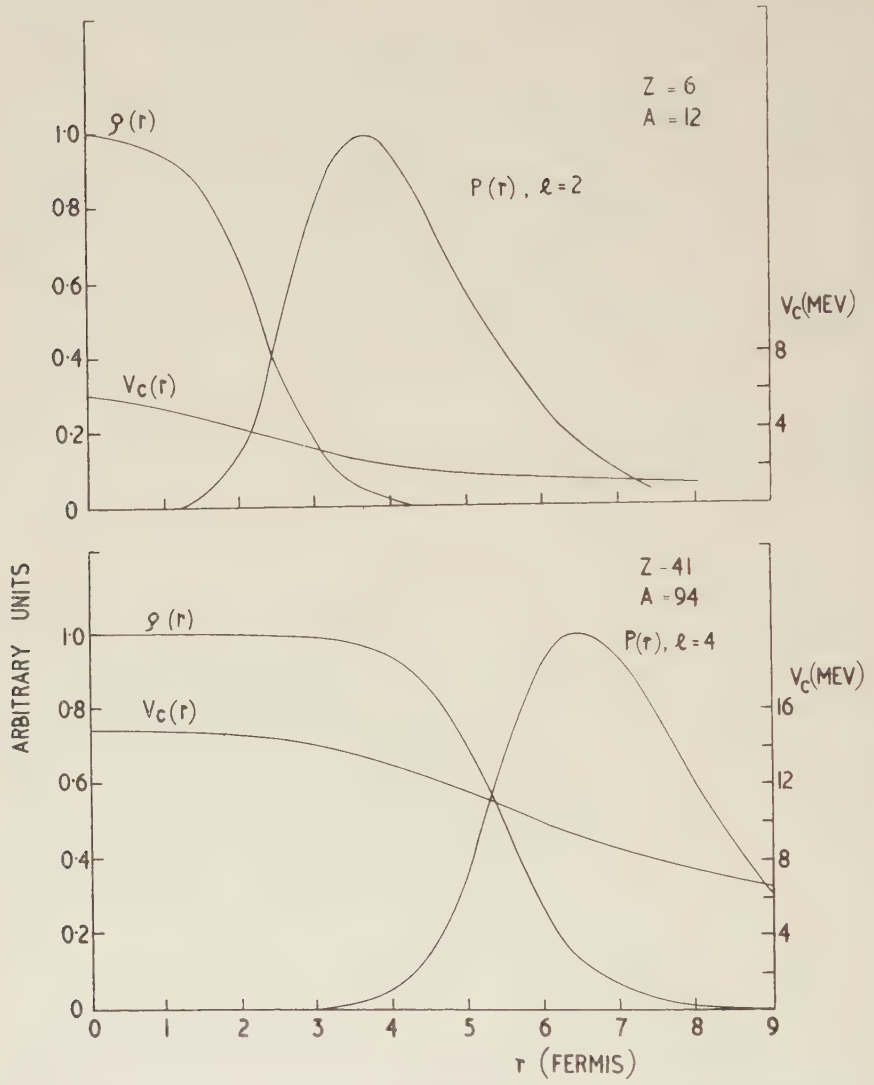

Plot of the nuclear matter density distribution $\rho(r)$, K^--meson capture probability $P(r)$ from the most probable Bohr orbit, and the Coulomb potential V_C, against the distance, r, from the centre of the nucleus, for two nuclei representative of nuclei of photographic emulsion. See text for other parameters used in the calculations.

$\Sigma^\circ + n \rightarrow \Sigma^- + p$ does not contribute appreciably to the number of observed Σ^--hyperons as we should expect if the absorption took place inside the nucleus.

The only alternative explanation of these effects seems to be that the mean free path in nuclear matter of normal density for scattering and

absorption of Σ-hyperons is of the order of the nuclear radius. The estimate of Gilbert and White (1958) is that a nuclear mean free path for absorption of $5^{+7}_{-2} \times 10^{-13}$ cm (cross section 11^{+7}_{-6} mb) would be required to reproduce the observed escape probabilities. Information on this point is rather scarce, but preliminary data have been reported (Venice–Padua Conference 1957) on scattering and absorption of fast Σ-hyperons which indicate at least geometrical cross sections for interaction. The existence of a Σ^+-proton compound, recently reported by Baldo-Ceolin *et al.* (1957), with small binding energy, would imply a fairly large zero energy scattering length in either the triplet or the singlet spin state and consequently a large hyperon–nucleon scattering cross section at low energies. In nuclear matter, of course, the effective scattering cross section would be decreased by the effect of the exclusion principle. Results obtained with the Berkeley hydrogen bubble chambers (private communication from L. W. Alvarez) also indicate a large hyperon–nucleon cross section. A mean free path of greater than about 5×10^{-13} cm for Σ-hyperons in nuclear matter, such as is probably required to make the results consistent with the hypothesis of volume absorption, therefore seems rather improbable.

It is possible to reconcile the actual observed abundance of K^--meson absorption products with the surface absorption model. Using the π-meson interaction parameters given by Frank *et al.* (1956), and assuming isotropic emission of π-mesons from points of origin distributed through the nuclear surface with probability $P(r)$ shown in fig. 7, the escape probability of such π-mesons is found to be 0·66. If 85% of K^--meson absorptions produce π-mesons (two-thirds of which are charged), we should observe 37% of absorption stars to have π-mesons. This is quite close to the generally accepted experimental figure, of a little over 30%, if a reasonable scanning loss is assumed. For Σ^+-hyperons, the escape probability will be about 0·5 if the nucleus is very black to them, while for Σ^--hyperons, the Coulomb field will capture about 30% (the fraction of Σ^+-hyperons with energy $< 2V_C$) and the escape probability is reduced to about 0·3. Estimates of the Σ-hyperon production probabilities can be made using charge independence and the results of absorption of K^--mesons in hydrogen (see Jones 1958); and using these our model predicts that 6% of stars will yield Σ^+-hyperons and 12% Σ^--hyperons. These figures are consistent with experiment. Such very rough figures may well be misleading. We should like to point out, however, the simplicity of the assumption (strong hyperon–nucleus interaction) needed to reconcile all aspects of the experimental situation (χ-distribution, π and Σ abundances) with the surface absorption model, and to contrast this with the special and probably implausible assumptions demanded by the volume absorption model.

If further investigation confirms that the K^--meson absorption occurs in the surface of large nuclei†, it will be a reaction of rather unusual

† The same considerations of course apply to the absorption of stopped anti-protons.

properties. It will provide a tool for investigating the nature of dilute nuclear matter. It will also be complicated both by the fact that the K^--meson has high angular momentum, and that at the low relative momentum involved, the strongly exothermic part of the total reaction cross section should be proportional to $(k)^{-1}$ for s-state interaction with a free nucleon, where k is the centre of mass momentum. Both these factors modify the effective momentum distribution of the capturing nucleon. It can easily be shown, using the independent particle model of the nucleus, that the probability of absorption of a K^--meson by a nucleon with ground state wave function ϕ_i depends on the final state momentum K through a factor

$$K^2 \left| \int d^3\mathbf{r}_i \exp(-i\mathbf{K} \cdot \mathbf{r}_i) v \phi_k(\mathbf{r}_i) \phi_i(\mathbf{r}_i) \right|^2.$$

ϕ_k is the wave function of the captured K^--meson, and the interaction operator assumed is

$$H(\mathbf{r} - \mathbf{r}_i) = v\delta^{(3)}(\mathbf{r} - \mathbf{r}_i).$$

For the heavy nuclei, the K^--meson should, as we have remarked above, be absorbed from a state of high angular momentum. In this case, $\phi_k(\mathbf{r}_i) \simeq 0$ inside the nucleus, and there is no reason to expect that the effective momentum distribution will coincide with a nucleon momentum distribution found from the analysis of other high energy nuclear reactions occurring more uniformly throughout the nuclear volume. It may even be different for neutrons and protons considered separately.

Finally, we may remark on the difficulties involved in the interpretation of the other experimental data, particularly the energy spectrum of fast protons and the number of Σ^--hyperons emitted from the K^- capture stars. In the case of the protons with energy greater than 100 MeV, the different processes mentioned in § 3.2 contribute and it is certainly not correct to assume that only the protons produced by the absorption of a K^- by a nucleon pair are important. The determination of the number of zero prong Σ^- capture stars is difficult. One possible method would be to compare the distribution of the angle χ for those 2-prong stars which have no visible hyperon with the distribution for $\Sigma\pi$ stars shown in fig. 3. However, we regard this method as unreliable since at energies of more than about 10 MeV the direct interaction processes become important and it can no longer be assumed that the distribution in χ for protons will be isotropic: they will to some extent carry the memory of the direction of the hyperon or meson from which they originated.

In discussing the escape of the reaction products from the nucleus using an optical model, the surface interaction and the high angular momentum involved are both important. Because the interaction is in the nuclear surface, but close to the body of the nucleus, the escape probability is insensitive to the reaction cross section for geometrical reasons. Thus, exact calculation of the absorption branching ratio inside the nucleus by direct use of the results of Alvarez *et al.* (1957) would be questionable in the present case.

§ 5. Conclusion

We feel that the present data on K^--meson interactions in heavy nuclei indicate fairly clearly that absorption takes place in the nuclear surface. The simplicity of the assumptions needed to explain the data is a further point in favour of the model presented as compared to the complex and explicit assumptions needed to justify the volume absorption model. However, the model is so insensitive to the hyperon–nucleon interaction that little information on this point can be obtained from a study of K^--meson absorptions, and it must be investigated separately.

Acknowledgments

We are most grateful to Dr. E. Lofgren and to the staff of the Bevatron at the Radiation Laboratory of the University of California for enabling us to secure the exposure and particularly to Dr. W. H. Barkas whose group engineered the K^--meson beam; the help of Dr. H. H. Heckmann was particularly appreciated. We should also like to thank the William Waldorf Astor Foundation which supported the carrying out of the irradiation at Berkeley.

We would like to thank Mrs. L. M. Eisberg, who helped in the early stages of the experiment, and our scanners, Mr. M. A. Ali, Miss M. de la Cruz and Mrs. S. Heiseler for their work.

G. B. Chadwick, S. A. Durrani, P. B. Jones and J. W. G. Wignall wish to thank respectively the following bodies for grants: the Shell Petroleum Company; Gonville and Caius College, Cambridge and the Clarendon Laboratory, Oxford; the D.S.I.R.; and the Royal Commissioners for the 1851 Exhibition.

References

Alles, W., Biswas, N. N., Ceccarelli, M., and Crussard, J., 1957 a, *Nuovo Cim.*, **6**, 517; 1957 b, *Padua–Venice Conference Report*, II–56.

Alvarez, L. W., Bradner, H., Falk-Vairant, P., Gow, J. D., Rosenfeld, A. H., Solmitz, F. T., and Tripp, R. D., 1957, *UCRL preprint* 3775.

Bacchella, L., Berthelot, A., Bonnetti, A., Goussu, O., Levy, F., Rene, M., Revel, D., Sacton, J., Scarsi, L., Tagliaferri, G., and Vanderhaeghe, G., 1958, *Nuovo Cim.*, **8**, 215.

Baldo-Ceolin, M., Fry, W. F., Greening, W. D. B., Huzita, H., and Limentani, S., 1957, *Nuovo Cim.*, **6**, 144.

Barkas, W. H., Dudziak, W. F., Giles, P. C., Heckmann, H. H., Inman, F. W., Mason, C. J., Nickols, N. A., and Smith, F. M., 1957, *Phys. Rev.*, **105**, 1417.

Bhowmik, B., Evans, D., Falla, D., Fowler, G. N., Kamal, A. A., and Prowse, D. J., 1957, *Padua–Venice Conference Report*, II–45.

Brueckner, K. A., Eden, R. J., and Francis, N. C., 1955, *Phys. Rev.*, **98**, 1445.

Dilworth, C. C., 1957, *Proceedings of the 7th annual Rochester Conference* (New York: Interscience Publishers Inc.).

Feld, B. T., 1957, *Padua–Venice Conference Report*, XIX–14.

Frank, R. M., Gammel, J. L., and Watson, K. M., 1956, *Phys. Rev.*, **101**, 891.

Fry, W. F., Schneps, J., Snow, G. A., Swami, M. S., and Wold, D. C., 1957, *Phys. Rev.*, **107,** 257.
Gatto, R., 1957, private communication to F. M. Smith.
Gilbert, F. C., Violet, C. E., and White, R. S., 1957, *Phys. Rev.*, **107,** 228.
Gilbert, F. C., and White, R. S., 1958, *Phys. Rev.*, **109,** 1770.
Glasser, R. G., Seeman, N., and Snow, G. A., 1958, *Nuovo Cim.*, **7,** 142.
Goldhaber, G., 1957 a, *Padua–Venice Conference Report,* XIX–13 ; 1957 b, *Ibid.*, XIX–8.
Haskin, D. M., Bowen, T., and Schein, M., 1956, *Phys. Rev.*, **103,** 1512.
Hoang, T. F., Engler, A., and Kaplon, M. F., 1957, *Padua–Venice Conference Report,* II–48.
Hofstadter, R., 1956, *Rev. mod. Phys.*, **28,** 214.
Hornbostel, J., and Salant, E. O., 1956, *Phys. Rev.*, **102,** 502.
Hornbostel, J., and Zorn, G. T., 1958, *Phys. Rev.*, **109,** 165.
Jones, P. B., 1958, *Phil. Mag.*, **3,** 33.
Lee, T. D., and Yang, C. N., 1956, *Phys. Rev.*, **104,** 822.
Lohrmann, E., Nikolic, M., Schneeberger, M., Waloschek, P., and Winzeler, H., 1958, *Nuovo Cim.*, **7,** 163.
Smith, F. M., and Inman, F. W., 1957, private communication.
Treiman, S. B., 1956, *Phys. Rev.*, **101,** 1216.
Watson, K. M., 1952, *Phys. Rev.*, **85,** 852.
Webb, F. M., Iloff, E. L., Fetherstone, F. H., Chupp, W. W., Goldhaber, G., and Goldhaber, S., 1957, *Padua–Venice Conference Report,* II–69.

Ductile–Brittle Transition in Steels Irradiated with Neutrons†

By D. Hull and I. L. Mogford
Atomic Energy Research Establishment, Harwell

[Received July 18, 1958]

Abstract

The yield and fracture stresses of unirradiated and irradiated En2 steel have been measured at 20°, −78°, and −196°c. From the change in yield stress, σ_y (shear), with grain size, $2d$, the values of σ_i and k_y in a Petch type equation, $\sigma_y = \sigma_i + k_y d^{-1/2}$, have been determined. The term k_y is unaffected by irradiation to within 5% and σ_i increases at a rate approximately proportional to the cube root of the dose. The effect of irradiation on the grain size transition from ductile to brittle fracture has been determined experimentally at −196°c and estimated from the change in σ_i and the value of k_y for tests at −78° and 20°c. The results are in accord with the predictions of Cottrell's relation $(\sigma_i\ d^{1/2} + k_y)\ k_y = \beta\gamma\mu$ for the transition. The transition surface relating grain size, yield stress and temperature has been obtained.

§ 1. Introduction

Cottrell (1958) has recently developed a theory of brittle fracture which overcomes some difficulties of previous theories and accounts for the brittle cleavage of single crystals. In this theory it is proposed that the crack nucleus is formed at the junction of two intersecting {110} slip planes by the coalescence of dislocations on these planes:

$$\tfrac{1}{2}a[\bar{1}\ \bar{1}\ 1] + \tfrac{1}{2}a[1\ 1\ 1] \rightarrow a[001]. \qquad (1)$$

The new dislocation is a pure edge lying in the (001) cleavage plane and if further dislocations run into it a cleavage crack is formed with a length of the same order as the slip length. When the joint size of the crack and slip bands is greater than the Griffith value the crack will continue to grow and produce cleavage fracture, but if it is smaller than the Griffith value the crack will not grow beyond a limited size and will become blunted by plastic flow at its tip. A calculation of the critical size shows that in grains of diameter $2d$ the transition occurs when the relation

$$(\sigma_i d^{1/2} + k_y) k_y = \beta\gamma\mu \qquad (2)$$

is satisfied, where shear stress σ_i, grain diameter $2d$, and k_y are related to the shear stress for yield σ_y, by a Petch type equation

$$\sigma_y = \sigma_i + k_y d^{-1/2} \qquad (3)$$

β is a constant depending on the mode of deformation, being unity for uni-axial tension and one-third at the root of a plastic notch in hydrostatic tension, γ is the effective surface energy of the crack, and μ is the shear modulus.

† Communicated by the Authors.

The constant k_y is a measure of the stress required to operate dislocation sources and σ_i measures the stress opposing the motion of dislocations. Heslop and Petch (1956) have shown experimentally that σ_i can be divided into two terms

$$\sigma_i = \sigma_1 + \sigma_2 \quad . \quad . \quad . \quad . \quad . \quad . \quad . \quad . \quad . \quad (4)$$

here σ_2 is the resistance of the lattice itself, and σ_1, the hardening caused, for example, by impurities, precipitates, and other dislocations in the lattice.

For steels irradiated with neutrons, Churchman *et al.* (1957) have shown that hardening results from an increase in the frictional resistance σ_i. The results suggest that radiation hardening is caused by dispersed regions of radiation damage, such as clusters of point defects, that are sufficiently large to withstand thermally activated movements of dislocations.

Equation (2) shows that the transition will depend on grain size, mode of deformation, and yield stress which is sensitive to temperature and strain rate. In the present work σ_i and k_y have been measured for En2 steel at three testing temperatures after irradiation doses up to 9×10^{19} neutron cm^{-2}. The combined effect of grain size, temperature, dose and yield stress has been determined. Providing k_y is unaffected by irradiation the results can be used to check the validity of Cottrell's transition equation which predicts that if k_y and $\beta\gamma\mu$ are constant the product of $d^{1/2}$ and σ_i should be constant at a given transition temperature.

§ 2. Experimental

Specimens were machined from En2 steel with a composition given in table 1. Double shouldered Hounsfield type test pieces with a 1 in. parallel gauge length and 0·126 in. diameter were used. The yield and fracture stresses were measured at 20°, −78°, and −196°C in a hard beam

Table 1. Composition of En2 Steel

C %	Si %	S %	P %	Mn %	Ni %	Cr %	Mo %	Co %	Al %	N %
0·15	0·12	0·051	0·026	0·59	<0·15	<0·10	<0·15	<0·06	<0·02	<0·011

tensile machine with a strain rate of 10^{-2} per minute. An optical lever system magnified the beam deflection.

A range of ferrite grain sizes (300 to 2850 grains/mm^2) was obtained by heat treatment and all the specimens were tested in the annealed condition. The specimens were irradiated in the BEPO and Windscale graphite reactors. The positions in the pile were chosen such that the maximum flux in a temperature range 60–100°C was utilized. The specimens were irradiated to doses between 10^{18} and $9{\cdot}1 \times 10^{19}$ neutron cm^{-2}. The thermal

and epithermal fluxes were approximately equal and an estimated 10% of the epithermal neutrons have energies greater than 1 Mev.

§ 3. Variation of k_y and σ_i with Temperature and Irradiation Dose

In figs. 1–4 the lower yield stress and fracture stress results for three temperatures and after doses up to $9{\cdot}1 \times 10^{19}$ neutron cm^{-2} are summarized. For unirradiated specimens k_y and σ_i increase as the temperature of testing is reduced. The values, $k_y = 2{\cdot}89 \times 10^7$ c.g.s. units, $\sigma_i = 4{\cdot}48 \times 10^8$ dyne cm^{-2} at room temperature agree reasonably well with those of Cracknell and Petch (1955), i.e. $k_y = 2{\cdot}52 \times 10^7$ c.g.s. units, $\sigma_i = 3{\cdot}54 \times 10^8$ dyne cm^{-2} for En2 steel of similar composition. There is an approximately linear variation of k_y with temperature, $\partial k_y/\partial T = -8{\cdot}0 \times 10^4$ c.g.s. units.

Fig. 1

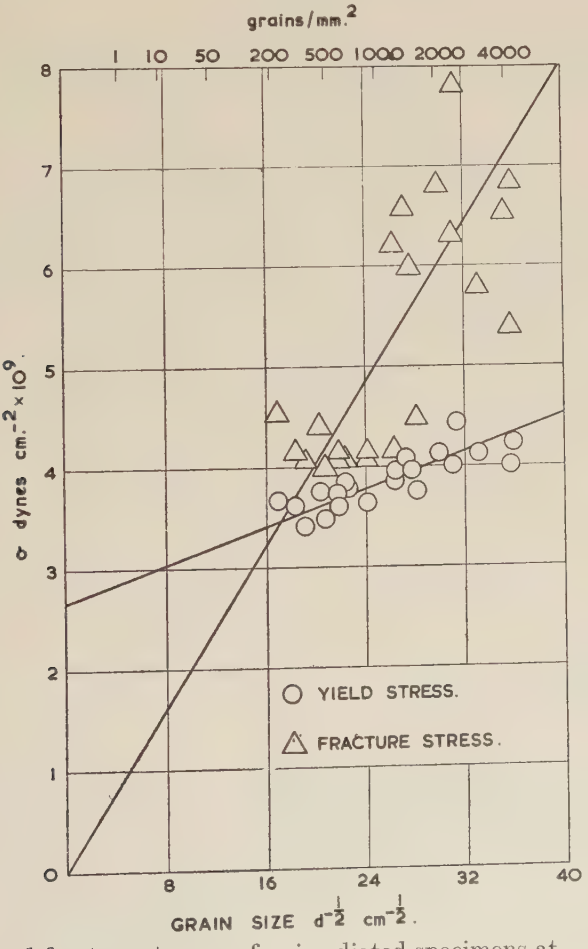

Yield and fracture stresses of unirradiated specimens at −196°C.

Fig. 2

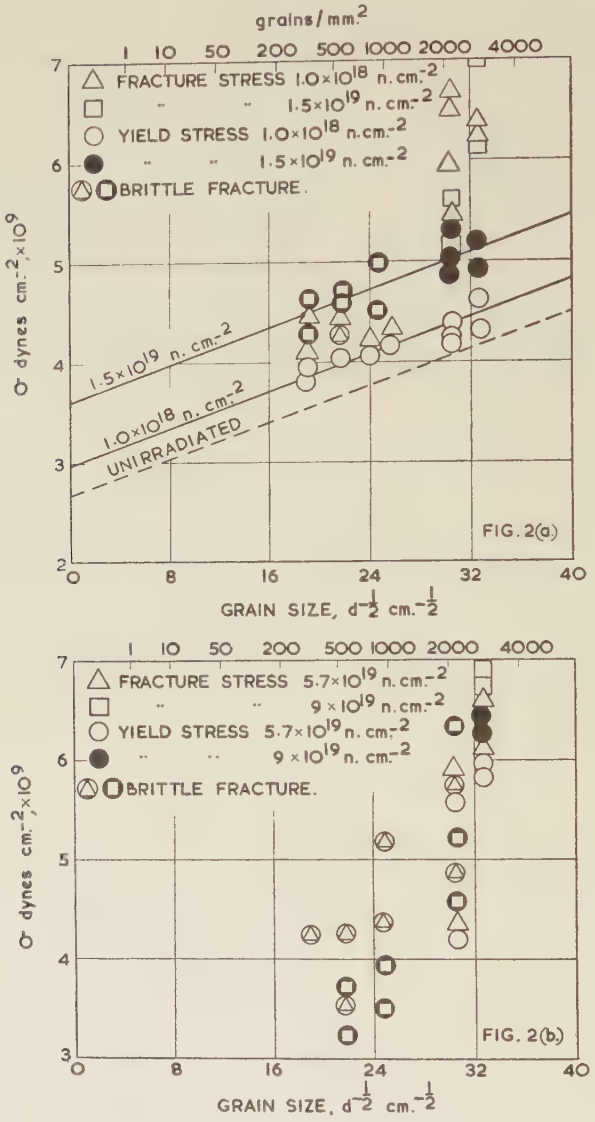

Yield and fracture stresses of irradiated specimens at −196°C.
(*a*) For doses 1×10^{18} and $1{\cdot}5 \times 10^{19}$ neutron cm^{-2}.
(*b*) For doses $5{\cdot}7 \times 10^{19}$ and $9{\cdot}0 \times 10^{19}$ neutron cm^{-2}.

After irradiation it was found that k_y is unchanged, in agreement with Churchman *et al.* (1957) who reported that in tests at 20°C k_y remained constant to within 15%. Greater accuracy was not possible because of the scatter in the results which was mainly due to difficulties in measuring the grain size of irradiated specimens. This also applies to the results shown in figs. 1–4 except for the 1×10^{18}, 3×10^{18}, and 8×10^{18} neutron cm^{-2}

dose irradiations tested at −78°c, in which the grain size was controlled more accurately. From the latter results it was concluded that k_y remains constant to within 5% with irradiation.

Fig. 3

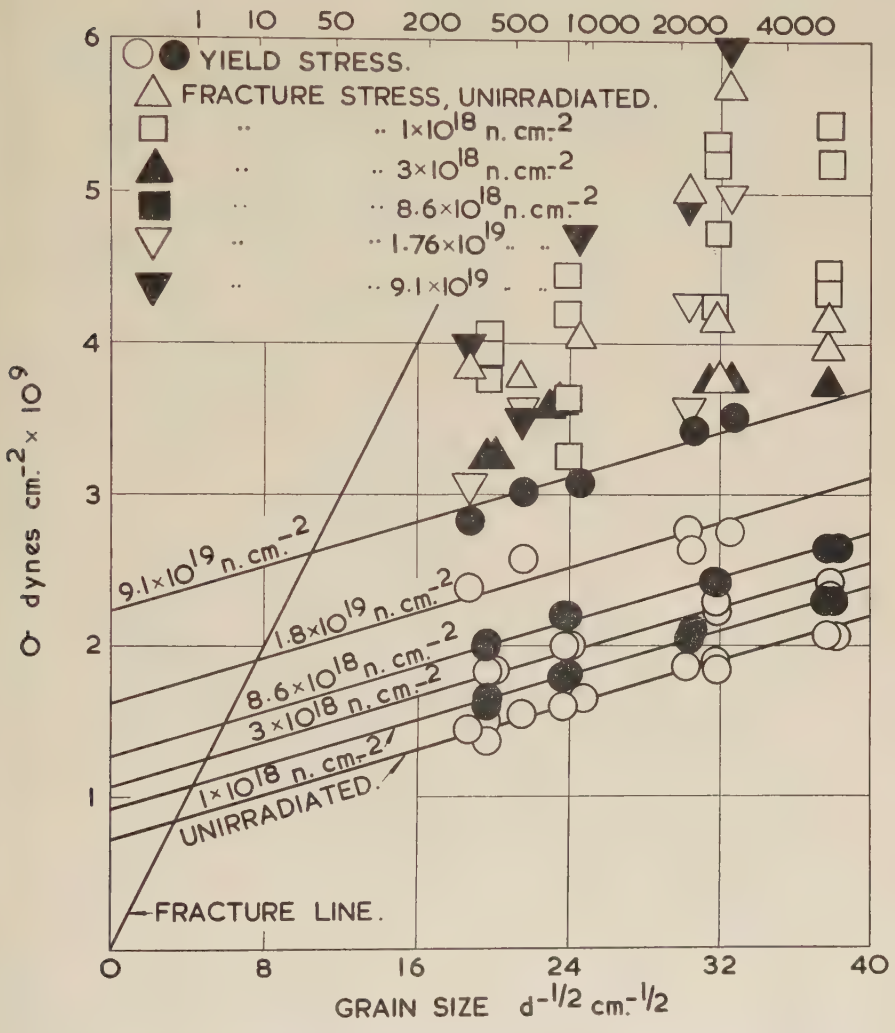

Yield and fracture stresses of unirradiated and irradiated specimens at −78°c.

Irradiation increases σ_i at a rate approximately proportional to the cube root of the dose, as shown in fig. 5†. This agrees with work by Blewitt (1955) on copper. It is interesting to compare fig. 5 with the results of Heslop and Petch (1956) for the variation of σ_i with carbon and

† A somewhat better fit is obtained by taking the increase in σ_i proportional to $\phi^{0.4}$.

nitrogen content. They obtained a linear increase of σ_i which was independent of temperature. The irradiation results show a slight temperature dependence, e.g. $\partial\sigma_i/\partial\phi^{1/3} = 2{\cdot}93$, $3{\cdot}28$ and $3{\cdot}79$ dyne cm^{-2}/10^6 neutron cm^{-2}, at 20°, −78°, and −196°C respectively.

Fig. 4

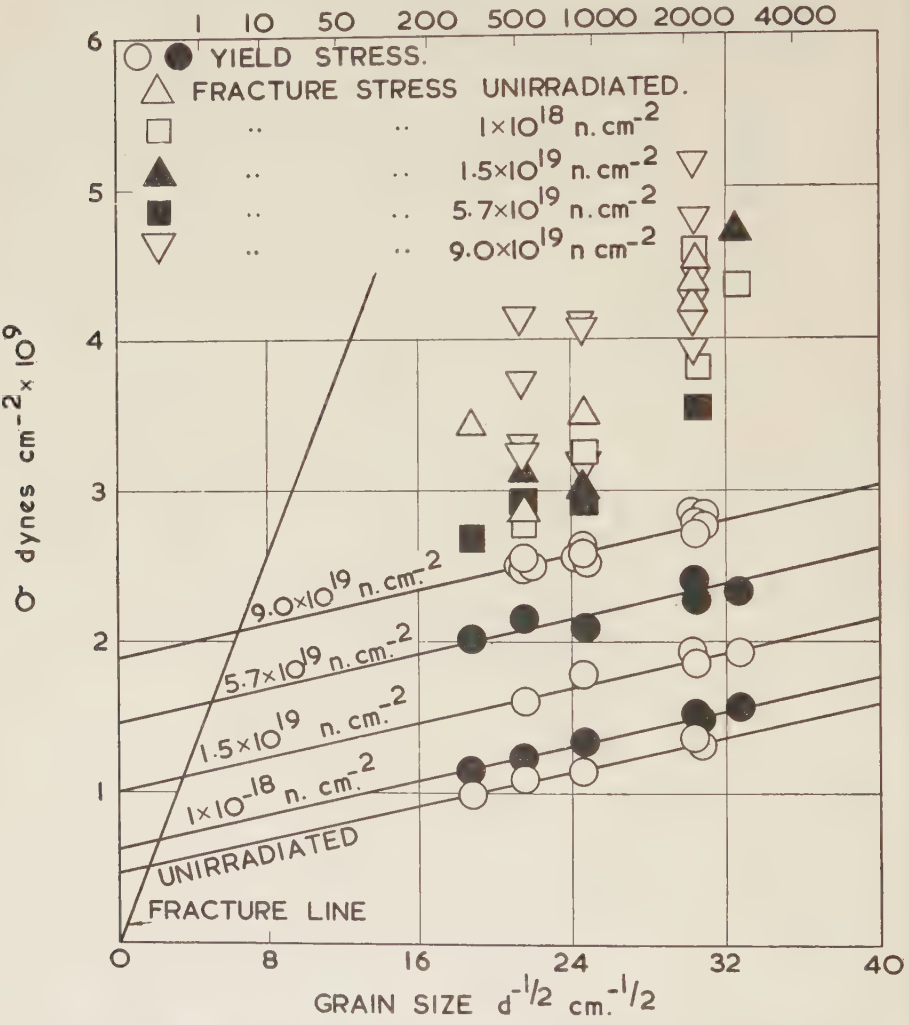

Yield and fracture stresses of unirradiated and irradiated specimens at 20°C.

The fracture stresses at 20° and −78°C are not significantly affected by irradiation. For tests at −196°C irradiation rapidly embrittles specimens of all grain sizes and in many cases fracture occurs without any detectable yield. After high doses some of the specimens fractured at a relatively low stress value.

§ 4. Ductile–Brittle Transition in Unirradiated Specimens

For the range of grain sizes and temperatures used all the unirradiated specimens showed some ductility and only specimens tested at −196°C

Fig. 5

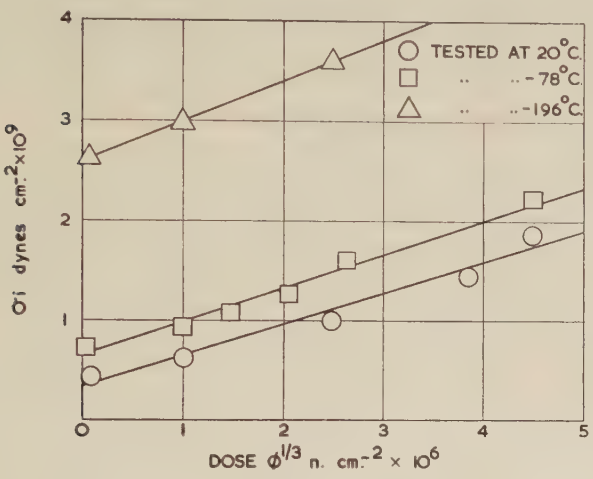

Variation of σ_i, with dose at 20°, −78°, and −196°C.

Fig. 6

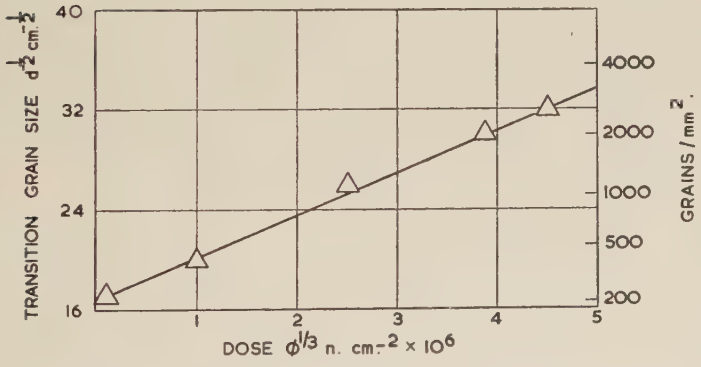

Variation of transition grain size with dose at −196°C.

became brittle after irradiation. For tests at −196°C the reduction in area at fracture varied from 4 to 47% with the range of grain sizes used, but at −78° and 20°C the reduction in area was greater than 60% for all grain sizes. Since the coarse-grained specimens of this steel are ductile at −196°C the transition temperature cannot be determined without using lower temperatures. Low (1953) has given a method of determining the transition grain size which can be used for the present results. The lower yield stress σ_y and fracture stress σ_f are plotted against $d^{-1/2}$. The $\sigma_y/d^{-1/2}$ plot follows the Petch relation (eqn. (3)) and $\sigma_f/d^{-1/2}$ the

Griffith–Orowan relation:

$$\sigma_f = \text{const} \times d^{-1/2} \quad . \quad . \quad . \quad . \quad . \quad . \quad . \quad . \quad (5)$$

which is a straight line passing through the origin. The intersection of $\sigma_y/d^{-1/2}$ and $\sigma_f/d^{-1/2}$ gives the transition grain size. In fig. 1 the method has been used to obtain the transition grain size at $-196°$C,

$$d^{-1/2} = 17{\cdot}3\ \text{cm}^{-1/2},\ \sigma_f/d^{-1/2} = 0{\cdot}2 \times 10^9\ \text{c.g.s. units.}$$

The equation of the fracture stress line according to Cottrell's theory is

$$\sigma_f = \left(\frac{\beta\gamma\mu}{k_y}\right) d^{-1/2}. \quad . \quad . \quad . \quad . \quad . \quad . \quad . \quad (6)$$

Taking $\mu = 8 \times 10^{11}$ dyne cm^{-2}, $k_y = 4{\cdot}6 \times 10^7$ c.g.s. units, and the results from fig. 1 the effective surface energy, $\gamma = 1{\cdot}16 \times 10^4$ ergs cm^{-2}. This value is less than half that obtained from results by Low, $\gamma = 2{\cdot}8 \times 10^4$ ergs cm^{-2}, where $k_y = 9{\cdot}98 \times 10^7$ c.g.s. units and $d^{-1/2} = 11{\cdot}2$ cm^{-2}, for a low carbon rimming steel containing 0·07% carbon, 0·03% manganese, 0·02% phosphorus, 0·033% sulphur, 0·020% oxygen, and 0·005% nitrogen.

For tests at $-78°$ and 20°C the line plotted through the fracture stress results does not extrapolate to the origin. This is due probably to a change in the mode of fracture, from ductile cleavage to ductile fibrous (Crussard *et al.* 1956), in specimens tested well above the transition temperature. In fractures with a reduction in area greater than 50% the fracture line has been observed to deviate from linearity (Cottrell 1958). Thus the transition grain size cannot be determined directly by the method used for tests at $-196°$C. The transition grain size can be estimated, however, using eqn. (6). Assuming $\beta\gamma\mu$ to be independent of temperature in the range used, the slope $\sigma_f/d^{-1/2}$ can be calculated at $-78°$ and 20°C from the measured values of k_y at these temperatures, and the value of $\beta\gamma\mu$ at $-196°$C. At $-78°$C, $\sigma_f/d^{-1/2} = 2{\cdot}51 \times 10^8$ c.g.s. units and at 20°C, $\sigma_f/d^{-1/2} = 3{\cdot}21 \times 10^8$ c.g.s. units. These values have been plotted in figs. 3 and 4 to obtain the transition grain sizes.

§ 5. Effect of Irradiation Dose on Transition Grain Size

It is now possible to determine the effect of irradiation on the transition grain size directly from figs. 1–5. Since k_y is constant with irradiation the fracture line is unaffected and the transition grain size is the intersection of this line and $\sigma_y/d^{-1/2}$ at various doses. In table 2 the information from these plots is summarized.

As mentioned in § 1, Cottrell's equation for the transition predicts that if k_y is constant, then at any one temperature, the product $\sigma_i d^{1/2}$ should be constant. It has been shown that k_y is constant with irradiation to within 5% and σ_i increases, thus $d^{1/2}$ should decrease at a corresponding rate. Only the results obtained at $-196°$C can be used to check this prediction since the transition grain sizes at $-78°$ and 20°C were calculated assuming Cottrell's relation to be true. From fig. 2 it is possible to determine the transition grain size for the high doses fairly accurately, but after 1×10^{18} and $1{\cdot}5 \times 10^{19}$ neutron cm^{-2} the results are rather

Table 2. Values of k_y, σ_i and Transition Grain Size at Three Testing Temperatures for Specimens Irradiated Between 0 and $9{\cdot}1 \times 10^{19}$ neutron cm^{-2}

Temp. of testing °C	Dose, ϕ n. cm^{-2} $\times 10^{18}$	Dose, $\phi^{1/3}$ n. cm^{-2} $\times 10^{6}$	k_y c.g.s. $\times 10^{7}$	σ_i dyne cm^{-2} $\times 10^{9}$	Transition grain size $d^{-1/2}$, $cm^{-1/2}$	$\sigma_i d^{1/2}$ c.g.s. $\times 10^{8}$
−196	0	0	4·64	2·66	17·5	1·52
	1	1	4·64	2·98	20·0	1·44
	15	2·47	4·64	3·61	26·0	1·39
	57	3·85	4·64	4·15	30·0	1·38
	90	4·48	4·64	4·40	32·0	1·38
−78	0	0	3·70	0·72	3·5	—
	1	1	3·70	0·92	4·4	—
	3	1·44	3·70	1·07	5·1	—
	8·6	2·05	3·70	1·27	6·0	—
	18	2·62	3·70	1·62	7·7	—
	91	4·50	3·70	2·22	10·5	—
20	0	0	2·89	0·45	1·6	—
	1	1	2·89	0·62	2·2	—
	15	2·47	2·89	1·0	3·5	—
	57	3·85	2·89	1·45	5·0	—
	90	4·48	2·89	1·87	6·5	—

Fig. 7

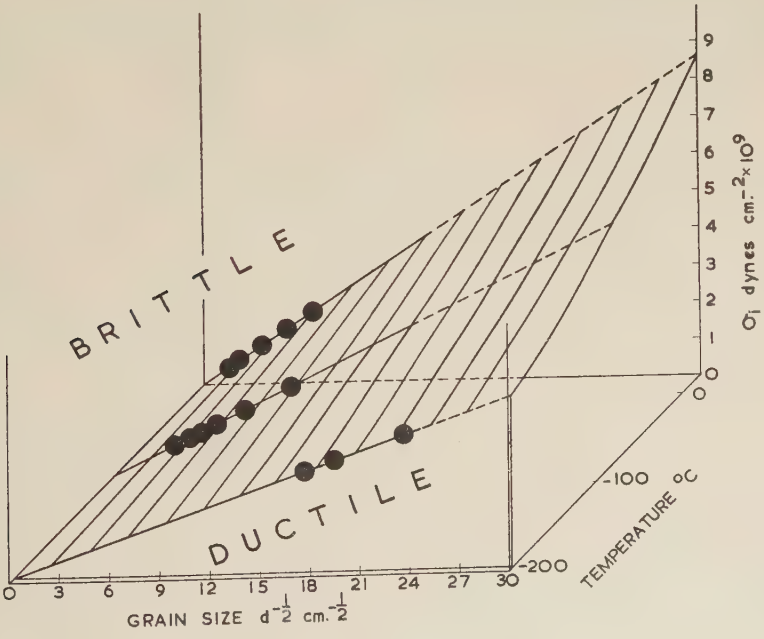

Transition surface relating yield stress, grain size and temperature.

scattered and the transition grain size values obtained are only approximate. The σ_i results are shown in fig. 5, for doses up to $1{\cdot}5 \times 10^{19}$ neutron cm^{-2}. The high dose values have been obtained by extrapolation. The product $\sigma_i d^{1/2}$ which is given in the last column of table 2, remains reasonably constant as σ_i increases. At $-196°C$ there is a linear variation of transition grain size with the cube root of the dose (fig. 6).

In conclusion, the combined effect of grain size, σ_i, and temperature on the transition can be obtained from the above results and the transition surface separating brittle and ductile fracture is plotted in fig. 7.

Acknowledgments

The authors wish to thank Dr. A. H. Cottrell for constant advice and encouragement. The work reported here is an extension of experiments started by Dr. A. T. Churchman, and we are indebted to him. Thanks are due also to Mr. D. C. Wynne for help with some of the experiments and to many colleagues for valuable discussions.

References

Blewitt, T. H., quoted by Kinchin, G. H., and Pease, R. S., 1955, *Prog. Phys.*, **18,** 1.

Churchman, A. T., Mogford, I. L., and Cottrell, A. H., 1957, *Phil. Mag.*, **2,** 1271.

Cottrell, A. H., 1958, *Trans. Met. Soc. A.I.M.E.*, **212,** 192.

Cracknell, A., and Petch, N. J., 1955, *Acta Met.*, **3,** 186.

Crussard, C., Borione, R., Plateau, J., Morrillon, Y., and Maratray, F., 1956, *J. Iron St. Inst.*, **183,** 146.

Heslop, J., and Petch, N. J., 1956, *Phil. Mag.*, **1,** 866.

Low, J. R., 1953. *Relation of Properties to Microstructure*, (Amer. Soc. of Metals), p. 163.

Isochronal Annealing of Vacancies in Aluminium†

By C. Panseri and T. Federighi
Istituto Sperimentale Metalli Leggeri—C.P. 169, Novara, Italy

[Received May 29; and in revised form July 7, 1958]

Abstract

A study based on electrical resistivity measurements at liquid nitrogen temperature has been carried out on the isochronal annealing out of quenched-in vacancies in 99·995% Al. The process of annealing takes place in two stages; the first stage is centred at about room temperature and takes place at a lower temperature the higher the quenching temperature; also the observed migration energies (in the range 0·37 to 0·58 ev) and the mean number of jumps for annihilation (in the range 10^4 to 10^9) are very sensitive to the initial concentration of defects, that is to the quenching temperature. The second stage takes place at about 160°c and its amount increases largely with quenching temperature; its activation energy results in $1·3 \pm 0·2$ ev. The results have been interpreted as due principally to a clustering of vacancies (first stage) and subsequent dispersion of clusters by self-diffusion (second stage).

§ 1. Introduction

It is now a well-established fact that in many close-packed metals it is possible, by rapid quenching from high temperature, to freeze-in lattice defects which are in thermal equilibrium at the high temperature. Theoretical considerations on the energy of formation support the hypothesis that such defects should be vacancies (single or possibly pairs) rather than interstitial atoms. Cottrell (1957) has given a short review of some recent results for various metals.

After the vacancies are quenched-in the question arises about the way they are annealed out to reach the equilibrium concentration. The present investigation was undertaken to throw some light on the annealing process in aluminium; the concentration of defects has been evaluated by means of the increase of resistivity they produce. In this paper results obtained specially by isochronal annealing are described; results connected with isothermal annealing will be reported in a forthcoming paper.

The possibility of freezing-in thermally generated defects in aluminium was shown by Maddin and Cottrell (1955) by the increase of yield stress of aluminium single crystals by quenching and by ageing after quenching; Levy and Metzger (1955) confirmed it by the decrease of the internal

† Communicated by the Authors. A short preliminary report on this work was presented in Italian by T. Federighi and F. Gatto, at the Meeting of the Società Italiana di Fisica, at Padua, September 22, 1957.

friction of aluminium by ageing after quenching. In each case the observed effects were referred to a pinning of dislocations by vacancies. The assumption that the quenched-in defects were vacancy-like defects was then supported by the observation of Takamura (1956) who reported that during the annealing process a contraction of the sample was observed. Subsequently, the possibility of freezing-in vacancies in aluminium was shown by an increase of electrical resistivity by quenching (Wintenberger 1956 and Panseri *et al.* 1957). The former showed that the rate of annealing of vacancies was largely increased by 10% plastic deformation; the latter reported that probably some clustering of vacancies takes place in the isothermal annealing at room temperature as the process was quicker the higher the quenching temperature.

Since the present investigation was started, other results obtained by electrical resistivity measurements have been published. Bradshaw and Pearson (1957) reported values of 0·76 ev for the formation energy of the quenched-in defects and 0·44 ev for their migration energy; De Sorbo and Turnbull (1957) reported a value of 0·37 ev for the migration energy and quoted a value higher than 0·6 ev for the formation energy. Finally Wintenberger (1957 a) reported a value of about $0{\cdot}57 \pm 0{\cdot}01$ for the migration energy after air quenching. Till now however, as far as we know, the details of the annealing process after quenching had not been investigated.

§ 2. Experimental Procedure

Aluminium of nominal purity 99·995% was used. Principal impurities were Cu = 0·0003%, Fe = 0·0004%, Si = 0·0015%.

Owing to the very small resistivity variations these were always computed from resistance variations of wire samples of ϕ 1 mm and length 50 cm with four soldered contacts. To simplify operations, samples were wound as a lamp coil filament and supported by an insulating rod. After soldering, samples were always stabilized by annealing some hours at 630°C. Usually resistance measurements were carried out in liquid nitrogen using a dummy sample to account for the variations of temperature; only some additional measurements, as specified hereafter, were carried out at 20°C in a thermostatic oil bath. The usual potentiometric system, using a Wenner type potentiometer, was employed in each case. The sensitivity of the equipment was about 1×10^{-5}.

The resistivity variations have been computed by the formula $\Delta\rho = \rho\Delta R/R$ where ΔR and R are respectively the variation of resistance and the resistance of the fully annealed specimen, and ρ the resistivity of aluminium ($\rho = 0{\cdot}228$ μohm cm at -195°C and $\rho = 2{\cdot}65$ μohm cm at 20°C). Results have been expressed usually in mμohm cm $= 10^{-9}$ ohm cm, a unit which is very useful for quenching experiments.

Quenching operations were carried out by manual extraction of samples from the furnace and by rapid immersion in the cooling medium (brine at about 2°C); immediately after that, samples were dipped in liquid nitrogen. This procedure, which is not, of course, the most convenient

for accurate reproducibility of quenching operations, was selected in this research for its great simplicity. By this technique, wires thinner than 1 mm could not be used as they would cool too much during the extraction from the furnace, before the water quenching.

The annealing treatments, after quenching, were carried out at various temperatures in the range -100 to 240°C by using proper liquid baths.

§ 3. Results

3.1. *Formation Energy*

Although it was not the principal object of this work, it was necessary at the beginning to determine the increase of resistivity which was possible to obtain by the adopted technique, with the quenching temperature.

Preliminary experiments had shown that by annealing a quenched sample for a few minutes at 240°C the same value of electrical resistance that existed before quenching was within experimental error obtained (see, however § 3.5); namely, all the excess of resistivity was practically annealed out at a such temperature. Therefore the quenched-in component of resistivity was usually computed from the changes of resistance, at liquid nitrogen temperature, after quenching and after the subsequent annealing at 240°C.

Results of many observations are shown in fig. 1, plotted as usual, on a semilogarithmic scale against $1/T$; in the same figure the results of Bradshaw and Pearson are indicated.

The following points may be noted: (1) notwithstanding the relatively large wire diameter, the quenched-in component of resistivity $\Delta\rho_0$ increases with quenching temperature in the range 360 to 620°C; (2) at low temperatures, until about 420°C, a straight line can be drawn which gives $E_f = 0{\cdot}76 \pm 0{\cdot}03$ ev for the formation energy in agreement with Bradshaw and Pearson's results; (3) at higher temperatures a deviation below the straight line is observed; (4) the whole results are lower by a factor 0·65 than the Bradshaw and Pearson ones; the straight line of the present results can be described by the relation:

$$\Delta\rho_0 = 800 \exp(-0{\cdot}76/kT)\ \mu\text{ohm cm} \quad . \quad . \quad . \quad . \quad (1)$$

and the pre-exponential factor is to confront with the value 1240 μohm cm reported by Bradshaw and Pearson.

It is interesting to observe that although a fraction of defects is lost by using a large diameter wire as in the present case, the fraction of quenched-in vacancies is still sufficient to leave a role to vacancies in increasing the rate of diffusion in pre-precipitation in aluminium alloys (Federighi 1958).

3.2. *Isochronal Annealing*

In order to know in which range of temperature the defects were annealed out, a first set of isochronal annealing was carried out after quenching from several temperatures; the selected procedure for these

Fig. 1

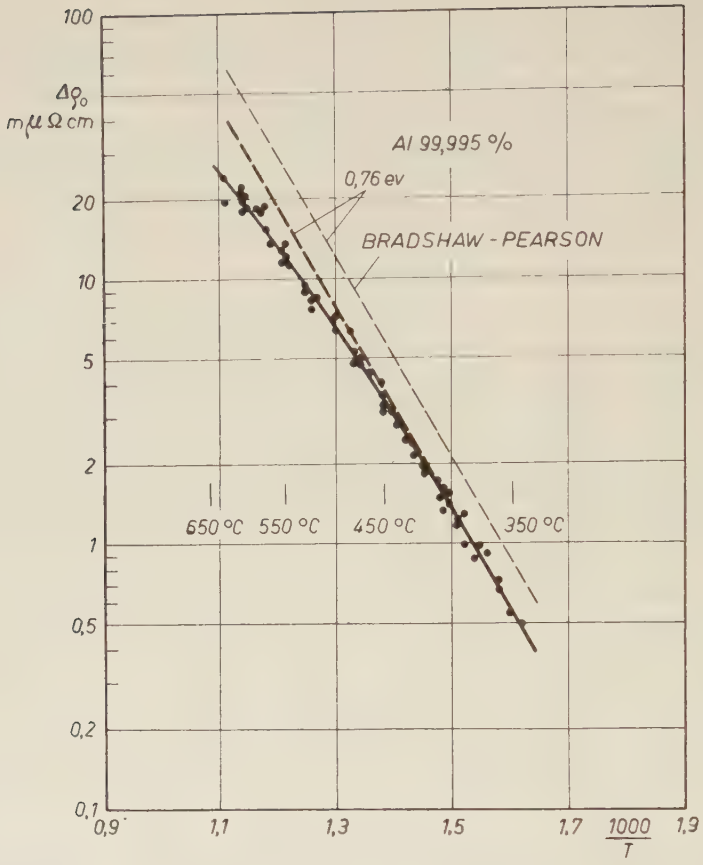

Semilogarithmic plot of quenched-in resistivity with the reciprocal of the absolute quenching temperature.

Fig. 2

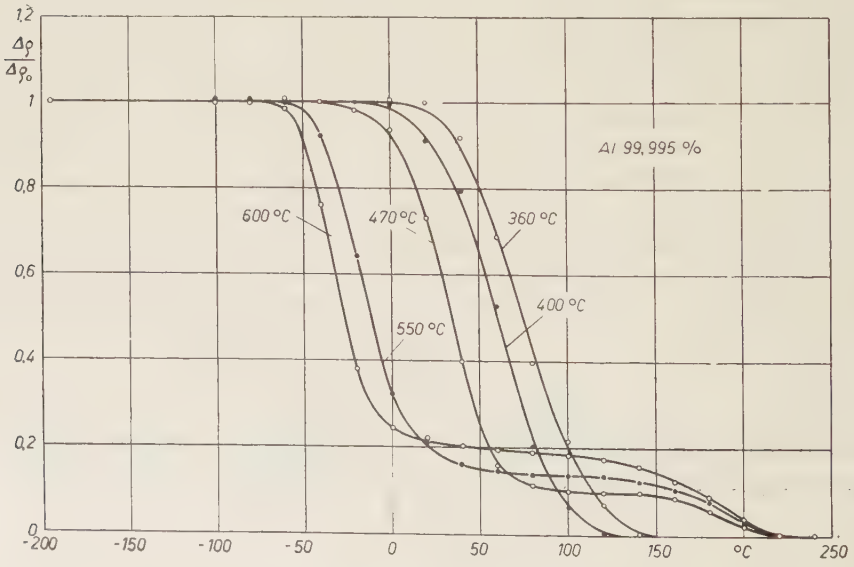

Isochronal annealing of 2 minutes at each temperature, after quenching from various temperatures.

tests was an annealing of 2 minutes at increasing temperature with steps of 20°C, in the range between −100°C to 240°C; hence after each treatment the variation of the electrical resistance in liquid nitrogen was determined.

This first set of results is shown in fig. 2; they have been normalized, namely $\Delta\rho/\Delta\rho_0$ is given instead of $\Delta\rho$. $\Delta\rho$ is the residual increment of resistivity after the treatment at each temperature and $\Delta\rho_0$ is the experimentally observed increase of resistivity (see table 1), which of course for higher quenching temperature is lower than the value $\Delta\rho_0$ obtained from eqn. (1).

Table 1. Data for Curves of Figs. 2 and 3 ($\Delta\rho_0$ and $\Delta\rho_0''$ are Mean Values, except for 360°C)

Quenching temperature °C	$\Delta\rho_0$ mμohm cm	$\Delta\rho_0''$ mμohm cm	$\frac{\Delta\rho_0''}{\Delta\rho_0}$	E_m ev	Jumps n
600	19·5	3·5	0·18	$0{\cdot}58 \pm 0{\cdot}03$	1×10^4
550	11	1·55	0·14	$0{\cdot}42 \pm 0{\cdot}02$	$6{\cdot}6 \times 10^7$
470	4·7	0·5	0·1	$0{\cdot}37 \pm 0{\cdot}07$	$6{\cdot}5 \times 10^9$
400	1·6	$\simeq 0$	$\simeq 0$	$0{\cdot}45 \pm 0{\cdot}03$	$1{\cdot}4 \times 10^9$
360	0·7	0	0	—	—

The first general observation is the existence of a very strong influence of quenching temperature.

In particular the following facts can be deduced: (1) for high (600°C) and mean values (470°C–550°C) of the quenching temperature, the annealing of defects takes place in two stages; in consequence of these results the quenched-in resistivity $\Delta\rho_0$ can be subdivided into two parts:

$$\Delta\rho_0 = \Delta\rho_0' + \Delta\rho_0''$$

where $\Delta\rho_0'$ and $\Delta\rho_0''$ represent respectively the first and the second stage; (2) for low quenching temperatures (400°C, 360°C) the recovery takes place in one stage; that is $\Delta\rho_0'' \simeq 0$; (3) the fraction of recovery which takes place in the second stage increases with $\Delta\rho_0$, namely with quenching temperature (see § 4.3.1); (4) the first stage which is centred at about room temperature takes place at lower temperatures the higher the quenching temperatures; for instance, after quenching from 600°C a fraction $\Delta\rho/\Delta\rho_0 = 0{\cdot}6$ is observed at about −30°C; after quenching from 400°C the same fraction of recovery is observed at about 55°C; (5) the range of temperature of the second stage (if existing) does not seem to be practically dependent on the quenching temperature, and it is centred at about 160°C.

The presence of a second stage in the annealing out of quenched-in defects in aluminium had been noted earlier by Panseri *et al.* (1958) in

a study of Al Mg alloys. Also Wintenberger (1957 b) reported that after a rapid quenching, only a fraction of quenched-in resistivity was annealed out at room temperature.

Following these results other similar isochronal annealings, after quenching from four temperatures, were carried out, with the same procedure, to test reproducibility and the influence of time of annealing (2 or 15 min). Results are reported in fig. 3 (results of fig. 2 also are included). In table 1, the mean values of $\Delta\rho_0$ and $\Delta\rho_0''$ and their ratio for curves of figs. 2 and 3 are reported (for other data of table 1, see below).

Fig. 3

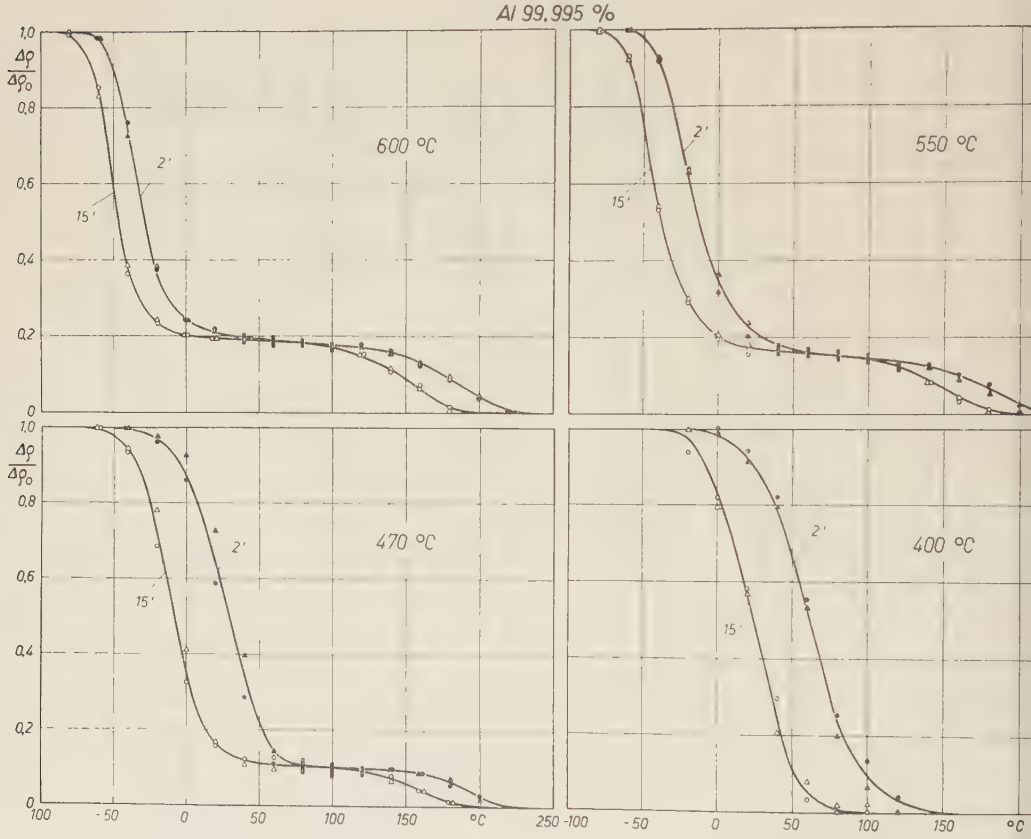

Isochronal annealing of 2 or 15 minutes at each temperature, after quenching from various temperatures.

Since at the beginning of the anneal from $-100°C$ the resistivity remained constant until a sufficiently higher temperature, experimental points in fig. 3 (and fig. 2) are reported only from that temperature at which the variation began to be observed. It is necessary to note however that after quenching from 400°C (and 360°C) an abnormal scattering of

results, sometimes with a small increase of resistivity, was noted before the true variation shown in figs. 2 and 3. At present it is not sure if this increase is real, and if it is, the reason is not clear.

The reproducibility of curves of fig. 3 appears to be good enough for the high temperature quenching and not so good for the lower temperatures; it should be noted however that in figs. 2 and 3 the scattering of experimental points is higher, the lower the quenching temperature, due to the large decrease of $\Delta\rho_0$ (see table 1).

For the interpretation of the results it is useful to introduce the number of jumps n for annihilation of defects in the first stage, given by (Cottrell 1957):

$$n \simeq 12 \, . \, t \, . \, 10^{13} \exp\left(-E_m/kT\right). \quad . \quad . \quad . \quad . \quad . \quad (2)$$

where E_m is the migration energy and t the lifetime of the defects (the entropic factor has been put equal to unity). From the data of fig. 3 it is possible to deduce the values of n and of E_m They are evaluated for a fraction of recovery $\Delta\rho/\Delta\rho_0 = 0{\cdot}6$, and included in table 1. The values of E_m are practically constant for any selected fraction $\Delta\rho/\Delta\rho_0$ in the first stage of recovery for each couple of curves drawn in fig. 3; the errors reported in table 1 have been computed from the scattering of experimental points.

A noticeable dependence of E_m and n upon quenching temperature appears to exist; this dependence, notwithstanding the indetermination of the results, can be concluded to be real and will be discussed in § 4.

It is interesting to note that the rapid annealing observed after quenching from 600°C is related to the low value of n and not to a low migration energy (which, on the contrary, is the highest observed).

3.3. *Some Isothermal Results*

The effect of quenching temperature observed in isochronal annealing should be evident also in isothermal annealing curves as reported by Panseri *et al.* (1957) by means of electrical resistivity measurements at room temperature. To show this effect better, a set of isothermal annealing curves at 0°C was therefore obtained, by means of more convenient liquid nitrogen measurements.

The quenching temperatures were selected in the range 460 to 600°C. After a time of isothermal recovery sufficiently long to get a large fraction of recovery, samples were left to rest 16 hours at room temperature (20°C) to deduce the final value of the first stage; then the samples were annealed $\frac{1}{2}$ hour at 240°C to anneal out the second stage.

Results, again in normalized form, are reported in fig. 4; the effect of quenching temperature and the presence of the second stage (shown by the limit value of each curve) are evident.

3.4. *The Second Stage*

3.4.1. *Isochronal annealing*

Some characteristics of the second stage will now be reported in this and in the following sub-sections.

In fig. 5 (left) isochronal annealing curves of the second stage are shown ; they have been deduced from the data of fig. 3, after quenching from 600°c; the results are normalized, namely $\Delta\rho''/\Delta\rho_0''$ has been plotted, where $\Delta\rho''$ is the residual increase of resistivity after each treatment, and $\Delta\rho_0''$ has been evaluated at 80°c (table 1). Similar isochronal

Fig. 4

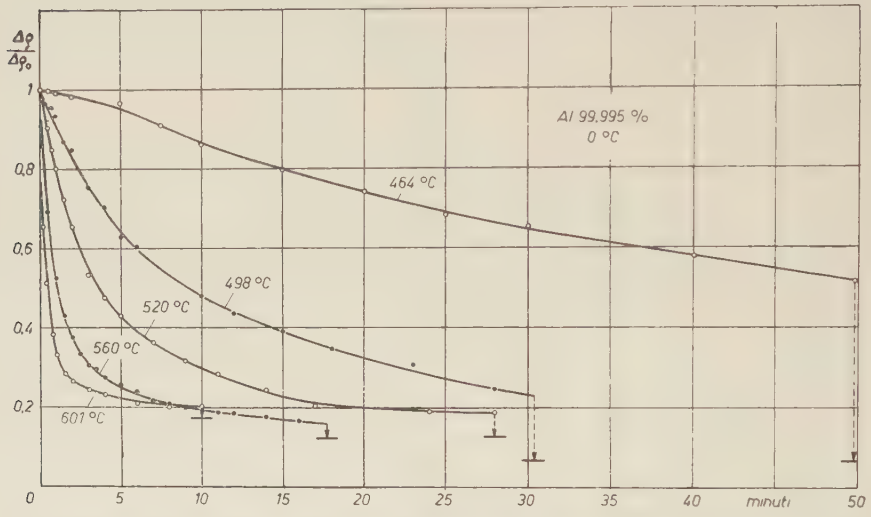

Isothermal annealing at 0°c after quenching from various temperatures.

Fig. 5

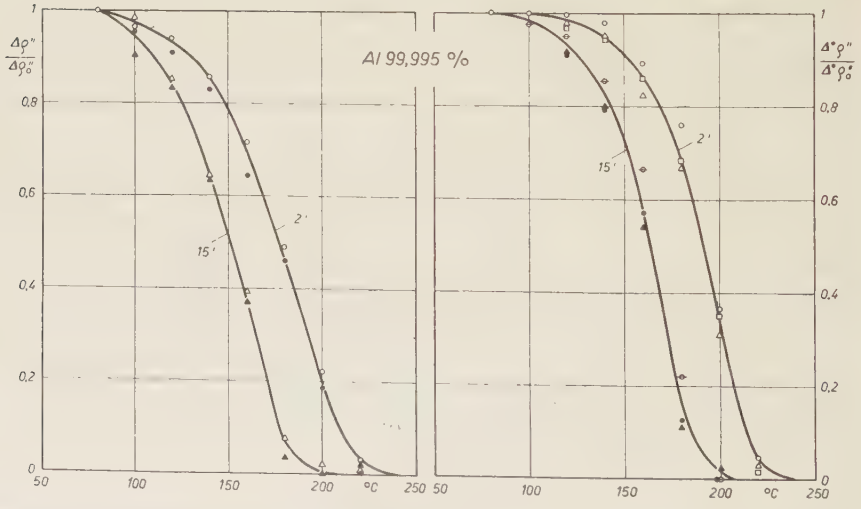

Isochronal annealing of 2 or 15 minutes at each temperature, for the second stage, after quenching from 600°c. Left: data taken from fig. 3; right: other results (see the text).

annealing curves of the second stage, again after quenching from 600°c, are reported in fig. 5 (right); in these measurements the first stage has taken place in 16 hours at 20°c followed by 3 minutes at 80°c.

The examination of results shows that the way in which the first stage takes place has a slight influence on the range of temperature of the second stage; namely, the second stage is not independent of the first. For example, a fraction $\Delta\rho''/\Delta\rho_0'' = 0{\cdot}6$ in 2 minutes is observed at 170°c in fig. 5 (left) and at 185°c (right).

From the shifting of the isochronal annealing curves with the time of annealing, an activation energy Q can be evaluated assuming that the time to observe a fraction of recovery is proportional to $\exp(Q/kT)$. The result is $Q = 1{\cdot}3 \pm 0{\cdot}2$ ev, independently, for the data reported in fig. 5, left or right.

3.4.2. *Dependence of* $\Delta\rho''$ *upon* $\Delta\rho_0$

The results obtained in many tests about the dependence of $\Delta\rho_0''$ on $\Delta\rho_0$ are shown in fig. 6 on logarithmic scales. Experimental points have

Fig. 6

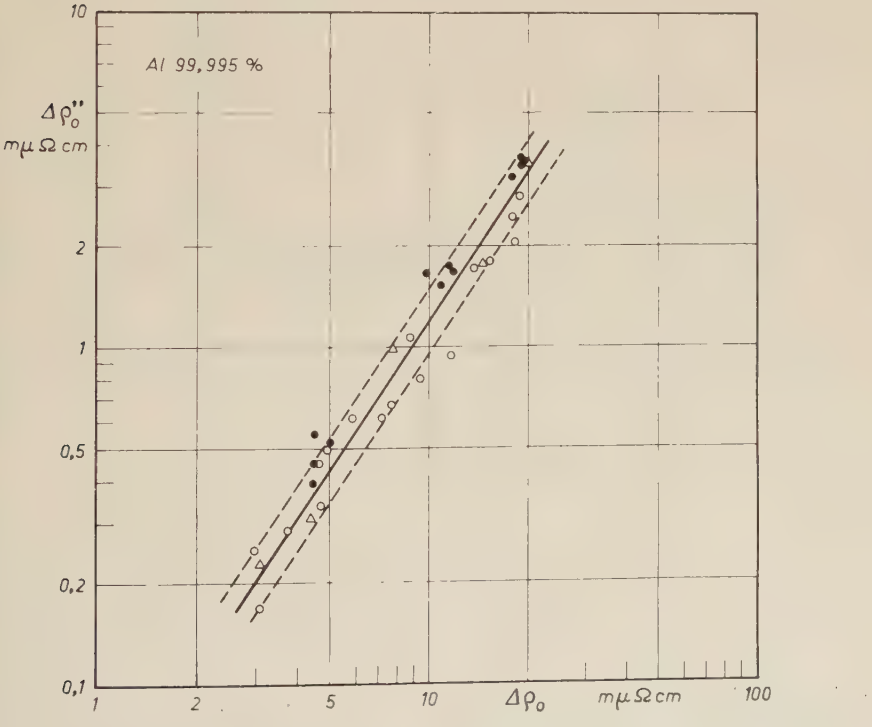

Logarithmic plot of $\Delta\rho_0''$ with $\Delta\rho_0$ (for explanation of experimental points see the text).

been subdivided into three classes; black circle points have been deduced from the data of fig. 3 (or table 1), white triangle points have been deduced from the isothermal curves of fig. 4, while white circle points have been deduced from proper experiments in which the first stage has taken place in 3 minutes at 80°C. The examination of results shows that despite a noticeable dispersion of experimental points the second stage $\Delta\rho_0''$ is related to the total increase of quenched-in resistivity $\Delta\rho_0$ by the law $\Delta\rho_0'' = a \cdot \Delta\rho_0^m$ where m has a value of about $\frac{3}{2}$ and $a = 3{\cdot}8 \times 10^{-2}$. Also the second stage is somewhat higher if the first stage has taken place at low temperatures; again there seems to exist a slight dependence of the second stage from the way the first stage has taken place.

The ratio $\Delta\rho_0''/\Delta\rho_0$ is obviously given by $3{\cdot}8 \times 10^{-2}\sqrt{\Delta\rho_0}$ and increases with $\Delta\rho_0$.

3.4.3. *Dependence of* $\Delta\rho_0''$ *upon* $1/T$

The data of $\Delta\rho_0''$ of fig. 6 can be plotted against $1/T$ to deduce a fictitious formation energy for the defects of the second stage, as shown

Fig. 7

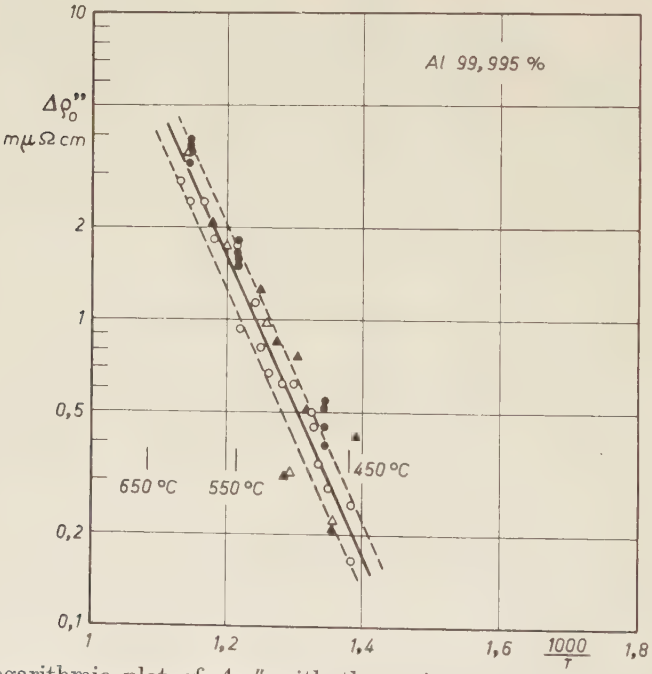

Semilogarithmic plot of $\Delta\rho_0''$ with the reciprocal of the absolute quenching temperature (for explanation of experimental points see the text).

in fig. 7. Some additional experimental points (black triangle points) for the second stage, evaluated by measurements at 20°C, have been added. For this set of tests the first stage took place in 16 hours at 20°C.

The fictitious formation energy so deduced is about $1{\cdot}2 \pm 0{\cdot}1$ ev; about the same value could obviously be evaluated from the reported dependence of $\Delta\rho_0''$ *vs* $\Delta\rho_0$ and from the dependence of $\Delta\rho_0$ upon T.

It is to be pointed out that the dependence of $\Delta\rho_0''$ on quenching temperature is relatively strong.

3.4.4. *Effect of quenching speed*

The values of the second stage $\Delta\rho_0''$, and of the total increase of resistivity $\Delta\rho_0$, are very sensitive to quenching speed, as shown in table 2. In these experiments the second stage has been evaluated after annealing for 3 minutes at 80°c. The time to reach a temperature lower than 80°c was less than 1 minute with air quenching and less than $\frac{1}{2}$ minute for a stream of air; after this time samples were dipped in liquid nitrogen.

Table 2. Influence of Cooling Medium on $\Delta\rho_0$ and $\Delta\rho_0''$
(Results are Mean Values of Several Observations)

Cooling medium	$\Delta\rho_0$ mμohm cm	$\Delta\rho_0''$ mμohm cm
Brine at 2°c	19·5	3·5
Water at 30°c	15	1·8
Oil	3·7	1·6
Blow of air	0·5	0·15
Still air	0·5	0·1

3.4.5. *Dependence of the second stage on the temperature of measurement*

As the second stage can be evaluated on a sample by measurements in liquid nitrogen, or at 20°c, control is possible if it is independent of temperature.

A series of 6 tests has given the following result: $\Delta^*\rho_0''/\Delta\rho_0'' = 1{\cdot}17 \pm 0{\cdot}03$ where the star indicates the measurements at 20°c. A slight dependence from the temperature of measurement seems to be present.

3.5. *Plastic Deformation during Quenching*

It is possible to obtain a rough estimate of the amount of plastic deformation during quenching by electrical resistance measurements. For this purpose it is necessary to evaluate the variation of resistance of the sample between the fully annealed state before and after the quenching (when all the introduced defects are annealed out).

The resistance R of the sample can be expressed by $R = \rho \,.\, f$ where ρ is resistivity and f a form factor (dimensionally f is a length $^{-1}$); during small plastic deformation f is altered to $f + \Delta f$, so that it should be possible to detect a permanent increase of resistance ΔR_p given by $\Delta R_p = \rho \,.\, \Delta f$. The plastic deformation ϵ should then be of the same order as $\Delta f/f = \Delta R_p/R$.

As stated before, by carrying out measurements at liquid nitrogen temperature all quenched-in resistivity appears to be annealed out, between experimental errors, after the annealing at 240°C; therefore $\Delta f/f$, if not zero, is very small. However, by carrying out measurements at 20°C (before quenching and after a full annealing after quenching) a permanent increase of R can be detected more easily, due to the fact that ΔR_p increases with ρ, that is, with the temperature of measurement.

Experience has shown that $\Delta R_p/R$ is scattered in the range $1\text{–}5 \times 10^{-4}$ and that there is not an appreciable dependence upon quenching temperature in the range between 400 to 600°C. This very small plastic deformation cannot account, of course, for the increase of resistivity by quenching or justify the dependence of the annealing process upon quenching temperature.

§ 4. Discussion

4.1. *The First Stage*

4.1.1. *High temperature quenching*

The presence of a double step in annealing and the variation of the migration energy with quenching temperature show clearly that more than one kind of defect should be present. Probably several tentative interpretations can be advanced; here we limit ourselves to show that it is possible to give a simple picture of the annealing process in terms of clustering of vacancies. At present this picture is only of a qualitative nature; really it is not easy to give an exact quantitative picture of the annealing process of quenched-in defects (for instance, see Koehler *et al.* 1957 b) as too many factors are involved, especially if there is a tendency to clustering; for instance, one should know the migration energies for each kind of defect (vacancies, divacancies, trivacancies, and more complex aggregates), their binding energies and their contribution to resistivity.

The present picture is based principally on three independent hypotheses: (i) the quenched-in defects are vacancies; (ii) an appreciable binding energy between vacancies exists; (iii) the contribution to resistivity of a cluster of vacancies is smaller than the contribution of the same dispersed single vacancies.

Then the annealing process, in the case of the high temperature quenching (600°C), can be synthetized as follows.

As soon as the annealing temperature increases enough to allow sufficient mobility of point defects, the concentration of which should be of the order of 10^{-4}, vacancies begin to couple together, forming divacancies, with a number of jumps of the order of 10^4, which is much smaller than the number of jumps to reach dislocations ($\simeq 10^9$); if the binding energy of a divacancy is sufficiently high it can live long enough to meet another vacancy before dissociation, and form a trivacancy more stable than a divacancy; the creation of trivacancies will be slowed up when their

concentration has increased to reach about the residual concentration of vacancies: from this moment trivacancies begin to be reached directly by other vacancies and grow up to larger clusters; therefore if the concentration of trivacancies is large enough, only a few vacancies will find a way to dislocation. In conclusion, if the initial concentration of defects is relatively high and the interaction energy between vacancies sufficiently strong, one should expect at first, in isochronal annealing, principally a *coagulation* of vacancies in clusters of some unspecified shape and not a true annihilation of vacancies at dislocations or other sinks; these clusters should be then annealed out subsequently at higher temperature by normal self-diffusion.

This picture is in agreement with the observed results as long as we suppose that the first stage, observed in the range from -80 to -20°C, is caused to a large extent by a smaller effect of clusters on resistivity and not to a true decrease of the concentration of vacancies. There is really an expectation for a smaller effect of clusters on resistivity (Dexter 1956). The second stage should then be due to the dispersion of clusters.

The experimental migration energy (0·58 ev) observed in the first stage should probably be connected with the motion of single vacancies, in agreement with Wintenberger's (1957 a) result; really, if divacancies move much quicker than vacancies (Bartlett and Dienes 1953) they can reach another vacancy, to form a trivacancy, as soon as they form, and therefore the rate of clustering should be controlled by the migration of single vacancies.

The suggested interpretation can account easily for the presence of the two stages, for the low value of jumps n ($\simeq 10^4$) observed in the first stage, and the value of Q of the second stage ($1{\cdot}3 \pm 0{\cdot}2$ ev) which is of the order of magnitude expected for self-diffusion ($1{\cdot}4 \pm 0{\cdot}1$ ev) in aluminium (Nowick 1951).

It is also interesting to note that $E_m + E_f = 0{\cdot}58\,\text{ev} + 0{\cdot}76\,\text{ev} = 1{\cdot}34\,\text{ev}$ is again of the expected order of magnitude for the activation energy for self-diffusion in aluminium. This fact may be considered as good evidence that in aluminium diffusion takes place *via* vacancies, or *vice-versa* that the quenched-in defects are vacancies.

4.1.2. *Lower quenching temperatures*

A very important point to be considered is what happens when the initial concentration of vacancies is lowered, as by quenching from 550°C and 470°C.

There is no doubt that the isochronal annealing curves must change. Actually at a given temperature the time for clustering is higher the lower the initial concentration of vacancies; therefore to observe a given fraction of recovery, in a fixed time, it is necessary to increase the annealing temperature; but at higher temperature the divacancies and the smallest clusters are not so stable and dissociation processes begin to be

competitive. The result is that the process of coagulation is relatively slowed down and many vacancies succeed in reaching dislocations giving a straight contribution to the decrease of resistivity; one should observe therefore an increase in the mean number of jumps n, a decrease of the fraction of the clustered vacancies and a decrease of the mean migration energy due to the presence of a relatively higher fraction of divacancies (whose number of jumps to reach another vacancy is now higher). These facts are really observed.

If the concentration of defects is again lowered, as by quenching from 400°C, the same picture as above takes place, but the temperature at which one could observe (in a fixed time) the coagulation is now sufficiently high so that, due to the more rapid dissociation, no cluster can form, and also the concentration of divacancies is relatively smaller; therefore one should observe the presence of no cluster, an increase in the mean migration energy (as the relative concentration of single-vacancies is now preponderant) and lastly, a high value of n, as now the whole decrease of resistivity should be due to a true annihilation of vacancies at dislocations.

To conclude, this picture is qualitatively in agreement with actual experimental results. The migration energy of divacancies should be, of course, not higher than 0·37 ev, to justify the result obtained by quenching from 470°C; this value is to be compared with the value 0·58 ev assumed for single vacancies.

4.2. *The Second Stage*

As said before, the second stage should be due to the dispersion of clusters of vacancies which have originated during the first stage. This interpretation is in agreement with the presence of the two stages and with the activation energy Q for the second stage considered to be equal to the activation energy for the self-diffusion in aluminium.

Of course, by resistivity measurements only, it is not possible to decide the shape of these clusters, for example, whether they are spherical or whether vacancies prefer to condense to form stacking faults (see, for instance, Kuhlmann-Wilsdorf 1958).

Coulomb and Friedel (1957) have recently given a theory for the formation of clusters of vacancies along dislocations. Although dislocations are surely preferential places where clusters are formed, the present results seem to show that clustering takes place anywhere in the bulk of the sample; actually with the mechanism of Friedel one should expect always $n \simeq 10^9$ in the first stage and Q lower than the activation energy for self-diffusion of aluminium in the second stage.

However, at present one cannot establish clearly the role of dislocations as nucleation agents for clusters; this point will be probably better understood after a study of the influence on the first stage of small plastic deformation after quenching and also by the influence of plastic deformation during quenching using wires of different diameter. In the

same way it is not possible at present to establish if the clusters are nucleated near some kind of impurity; the use of zone-refined aluminium could probably resolve this.

It will be shown now that other interpretations of the second stage are improbable. For example, it might be due: (i) to a precipitation of impurities set in solution before quenching; (ii) to a fraction of vacancies trapped near some impurity or dislocation; (iii) to the annealing out of dislocations introduced by plastic deformation during quenching operations.

With the first hypothesis a saturation for $\Delta\rho_0''$ should be observed at about 400–500°c, when all impurities are set in solution; besides a scarce dependence of $\Delta\rho_0''$ from quenching speed should result. There is no agreement with experimental results.

With the second hypothesis a lower value for Q of about 0·6–0·9 ev should be expected (namely, the sum of migration energy 0·58 ev and the binding energy with impurity atoms which would not be higher than 0·2–0·3 ev); also a quite different dependence should be expected of $\Delta\rho_0''$ upon T; if the concentration of sinks were high, $\Delta\rho_0''$ should be nearly equal to $\Delta\rho_0$, at least until a sufficiently high quenching temperature is reached; if the concentration of sinks were small, $\Delta\rho_0''$ should be practically constant with quenching temperature.

As for the last hypothesis there is no doubt that during the quenching operation there is a plastic deformation, but this is too insignificant to account for the variation of resistivity of the second stage; for instance applying a formula of Wintenberger (1957 a) a plastic deformation of 5×10^{-4} should give an increase of resistivity of about $1{\cdot}8 \times 10^{-3}$ mμohm cm, which is much smaller than the values of about 2 mμohm cm experimentally observed (see table 1). Besides, the second stage should not depend very strongly upon quenching temperature, as in fact it does. Only the hypothesis of clustering therefore appears to account for the experimental results.

4.3. *Additional Remarks*

4.3.1. *On the annealing after irradiation*

McReynolds *et al.* (1955) have reported that in aluminium irradiated with neutrons at -150°c a recovery of resistivity takes place in the range from -80 to -30 with a migration energy of 0·55 ev. Several facts suggest that this recovery might be due to the clustering of vacancies in the same way as after quenching: (1) the migration energy is about the same; (2) the number of jumps computed from the data of McReynolds *et al.* (fig. 3 of their paper) is $1{\cdot}4 \times 10^3$, which is lower than the value observed after quenching from 600°c; this fact was expected as it is possible to deduce, from the same data, that the excess of resistivity after irradiation was $\simeq 76$ mμohm cm, that is about four times higher than the $\Delta\rho_0$ produced by quenching from 600°c; (3) the isothermal annealing curves are of the second order (as after quenching from 600°c, as will be shown in a forthcoming paper).

However, there are other facts which leave some doubts: (1) McReynolds *et al.* do not report the existence of a second stage (it might be that sufficient attention was not given to this possibility); (2) also the critical shear stress is recovered with resistivity and there is no clear mechanism for this in terms of clustering.

Also Blewitt *et al.* (1957) have reported (fig. 20 of their paper) the existence of a stage in the range from -80 to -20, after irradiation with fast neutrons at 10°K, which they attribute to the annealing out of vacancies.

4.3.2. *On vacancies lost during quenching*

As said before, a fraction of vacancies is lost during quenching from high temperature, that is the $\Delta\rho_0$ experimentally observed is lower than the $\Delta\rho_0$ given by eqn. (1). These lost vacancies could have, of course, some bearing on the subsequent annealing process; for instance they could act as nuclei for the clustering process. Therefore, in view of the impossibility of establishing from the actual data the precise role of these lost vacancies (if there is one), it is necessary to consider the actual results as peculiar of the adopted quenching technique; namely they cannot be, *a priori*, extrapolated to other quenching conditions without an experimental confirmation.

4.3.3. *On the annealing of vacancies in gold*

Koehler *et al.* (1957a) have published recently their results on the recovery of vacancies in gold, after quenching from several temperatures. It is useful to mention here some essential points of similarity or dissimilarity between the results for gold and for aluminium. The principal results of Koehler *et al.* can be synthetized as follows: (i) the migration energy decreases from 0·8 ev for a quench from 700°C to 0·6 ev for a quench from 1000°C; (ii) the annealing 'half-life' time decreases largely with increasing quenching temperature; (iii) a decrease of the volume of the specimen, proportional to the decrease of resistivity, is found; (iv) with quenching temperature an increasing fraction of the quenched-in resistivity is not annealed at low temperature (0·10 for a quench from 1000°C).

Koehler *et al.* (1957b) interpret their results in terms of single and multiple vacancies, especially to explain the effect of quenching temperature on the migration energy and on half-life time. The presence of larger clusters seems to be precluded especially by the results of point (iii).

On the contrary, in the case of aluminium the clustering is needed to explain, *inter alia*, the reduction in the number of jumps and the increase in E_m as the quenching temperature is increased from 470 to 600°C. This last fact is not observed in gold, as shown by point (i). In the same way, if we estimate the number of jumps n in gold, by using eqn. (2) and the half-life times and migration energies reported by

Koehler *et al.*, we find for the highest quenching temperatures $n \simeq 10^8$, and this is too large a value to be connected with clustering.

In conclusion, although multiple vacancies appear to exist in each metal, the tendency to clustering appears to be much stronger in aluminium than in gold. It is to be noted, however, that probably some clustering occurs in gold also, as shown by results of point (iv).

§ 5. Conclusions

The principal experimental results can be synthetized as follows: (1) notwithstanding the relatively large wire diameter, a large fraction of vacancies can be quenched-in; a formation energy of 0·76 ev is obtained from the lower quenching temperatures; (2) isochronal annealing after quenching from mean and high temperatures show the presence of two stages; after quenching from lower temperatures (400°c) only one stage is observed; (3) the first stage is centred at about room temperature and takes place at lower temperatures the higher the quenching temperatures; (4) the second stage is centred at about 160°c; there is some evidence of a slight dependence upon the way the first stage has taken place; (5) the amount of the second stage is related to the total increase of resistivity $\Delta\rho_0$, by the expression $\Delta\rho_0'' = a \,.\, T\rho_0^m$ where $m \simeq \frac{3}{2}$ and $a \simeq 3{\cdot}8 \times 10^{-2}$; (6) the migration energy for the defects of the first stage is $0{\cdot}58 \pm 0{\cdot}03$ ev for quenching from high temperature and somewhat lower ($\simeq 0{\cdot}4$ ev) for lower quenching temperatures; (7) the number of jumps n for annihilation in the first stage increases from $\simeq 10^4$ for quenching from 600°c to $\simeq 10^7$ for quenching from 550°c, and to $\simeq 10^9$ for lower quenching temperatures; (8) the activation energy for the second stage is about $1{\cdot}3 \pm 0{\cdot}2$ ev; (9) the fictitious formation energy of the second stage is $\simeq 1{\cdot}2$ ev.

The experimental results have been interpreted, in a qualitative way, in terms of clustering of vacancies; namely the first stage observed should be related principally to a coagulation of vacancies in clusters of some unspecified shape and the second stage to the subsequent dispersion by self-diffusion of these clusters.

Acknowledgment

The authors are much indebted to Professor F. Gatto for many useful criticisms and comments, and for his direct cooperation at the beginning of the work.

References

Bartlett, J. H., and Dienes, G. J., 1953, *Phys. Rev.*, **89**, 848.

Blewitt, T. H., Coltman, R. R., Holmes, D. K., and Noggle, T. S., 1957, *Creep and Recovery* (Cleveland: American Society for Metals), pp. 84–110.

Bradshaw, F. J., and Pearson, S., 1957, *Phil. Mag.*, **2**, 570.

Cottrell, A. H., 1957, *Vacancies and Other Point Defects in Metals and Alloys*, Institute of Metals Monograph, no. 23.

Coulomb, P., and Friedel, J., 1957, *Dislocations and Mechanical Properties of Crystals* (New York: J. Wiley and Sons Inc.), pp. 555, 576.

de Sorbo, W., and Turnbull, D., 1957, *Bull. Amer. phys. Soc.*, **2**, 262.
Dexter, D. L., 1956, *Phys. Rev.*, **103**, 107.
Federighi, T., 1958, *Acta Met.*, **6**, 379.
Koehler, J. S., Seitz, F., and Bauerle, J. E., 1957 a, *Phys. Rev.*, **107**, 1493; 1957 b, *Ibid.*, **107**, 1499.
Kuhlmann-Wilsdorf, D., 1958, *Phil. Mag.*, **3**, 125.
Levy, M., and Metzger, M., 1955, *Phil. Mag.*, **46**, 1021.
Maddin, R., and Cottrell, A. H., 1955, *Phil. Mag.*, **46**, 735.
McReynolds, A. W., Augustiniak, W., McKeown, M., and Rosenblatt, D. B., 1955, *Phys. Rev.*, **98**, 418.
Nowick, A. S., 1951, *J. appl. Phys.*, **22**, 1182.
Panseri, C., Gatto, F., and Federighi, T., 1957, *Acta Met.*, **5**, 50; 1958, *Ibid.*, **6**, 198.
Takamura, J., 1956, *Metal Phys., Japan*, **2**, 112.
Wintenberger, M., 1956, *C.R. Acad. Sci., Paris*, **242**, 128; 1957 a, *Ibid.*, **244**, 2800; 1957 b, *Vacancies and Other Point Defects in Metals and Alloys*, Institute of Metals Monograph, no. 23.

Growth of Electric Space-Charge and Radio Waves in Moving Ion Streams†

By J. H. Piddington
C.S.I.R.O., Radiophysics Laboratory, Sydney, Australia

[Received July 10, 1958]

Abstract

The following conclusions are reached:

(i) In a medium comprising two identical interpenetrating ion streams. four electric space-charge phenomena may occur. The ' fast ' and ' slow ' travelling waves do not concern us; the two effects of interest are non-travelling in a system in which the medium as a whole is at rest.

(ii) The first is most probably a set of evanescent waves. These have erroneously been interpreted as spatially growing waves and as the basis of the electron-wave and similar amplifiers.

(iii) The second effect is not an oscillation at all but an instability in the medium. A single space-charge cloud, however low its density, will, if its linear dimension is large enough, continuously increase in density with time. The mechanism disclosed is quite simple and does not require, as previously suggested, a series of ion clouds (that is, a spatial wave).

(iv) The effect may occur widely in nature, for example in the solar atmosphere (leading to patchiness and increased radio emission) in interstellar space and in the ionosphere (sporadic $-E$). It also provides a physical picture of the action of the electron-wave tube.

(v) An earlier criticism of Bailey's theory of radio waves growing in a medium which drifts along a magnetic field is consistent with special relativity theory. The consistency depends on a suitable definition of ' growth ', being increase in amplitude away from the source of the wave. The original definition—increase in amplitude in the direction of travel—indicates growth of virtually all waves to suitably moving observers.

(vi) The earlier criticism is also confirmed in discussing a previous Laplace transform analysis of the same situation plus a reflecting boundary. A new type of wave (the ' transverse space-charge wave ') described in this analysis is shown to be spurious and a corresponding theory of solar radio noise untenable.

§ 1. Introduction

Electric space-charge effects in interpenetrating ion streams have been the subject of numerous investigations. However, the different phenomena which may be present do not seem to have been adequately isolated, identified and described physically. The effects concerned may be important in nature, in interstellar space, in the sun's atmosphere and in the ionosphere, as well as in the laboratory. For this reason a better understanding is desirable and an attempt is made here to provide this for the simple case of two equal density streams.

† Communicated by the Author.

The different effects are isolated and it is found that, apart from ordinary travelling waves which do not grow or decay (collisions being neglected), there are two phenomena of interest. The first is an instability which may be described as a 'growing ion cloud'. It has been disclosed by previous mathematical analyses and its physical mechanism is discussed below. It is thought to be the basis of the two-stream laboratory amplifier and to have possible astrophysical significance, particularly in the field of radio astronomy.

The second effect has sometimes been interpreted as a spatially growing wave but there seems no evidence for this belief and the phenomenon is probably an ordinary evanescent wave as previously suggested (Piddington 1956a).

It seems appropriate to include here a discussion of 'growing' radio waves in a plasma drifting along a magnetic field. The reason is that the phenomenon involved is similar to one of those in the double ion stream and the discussion almost identical. A previous conclusion (Piddington 1956b), that the growth was spurious, was based on a steady-state analysis. It is confirmed by reference to a transient analysis and also shown to be consistent with the principle of (special) relativity.

§ 2. The Dispersion Equation of the Double-Ion Stream

Consider two interpenetrating streams, each of infinite extent and each consisting of N protons and N electrons per cm^3. Initially we consider an observer at rest relative to the whole plasma, the streams having velocities $\pm v$. The dispersion equation for disturbances having the form $\exp i(\omega t - kx)$ then has the form (Piddington 1956a, eqn. (10))

$$\frac{{\omega_0}^2}{(\omega - vk)^2} + \frac{{\omega_0}^2}{(\omega + vk)^2} = 1 \qquad . \; . \; . \; . \; . \; . \; . \; (1)$$

where ${\omega_0}^2 = 4\pi N\epsilon^2/m$ and ϵ and m are the electron charge (e.s.u.) and mass respectively.

Equation (1) is a biquadratic and so indicates that two pairs of waves may propagate in the medium. Each pair comprises two similar waves propagating in opposite directions. Some characteristics of these two types of wave may be displayed in a diagram where k is plotted against ω as in fig. 1 (*a*) where only positive values of ω and k are used and where the scales are simplified by putting $v = 1$ and $\omega_0 = \sqrt{\frac{1}{2}}$.

For values of $\omega > 1$ and $k > 1$, that is, for frequencies and wave numbers above certain critical values, the waves are ordinary travelling waves of the form $\exp i(\omega_r t - k_r x)$ with both ω_r and k_r real. The phase velocities of these waves correspond to the two values of ω_r/k_r so that those corresponding to curve A1 are slow travelling (velocity $< v$) and those corresponding to curve B1 are fast travelling waves. Neither of these waves shows either growth or decay and so they do not concern us directly here.

Nearer the origin O we have two other phenomena, which are the ones of interest.

(i) The A2 curve, obtained by assuming k real in eqn. (1).

The values of ω for $k<1$ are imaginary† and it might be presumed that the corresponding waves remained stationary in the medium but grew or decayed with time. To settle this point a Laplace analysis of a

Fig. 1

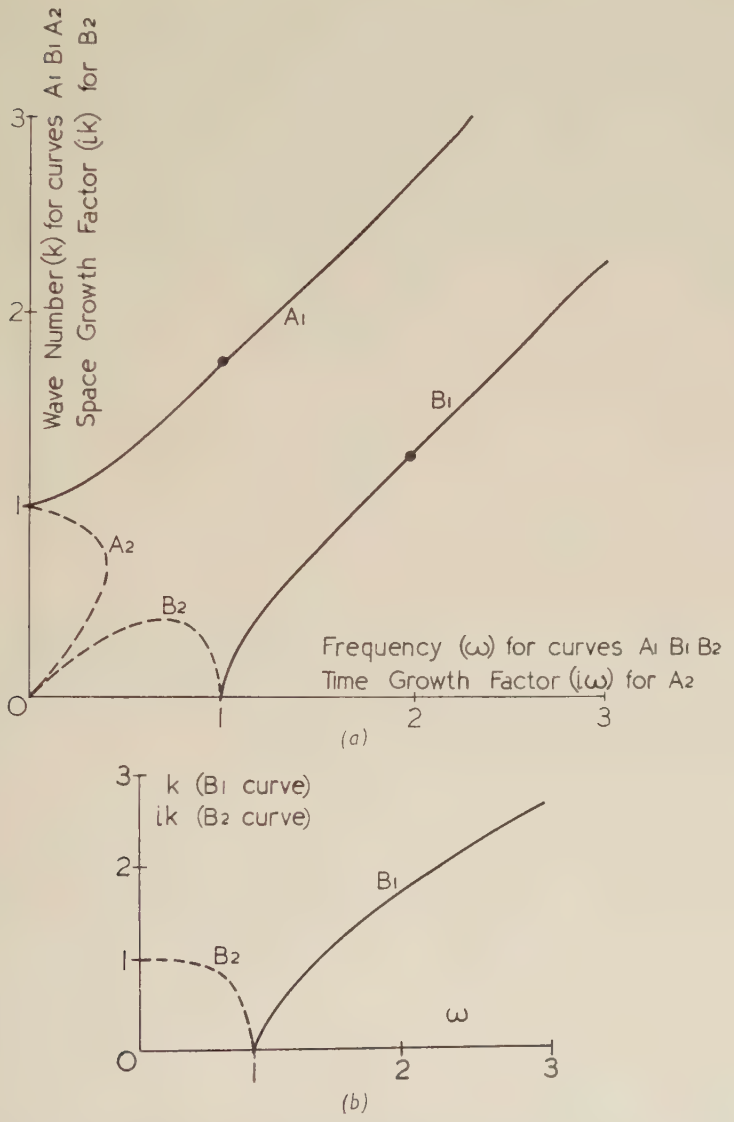

Graphical representations of the dispersion equations of two types of electron gas.

(*a*) The double-stream gas.
(*b*) Thermally agitated gas.

† The critical wave number $k=1$ applies when $v=1$ and $\omega_0=\sqrt{\frac{1}{2}}$. In general the values of ω are imaginary for $0<k<\sqrt{(2)}\omega_0/v$.

transient situation is required. No boundaries of the medium need be assumed ; the transient need only comprise an initial weak spatial distortion of the medium whose subsequent development is studied. A previous analysis of this type is discussed in the following section. The discussion is necessary because the results, as related to the dispersion equation, appear to have been misinterpreted.

(ii) The B2 curve, obtained by assuming ω real.

The values of k for $\omega < 1$ are then imaginary. The B curves of fig. 1 (*a*) may be compared with those of fig. 1 (*b*) for a gas whose ions have thermal motions only. The latter correspond to travelling waves (B1) and evanescent waves (B2). The B2 waves of the double ion stream may similarly be reflected waves shown schematically in fig. 2 (*a*) or, alternatively, exponentially growing waves as shown in fig. 2 (*b*). This ambiguity is discussed in § 4 below ; it cannot be resolved by the simple substitution-analysis methods described above and has been the cause of some confusion.

Fig. 2

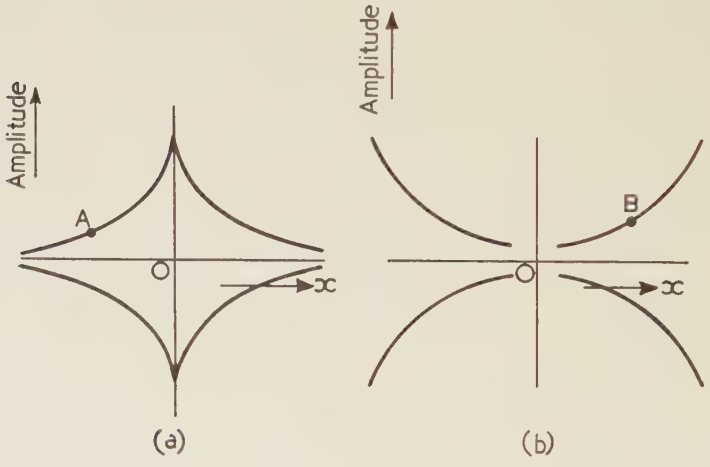

Spatially exponentially varying standing waves.
(*a*) Attenuated (evanescent) waves.
(*b*) Growing waves.

§ 3. The A2 Curve—Growing Ion Clouds

In an unbounded two-stream medium Twiss (1951 a) has assumed an arbitrary initial spatial distribution of charge at time $t = 0$ within a narrow region $0 < x < d$. He found that this ' ion cloud ' drifted with the plasma as a whole and at the same time steadily increased in amplitude. This simple and important result was later complicated by the introduction of a time modulation which is discussed in § 6 below but need not concern us as yet.

To relate Twiss' analysis to the steady-state phenomena described above consider a *single* spatial (δ-function) distribution of charge carried along by the drifting plasma. This distribution may be identified with a Fourier integral or, what is more easily visualized, a Fourier series having a large number of terms. Each term, or each wave, is defined by a particular value of k or a particular wavelength $2\pi/k$. Each value of k is related by eqn. (1) or graphically by fig. 1 (a) to two values of ω. Thus each term of the Fourier series corresponds to one or two points on the curves of fig. 1 (a). Every term of the Fourier series must correspond to a wave uniform throughout space and described by a *real* wavelength and *real* value of k. They correspond therefore to the curves A1, B1 and A2 (but not B2) of fig. 1 (a). The travelling waves (A1 and B1) cause the disturbance to spread, as found by Twiss, The A2 effect, with ω imaginary, causes it to increase in amplitude with time. Hence as far as growth is concerned, the analysis is concerned with the A2 effect, having imaginary values of ω.

The same phenomenon has also been discussed by Twiss (1951 a) in a steady-state analysis. He determined ω for *real values* of k and stream velocities u_1, u_2.

$$\omega = -\left(\frac{u_1+u_2}{2}\right)k \pm \omega_0\left[1+\frac{k^2(u_2-u_1)^2}{4{\omega_0}^2} \pm \left\{1+\frac{k^2(u_2-u_1)^2}{{\omega_0}^2}\right\}^{1/2}\right]^{1/2}. \quad (2)$$

Two of these roots are conjugate complex when

$$0 < k < \frac{2\sqrt{2}\omega_0}{u^2-u_1}. \quad . \quad . \quad . \quad . \quad . \quad . \quad . \quad . \quad (3)$$

Twiss referred to the growth corresponding to the imaginary part of ω as ' instability ' in the medium. On transforming to a coordinate system moving with the gas ($u_1+u_2=0$) and putting $u_2-u_1=2v$, eqn. (2) reduces to eqn. (1) and Twiss' ' instability ' is identified with the A2 curve of fig. 1 (a).

In relating his Laplace transform and steady-state analyses Twiss seems to have made an error. He concluded that the former, together with its indication of growth, was a different phenomenon to his ' instability ' which he considered unimportant. He believed that the Laplace transform analysis revealed a second phenomenon involving growth which he called ' amplification ' and which, in the steady-state analysis corresponded to imaginary values of k. This phenomenon he considered important being responsible for the operation of two-stream amplifiers.

These conclusions are inconsistent with the present discussion. As shown above the growth indicated by the Laplace analysis can only be associated with the A2 effect (k real, ω imaginary). This effect *is* important; a physical explanation is given in § 5 and in § 6 it is shown that operation of the two-stream amplifier may be explained by this effect. On the other hand there seems no evidence that Twiss'

'amplification' effect is important. It corresponds to k imaginary, ω real, that is to the B2 curve. In the following section it is suggested that this is probably an evanescent wave.

Using steady-state or substitution analyses, the A2 phenomenon (k real, ω imaginary) has been investigated by Bohm and Gross (1949a) and Kahn (1957) who obtain, within certain wavelength bands, a dispersion equation of the form $\omega^2 = -Ak^2$, where A is real and positive. This equation suggests the possibility of growth but may not be acceptable as full proof (Piddington 1956a) in the absence of a description of the mechanism of growth.

§ 4. The B2 Curve—Probably Reflecting Waves

The roots of the dispersion eqn. (1) corresponding to the B2 curve of fig. 1(*a*) (ω real, k imaginary) may be represented either by fig. 2(*a*) or fig. 2(*b*). The amplitude varies exponentially in space and, at a given point, it varies sinusoidally with time. The steady-state analysis cannot distinguish between the two possibilities of decaying and growing waves and since no appropriate Laplace transform analysis has been made the ambiguity remains.

However, it has been shown (Piddington 1956a) that previous demonstrations of growth of these waves were not valid. If the explanation given below of the growth mechanism in double-stream amplifiers is acceptable, then there remains neither theoretical nor experimental evidence that the B2 waves are growing waves.

Furthermore, when considered in connection with the double-stream amplifier, the waves of fig. 2(*b*) seem improbable, if not physically unrealizable. Between the input electrode and infinity (on the simple theory there is no limitation in length of the amplifier), at a given instant the perturbation space-charge is all of one sign and increases (spatially) exponentially. A half-cycle later it is all of the opposite sign, the change being caused by an applied signal which may be vanishingly small.

On the other hand, waves of the form shown in fig. 2(*a*) are well known and understood—they are evanescent waves. It seems very probable that the double-stream B2 waves are of this type.

§ 5. The Mechanism of the Growing Ion Cloud

There does not seem to be a satisfactory physical explanation of the instability or growing ion cloud phenomenon represented mathematically by certain roots of eqn. (1) and by curve A2 of fig. 1(*a*). Perhaps the omission is due to the fact that the effect has generally been regarded essentially as a *wave* phenomenon. Growth was thought to be due to a weak initial disturbance, say at $x = 0$, being carried along by one stream and growing due to velocity modulation. By interaction, the signal was then transferred to the second stream and carried back to $x = 0$ in an amplified form (Bohm and Gross 1949a).

There seems little justification for assuming that signals are carried along by the separate streams; rather do disturbances travel with or

propagate through the medium as a whole. Furthermore, it will be shown that the instability or growth applies for a single cloud and is simpler than the above ' feedback ' mechanism. It may be described briefly as follows: consider a neutral stream passing through a cloud of negative space-charge. On entering the cloud each electron will be slowed down by the space-charge field and on leaving, each electron will be accelerated to its original velocity. The corresponding effects on the heavy ions are neglected because of their much greater mass. The electron velocity in the cloud is lower than that outside the cloud and to maintain continuity of flow the electron stream density must be greater inside the cloud†. Thus the retardation of the electron stream contributes to the initially assumed excess electron density. This contribution *may be greater than the whole of the initially assumed cloud*, in which case the cloud density increases spontaneously. Two ion streams (or one stream plus a fixed grid system) are necessary because a space-charge cloud which tended to form in a single stream would be swept along with that stream and could not grow.

Fig. 3

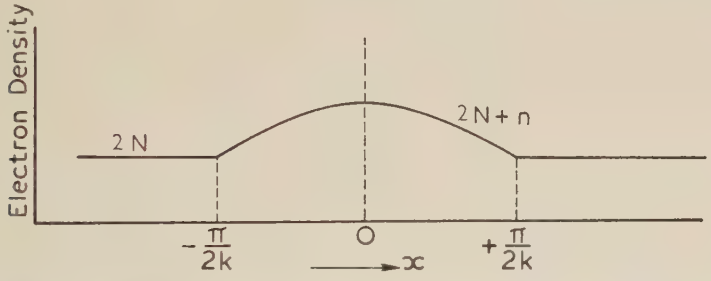

The electron density distribution in a hypothetical double electron beam.

Consider a neutral medium through which are flowing two electron streams of uniform density N and velocities along the x-axis of $\pm v_0$. Assume for the moment that a space-charge perturbation of the form shown in fig. 3 may exist; in the region $-\pi/2k < x < \pi/2k$ the total electron density is increased from its normal value of $2N$ to $2N+n$ where $n = n_0 \cos kx$. The perturbation is caused by inserting a cloud of electrons of density $n_3(x)$ attached to a rigid but permeable grid. The function n_3 must be determined as well as those n_0 and n_2, which are perturbations in the stream densities caused by the charged grid. We have, of course

$$n = n_1 + n_2 + n_3. \quad . \quad . \quad . \quad . \quad . \quad . \quad . \quad . \quad (4)$$

The presence of the space-charge cloud changes the stream velocities from $\pm v_0$, to $v_0 + v_1$ and $-v_0 + v_2$. To make the picture clearer physically,

† This situation corresponds to the ' travelling pulse ' solution of Bohm and Gross (1949 b). The correspondence does not extend, however, to the mechanism of growth developed here; the mechanism actually proposed by Bohm and Gross (1949 a) is mentioned above.

shielding grids may be assumed at the cloud boundaries so that the external field is everywhere zero and the stream velocities $\pm v_0$.

Poisson's equation gives (e.s.u.)

$$\frac{\partial E}{\partial x} = -4\pi e n_0 \cos kx, \qquad (-\tfrac{1}{2}\pi < kx < \tfrac{1}{2}\pi) \quad . \quad . \quad . \quad . \quad (5)$$

which on integrating and noting that by symmetry $E=0$ when $x=0$, yields

$$E = \frac{-4\pi n_0 e}{k} \sin kx. \quad . \quad . \quad . \quad . \quad . \quad . \quad (6)$$

Let us assume, subject to verification, that the situation is stable so that $\partial/\partial t = 0$. The equations of force and continuity for the first stream and for small perturbations are

$$v_0 \frac{\partial v_1}{\partial x} + \frac{e}{m} E = 0 \quad . \quad . \quad . \quad . \quad . \quad . \quad . \quad (7)$$

$$\frac{\partial}{\partial x}(N v_1 + n_1 v_0) = 0. \quad . \quad . \quad . \quad . \quad . \quad . \quad . \quad (8)$$

Combining with (6) and integrating again

$$n_1 = \frac{\omega_0^2 n_0}{v_0^2 k^2} \cos kx, \qquad (-\tfrac{1}{2}\pi < kx < \tfrac{1}{2}\pi) \quad . \quad . \quad . \quad . \quad (9)$$

where $\omega_0^2 = 4\pi N e^2/m$. The value of n_2 is the same, so that

$$n_3 = n_0 \cos kx \left(1 - \frac{2\omega_0^2}{v_0^2 k^2}\right). \quad . \quad . \quad . \quad . \quad . \quad (10)$$

This equation points directly to the physical reason for growth of ion clouds.

When $\sqrt{(2)}\omega_0/v_0 k < 1$ so that n_3 is a positive quantity we have the stable situation of a cloud of electrons of density n_3 attached to a rigid frame inserted in the double stream. The slowing down of the streams, given by

$$v_1 = \frac{-4\pi n_0 e^2}{m v_0 k^2} \cos kx,$$

causes an increase in density in each stream so that the resultant cloud has density $n > n_3$. The stability results from the mechanical forces exerted by the frame in holding the original cloud together; otherwise this would presumably dissipate as a set of travelling waves.

Now increase the dimensions of the cloud until $\sqrt{(2)}\omega_0/v_0 k = 1$ and $n_3 = 0$. The situation is simpler, as the original cloud held by the frame is dispensed with. A perturbation of this critical size (the wavelength $\lambda = \sqrt{(2)}\pi v_0/\omega_0$) is self-sustaining and again our assumption that $\partial/\partial t = 0$ is justified.

On further increasing λ a new situation arises; an initial assumed cloud has such a powerful effect in slowing and concentrating the streams that the resulting cloud is more dense than that assumed (n_3 negative), the effect being independent of the assumed density of the original cloud.

The more dense cloud in turn causes an even more dense cloud and so on to continual growth—for disturbances beyond a critical size the medium is unstable. The assumption $\partial/\partial t = 0$ no longer holds so that the full equation of force and continuity become necessary to determine rate of growth; however the simpler equations served their purpose in showing when and how growth occurred. The growth criterion $k < \sqrt{(2)}\omega_0/v_0$ is the same as that defining curve A2 of fig. 1 (*a*).

The above arguments may be modified to show that a cloud of positive space-charge (an electron deficiency) also grows, the electron streams being attenuated in passage. Growth might also be anticipated when a single electron stream moved past stationary positive ions (an electric current).

The effect is essentially an instability rather than an oscillation (where an initial distortion is resisted and replaced by one of opposite sign). However, as seen below, to a suitably moving observer a travelling spatially growing wave may be simulated.

§ 6. Growing Ion Clouds in Nature and in the Laboratory

In solar atmosphere clouds of ionized gas are seen to move with velocities up to 10^3 km sec^{-1} or more. Near the borders of these clouds there must be double-stream regions where space-charge clouds may grow. The minimum extent of an electron cloud which grows spontaneously is given by $\lambda = \sqrt{(2)}\pi v_0/\omega_0$. In the corona where $N = 10^8$ cm^{-3} the values of λ for cloud velocities of 10^6, 10^8 cm sec^{-1} ($v_0 = 5 \times 10^5$, 5×10^8 cm sec^{-1}) are 0·004, 0·4 cm. This may be compared with the collision distance of electrons, about 10^8 cm for a gas temperature of 10^6 °K. It is evident that the extent of the double-stream region, limited to the electron collision distance, is ample to provide growing electron clouds so that every slight irregularity tends to grow into a dense space-charge cloud.

Possible secondary effects of small ion clouds in the solar atmosphere are of interest. They create localized electric fields which accelerate electrons passing through or near the clouds. This in turn causes a type of thermal radio emission as discussed by Hoyle (1953) and Piddington (1954). The latter showed that under ideal conditions, when all the electrons exist in separate clouds, the emission may be increased over the free-free value by a factor $0{\cdot}002\,(v_e/f)^2 N$. v_e is the electron (thermal) velocity, f the radio frequency and N the electron density. For a gas temperature of 10^6 °K, $v_e \sim 7 \times 10^8$ cm sec^{-1} and for an electron density of 10^8 cm^{-3} the factor at 100 Mc/s is about 10^8. It seems unlikely that the ideal conditions required would ever be remotely approximated but even so, the factor is so large that the effect may be important in contributing to solar radio emission.

Solar radio emission also contains components of such high intensity that their origin would seem to require the ordered motion of large numbers of electrons rather than random (thermal) motions of individual electrons. The space-charge clouds seem to provide a possible basis for such an effect, provided there are localized irregularities in the gas density and

velocity. The emission would result from the 'collision' of two clouds rather than of a single electron with a cloud.

The electrostatic energy of an electron cloud is provided at the expense of the kinetic energy of the streams which are consequently slowed. Khan (1957) has considered this effect in connection with the collision of interstellar gas clouds whose relative motion, he concluded, might be arrested because of the instability of the system. The theory raises interesting possibilities but does not, however, consider the motions of the heavy ions which carry most of the gas kinetic energy.

Yet another effect is revealed when account is taken of collisions between particles of the two streams. This provides ions which do not share the streaming velocities and so may become permanent parts of the ion clouds. A cloud of electrons will attract positive ions and so create a co-existing neutral gas cloud. This effect may be important in the solar atmosphere where there is evidence of small-scale irregularities in the gas density. It may also play a part in creating ionospheric irregularities such as sporadic-*E* for which no satisfactory explanation seems available.

The growing ion cloud or A2 effect also appears to be the basic mechanism of the two-stream amplifier (electron-wave tube and similar devices). However, whereas the A2 effect shows growth in time (k real, ω imaginary), the two-stream amplifier shows spatial growth (k complex, ω real). The apparent discrepancy lies in the assumed methods of introducing the waves into the medium. In the former case a wave of uniform amplitude is assumed already present throughout the medium at a given instant so that $k=k_r$ and $\omega=-i\omega_i$, where k_r and ω_i are real and positive. In the second case a sinusoidally varying input signal creates a series of identical, equally spaced ion clouds in the medium moving with velocity U (the two streams have velocities $U+v$, $U-v$) past the emitter. These drift along, each growing in time at the rate given by $\exp \omega_i t$. In a time interval t, a cloud moves a distance Ut and so shows an apparent *spatial* growth given by $\exp \omega_i x/U$. Thus the appropriate value of k is $k_r+i\omega_i/U$; as before, for an observer moving with the stream $\omega=-i\omega_i$. In the two-stream amplifier the observer is assumed fixed as the emitter so that a Galilean transformation, involving a velocity change $-U$, is necessary. The value of k is unchanged, in this transformation the value of ω is increased by an amount Uk so that

$$k=k_r+\frac{i\omega_i}{U}, \quad \omega=-i\omega_i+U\left(k_r+\frac{i\omega_i}{U}\right)$$
$$=Uk_r.$$

These expressions correspond to the type of wave found in the two-stream amplifier†.

† Twiss extended the simple situation described in § 3 above by assuming a time modulation, at a new arbitrary frequency Ω, of the spatial distribution of charge in the narrow region $0<x<d$. Since this region drifts through the gas the result is a series of equally spaced ion clouds released with increasing time delays. The physical growth mechanism is unchanged but the situation corresponds with the two-stream amplifier.

The early theory of double electron-stream amplifiers (see, for example, Pierce 1948) has been criticized (Piddington 1956 a) on the grounds, briefly, that the same theory would show 'growth' of any reflected wave in any medium Pierce and Walker (1956) stated in reply that "no definitive conclusions can be drawn from it (the steady-state analysis) alone". They added that a Laplace transform analysis *is* capable of providing such conclusions.

This difference may now be clarified in terms of the phenomena referred to here as the A2 and B2 effects. The former (the growing ion cloud) is an instability in the medium by which kinetic energy of relative drift of the two streams is converted to electric potential energy. It is essentially a continuous, non-oscillatory process but as seen above may be made to appear as a spatially growing oscillation. The B2 effect was the basis of the earlier criticism, being accepted by Twiss (1951 a) and others as an 'amplification' effect or spatially growing oscillation of the type illustrated in fig. 2 (*b*). There appears to be no evidence for this conclusion; the effect is probably an ordinary evanescent wave as previously suggested.

§ 7. Growing Radio Waves

As seen above, an evanescent wave may appear to be a spatially growing wave when both observer and emitter drift through the propagating medium. This applies equally for radio as for electric space-charge waves and is the basis of a previous criticism (Piddington 1956 b) of a theory of growing radio waves. For completeness the earlier discussion must be extended as follows:

(*a*) To include the boundary problem, solved by the method of Laplace transforms by Twiss (1951 b), who concluded that real wave growth *could* occur. This is done in § 8 below.

(*b*) To show that, contrary to a recent assertion (Bailey 1956)†, the previous criticism is consistent with Einstein's principle of (special) relativity. This is done in the following paragraphs.

The dispersion equation for radio waves of the form $\exp i(\omega t - kx)$ in a plasma with mass drift along a magnetic field has been given in a simple form by Twiss (1951 b).

$$k = \pm i\alpha + U\beta \qquad . \; . \; . \; . \; . \; . \; . \; . \; (11)$$

where α is a function of ω and is real within the wavebands concerned, U is the velocity of the gas relative to the observer and β is a (real) constant. When U is small, even vanishingly small, one wave has a positive phase velocity (in the $+x$ direction) and increases in amplitude in that direction.

† Repeated references in this note to 'views about the transfer of energy' together with a simple illustration that the transfer of kinetic energy of a particle is not invariant, imply that the earlier criticism of Bailey's theory was based on energy considerations. This was not the case: as shown below a discussion of relative wave amplitudes was sufficient to show the theory untenable. Energy did not and need not enter into the arguments.

Bailey (1950) interpreted this as a spatially growing wave but an alternative explanation is that the wave is the left-hand wave of fig. 2 (*a*) moving to the right and growing to the right but *decaying* spatially away from its source at $x=0$. The wave moves because the gas drifts relative to observer and emitting boundary (Piddington 1956 b).

The basic equations used in the original theory (Bailey 1950), the theory itself and its criticism are all independent of considerations of energy. We are concerned with the *amplitude* of the wave as a function of time and space. Further, since only small velocities need be invoked, transformations between relatively moving systems are Galilean. Hence wave amplitudes and the direction in which the amplitude increases are independent of the observer.

It is the physical significance of this (invariant) direction of spatial growth that is the point at issue. Bailey relates it to the direction of positive phase velocity which, in the wavebands concerned, is merely the direction of drift of the gas. Using this criterion any evanescent wave may show growth. A more satisfactory criterion of growth is that the wave amplitude should increase in the direction away from the boundary at which the wave is introduced into the medium concerned.

The reality of wave growth defined in this way is invariant and so renders the original criticism consistent with the principle of special relativity.

§ 8. The Transient Analysis

Twiss (1951 b) has described and analysed a laboratory experiment corresponding to Bailey's theory of radio waves growing in a plasma with a mass drift along a magnetic field. The experiment is illustrated schematically in fig. 4. Media I and III are vacua and Medium II a plasma drifting along a magnetic field. A transverse electromagnetic (radio) transient is assumed incident on the boundary $x=0$ at time $t=0$. The boundary $x=d$ is a metallic reflecting surface and the field in the region $0<x<d$ is investigated at times $t>0$.

Before undertaking the Laplace transform analysis Twiss derived the appropriate (steady-state) dispersion equation. He modified the corresponding equation for the two well-known circularly polarized radio waves ('ordinary' and 'extraordinary') propagated along a magnetic field in an ionized gas

$$c^2k^2=\omega^2-\omega_0^2(1\pm\Omega/\omega)^{-1} \qquad . \quad . \quad . \quad . \quad . \quad (12)$$

where ω_0 and Ω are the plasma and gyro-frequencies and c the velocity of light. The modification was a Galilean transformation to an observer moving with the emitter (ω assumed real) relative to the gas†. The

† The dispersion equation is then of the third degree and Twiss has claimed that a third type of wave, a "transverse space-charge wave", is present. Before considering wave growth it is well to be sure which wave is under discussion. To this end it is shown in Appendix I that the 'transverse space-charge wave' has no reality and that the only waves present are the original 'ordinary' and 'extraordinary' waves viewed by a (slowly) moving observer.

appropriate dispersion equation then has the familiar form (neglecting electron collisions) of eqn. (11) where β is real and, *within certain wavebands*, α is also real. One of these waves evidently grows spatially in the $+x$ direction and one decays. Twiss used the transient analysis to find if the growing wave appeared in Medium II (fig. 4).

Part of the transient solution revealed waves travelling in the $+x$ direction and decaying. Twiss concluded that if another part revealed waves travelling in the $-x$ direction, then these must be growing waves. Part of the solution (Twiss 1951 b, § 5, line 4) *did* correspond to waves travelling in the $-x$ direction. This was shown by the fact that the contribution made by this term to the electric field at any plane x was identically zero until a time $t \geqslant c^{-1}(2d-x)$ where $x=d$ is the reflecting boundary of Medium II. The waves concerned must have been reflected and so must be travelling in the $-x$ direction. Twiss concluded that this result indicated the presence of growing waves.

Fig. 4

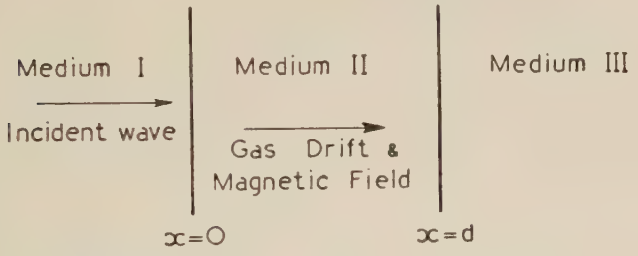

Boundary conditions for ' growing ' electromagnetic waves.

The error in this argument results from the fact that the wave shown travelling in the $-x$ direction had an infinitely high frequency. The term in Twiss' transient solution with which we are concerned comprises a set of radio waves of all frequencies ($0<\omega<\infty$). Above the critical frequency, that is in the frequency range where α of eqn. (11) is imaginary, the waves are ordinary travelling waves, not growing or decaying. In particular the wave of infinite frequency is not affected by the medium at all and so travels with the velocity of light and returns to the plane x in time $t=c^{-1}(2d-x)$. It was this wave which Twiss used in testing for reflected waves and the answer was just as anticipated from simple theory. However, this wave is not a growing wave so that the presence of a growing wave in Medium II has not been demonstrated.

According to eqn. (11) and to Bailey's theory, growth may occur only in certain wavebands where α is real so that the waves have the form $\exp \pm \alpha x \exp i(\omega t - U\beta x)$. Viewed in a frame moving with the gas ($U=0$) these are standing waves and so cannot be reflected at the boundary at $x=d$ and cannot travel against the direction of gas flow. Hence there

are no exponentially spatially varying waves in Medium II travelling in the $-x$ direction; no growing waves can be present.

Acknowledgments

I derived much pleasure and information from several interesting discussions with Dr. R. Q. Twiss. Helpful suggestions concerning the presentation were made by Dr. D. F. Martyn.

APPENDIX 1

Waves in a Drifting Gas

When ionized gas drifts along a magnetic field the dispersion equation for electromagnetic waves is modified from eqn. (12) above by the transformation $\omega_1=\omega-Uk$, $k_1=k$. Each of the two equations is now of the third degree suggesting that instead of two 'ordinary' and two 'extraordinary' waves there are now three in each case. We will consider the physical significance of the third wave.

It might be suggested as obvious that the mere motion of an observer along an existing wave (or waves) could not create another wave. Twiss explains the third wave as due to the observer's drift past successive layers of gas in which the electrons have different (transverse) motions, so creating a wave of velocity $\sim U$. However, all the electron motions are integral parts of the radio waves which existed prior to the drift and are only modified by the drift. In a linear medium they cannot create a fresh wave. It remains to explain the fact that three different values of k satisfy the new dispersion equation.

This is best done by plotting values of k against ω as shown in fig. 5 for either radio wave (the extraordinary wave is chosen) in the absence of drift. For any particular value of ω, say ω_a, there are two values of $k=\pm k_a$ found by drawing a vertical line to cut the curves. Similarly for ω_b we find $\pm k_b$. Now introduce a drift and for the two unchanged values of k (in a Galilean transformation $k_1=k$) we find two new values of frequency given by

$$\omega_{1a}=\omega_a-Uk_a, \quad \omega_{1b}=\omega_b-Uk_b.$$

In effect the diagram is now drawn in skew axes, the new points corresponding to ω_{1a}, ω_{1b} having moved to the left of the old as shown. As the rate of drift increases slowly the points move further to the left but that corresponding to ω_{1b} moves faster and eventually overtakes ω_{1a} at the point marked ω_1. The skew axis is now parallel with the dashed line which passes through three points marked k_a, k_b and k_c, corresponding with three waves having these propagation constants.

This does not mean that a new type of wave has been introduced but that three extraordinary radio waves, having different wavelengths, all appear, to a moving observer, to have the same frequency ω_1. The

reason is that, because of their different wavelengths, they have different Doppler shifts, thus compensating for the differences in frequency noted by a stationary observer. Figure 5 shows only real values of ω and k but the same arguments hold when one or other is imaginary.

Fig. 5

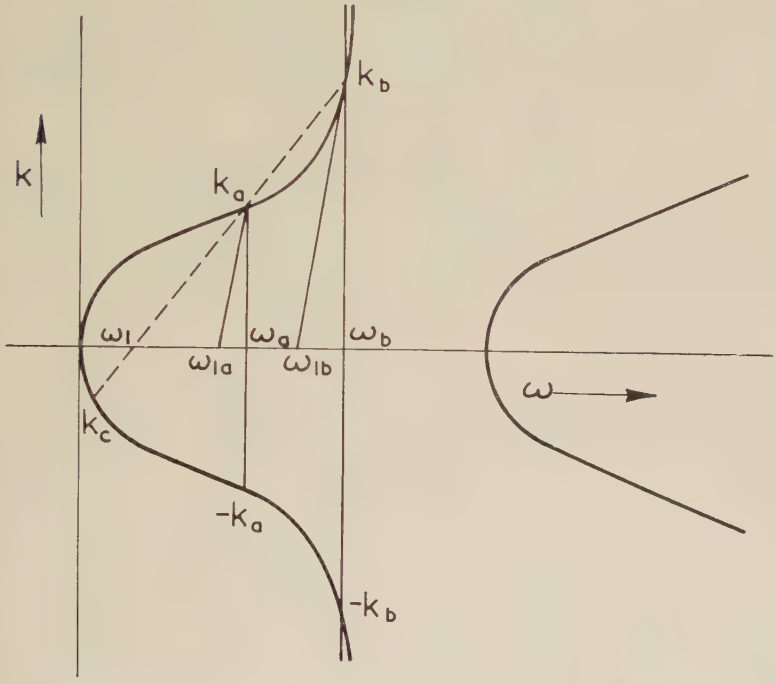

A graphical representation of the dispersion equation of transverse (radio) waves propagated along a steady magnetic field.

If this conclusion is correct it removes an inconsistency with a previous investigation (Piddington 1955) in which it was concluded that in a magneto-ionic medium only four different waves are possible. Apparent additional waves evident to moving observers appear to be spurious. The present conclusion would also invalidate Twiss' (1952) theory of sunspot radio noise.

References

Bailey, V. A., 1950, *Phys. Rev.*, **78,** 428; 1956, *Ibid.*, **106,** 1356.
Bohm, D., and Gross, E. P., 1949 a, *Phys. Rev.*, **75,** 1864; 1949 b, *Ibid.*, **75,** 1851.
Hoyle, F., 1953, *Nature, Lond.*, **172,** 296.
Kahn, F. D., 1957, *J. fluid Mech.*, **2,** 601.
Piddington, J. H., 1954, *Nature, Lond.*, **173,** 482; 1955, *Phil. Mag.*, **46,** 1037; 1956 a, *Aust. J. Phys.*, **9,** 31; 1956 b, *Phys. Rev.* **101,** 9.
Pierce, J. R., 1948, *J. appl. Phys.*, **19,** 231.
Pierce, J. R., and Walker, L. R., 1956, *Phys. Rev.*, **104,** 306.
Twiss, R. Q., 1951 a, *Proc. phys. Soc. Lond.* B, **64,** 654; 1951 b, *Phys. Rev.* **84,** 448; 1952, *Nature, Lond.*, **169,** 185.

Charged Particles Emitted from Aluminium on Bombardment with 14 MeV Neutrons†

By P. V. March and W. T. Morton
Department of Natural Philosophy, University of Glasgow

[Received July 4, 1958]

Abstract

The energy spectra of the charged particles emitted from aluminium on bombardment with 14 Mev neutrons have been measured for the angular intervals 16–48° and 132–164°. Groups of protons corresponding to known levels in ^{27}Mg were found. The ratio of the differential cross section for the forward angular interval to that for the corresponding backward interval was found to be 2·6.

§ 1. Introduction

In previous studies of the reaction ^{27}Al(n, p) at 14 Mev (Allan 1957, Colli and Facchini 1957, Brown *et al.* 1957, and Haling *et al.* 1957) peaks in the energy spectra of the protons emitted have been observed and a preference for proton emission in the forward direction has been noted. However in none of these studies were the statistics and resolution sufficient to make a detailed comparison of the spectrum at forward angles with that at backward angles.

This paper is a report of such a comparison in which photographic emulsions were used to detect the protons.

§ 2. Experimental Procedure

2.1. *Apparatus*

A schematic diagram of the apparatus is given in fig. 1. The 150 kev deuteron beam of the Glasgow H.T. set was incident on a tritium–zirconium target producing neutrons by the T(d, n)^{4}He reaction. At 90° to the deuteron beam and in the horizontal plane, a wedge-shaped iron collimator, 10 in. in length and 1·5 in. in height with a tapered rectangular hole through its centre, produced an approximately uniform beam of neutrons with an energy of 14·1 ± 0·1 Mev. At the centre of the brass exposure box the neutron beam was 1·5 cm in height and 3 cm in width. The box, 7 in. × 3 in. × 1·5 in., was lined with gold, 400 μ in thickness, to shield the photographic emulsions from external sources of protons (gold has a very small (n, p) cross section). An aluminium foil 14 mg/cm^2 in thickness was stretched across the centre of the box with its plane perpendicular to the neutron beam. Ilford C2 nuclear research emulsions,

† Communicated by Professor P. I. Dee, F.R.S.

Fig. 1

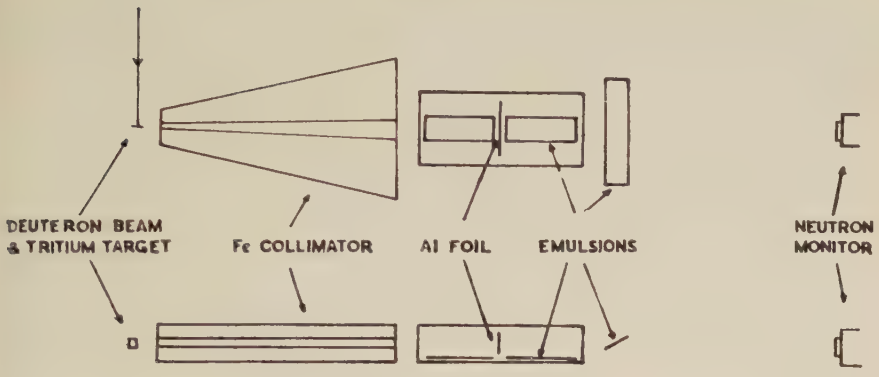

Diagram of apparatus.

Fig. 2

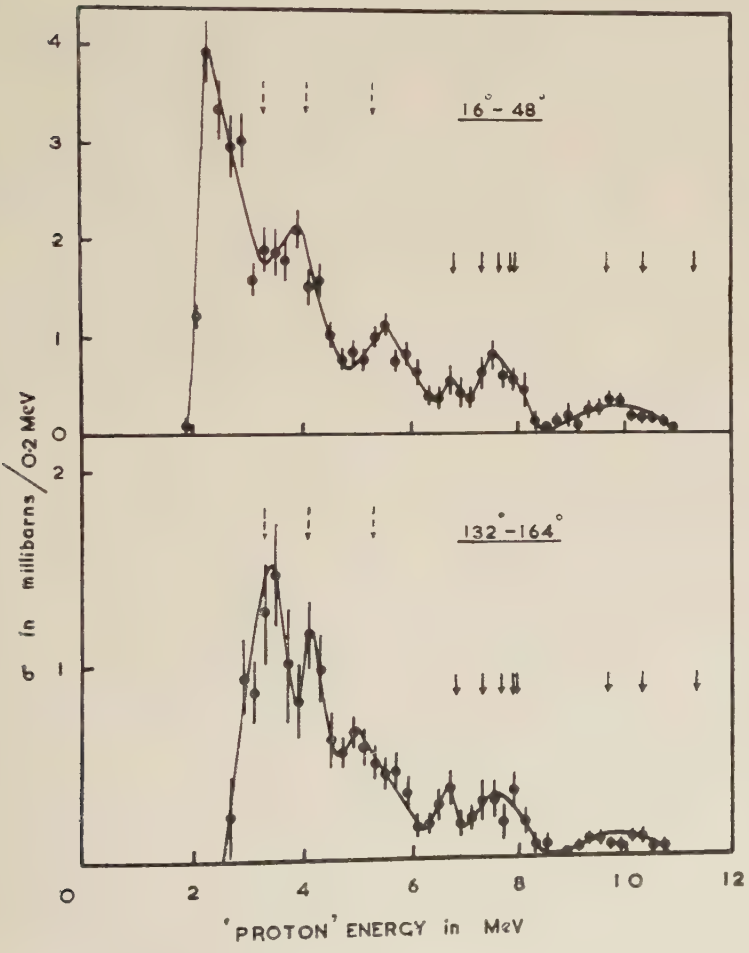

Energy spectra of ' protons ' in the centre of mass system.

400 μ in thickness, were placed below the beam on either side of the target foil with the emulsion surface horizontal. The neutron beam on emerging from the exposure box passed through a nuclear emulsion inclined at 30° to the beam and then to a plastic scintillator 2 metres away which was used to monitor the exposure.

2.2 *Examination of the Emulsions and Subtraction of Background*

The emulsions were scanned using $\times 50$ oil immersion objectives and $\times 10$ eyepieces for tracks of charged particles which entered the surface of the emulsion and appeared to originate at the aluminium foil.

The areas scanned in the forward and backward directions were symmetrical about the target foil and subtended angles at the foil of 16–48° and 132–164° respectively to the direction of the incident neutrons.

The range, angle of dip and the projected angle of each track accepted was measured. Assuming that the tracks were produced by protons, the ' proton ' energies were obtained using the range energy tables of Rotblat (1951). Some of these tracks will be due to deuterons and α-particles, the latter will have little effect on the spectra because an α-particle with the maximum energy possible would correspond to a 3 MeV ' proton ' in fig. 2.

Table 1

Angle	16°–48°	132°–164°
Area scanned	0·513 cm²	0·441 cm²
Tracks accepted	2123	741
Background contribution	307	118
Tracks from Al foil	1816	623

The background for the forward direction was determined by scanning the corresponding backward area for tracks whose projected angles and dips fell within the ranges of acceptance used in the forward direction. The background for the backward direction was determined using a similar procedure. This method is probably valid since the areas scanned are both close to and symmetrical about the centre of the exposure box and well away from the ends where most of the local background is produced. The numbers of tracks found and the background subtraction are given in table 1.

2.3. *Correction for Energy Loss*

Protons originating within the aluminium foil lose energy before emerging from the foil. Allowance was made for this loss by adding to the observed energy of each ' proton ' the energy it would have lost in traversing half the thickness of the foil, taking account of the angle of

traversal. Thus protons having ranges in the emulsion corresponding to energies of 2 MeV, 6 MeV and 10 MeV were considered to have had initial energies of $2{\cdot}75 \pm 0{\cdot}75$ MeV, $6{\cdot}4 \pm 0{\cdot}4$ MeV and $10{\cdot}2 \pm 0{\cdot}2$ MeV respectively.

2.4. *Determination of the Neutron Flux*

The extent of the beam and the flux of neutrons in it were determined from the emulsion exposed directly to the beam. At various positions across this emulsion, a known volume of emulsion was scanned for protons resulting from the collision of the incident neutrons with the hydrogen present in the emulsion. These recoil protons produce the majority of the tracks observed within the emulsion and are easily identified by applying the relationship,

$$Ep = (14{\cdot}1 \pm 0{\cdot}1)\cos^2,\theta$$

where Ep is the energy of the recoil proton and θ is the spatial angle between the direction of the recoil proton and the incident neutron.

§ 3. Results

The energy spectra of the ' protons ', in the centre of mass system, for the two angular intervals are given in fig. 2. There are peaks in the spectra for both forward and backward angles. The solid line arrows drawn on fig. 2 indicate the position of known energy levels in the nucleus ^{27}Mg, the residual nucleus of the (n, p) reaction, measured using the reaction ^{26}Mg(d, p)^{27}Mg, e.g. Hinds *et al.* (1958). Reading from left to right, they are the ground state, 1·0, 1·66, 3·50, 3·56, 3·75, 4·13 and 4·75 MeV levels. The ground state (n, p) transition is not observed but the high energy peaks in both the energy spectra are in good agreement with the positions of the higher levels.

Some of the particles classed as protons will in fact be deuterons, the maximum possible energy for a deuteron would correspond to a ' proton ' energy of 5·3 MeV. Thus the peak at 5·6 MeV consists mainly of protons suggesting energy levels of ^{27}Mg in this region. At lower energies a peak occurs at about 4 MeV, an energy which might be expected to lie in the continuum of levels for ^{27}Mg.

The group of lowest energy ' protons ' of the spectra occur at different ' proton energies ' for the two angular intervals. This effect also appears in the results of Haling *et al.* The broken line arrows shown on the energy spectra indicate the ' proton energies ' corresponding to deuterons from (n, d) transitions to the ground, 1·8 and 3·0 MeV levels of ^{26}Mg (Endt and Kluyver 1954). It should be noted that the positions indicated do not allow for the assumption that the tracks were produced by protons made in correcting for energy loss in the target foil and in determining the centre of mass ' proton energy ' from the observed value. If the low energy ' protons ' were in fact deuterons these effects each displace the low energy end of the spectrum by about 0·3 MeV. Thus at the forward angles the spectrum would be displaced about 0·6 MeV towards lower

energies while at the backward angles the displacements would cancel out. The two low energy peaks in the spectra are thus consistent with the reaction $^{27}Al(n, d)^{26}Mg$, indicating that a large proportion of these particles are deuterons.

The ratio of the cross section averaged over the angular interval 16–48° to that averaged over the interval 132–164° for the different groups observed in the energy spectra is given in table 2.

Table 2

' Proton ' energy in MeV	2·0–3·8	3·8–5·0	5·0–6·4	6·4–8·6	>8·6	All energies
$\frac{\sigma_{16°-48°}}{\sigma_{132°-164°}}$	2·8	2·8	2·1	2·1	3·5	2·63

In obtaining the values given for the two low energy groups, the majority of the particles in the groups were assumed to be deuterons and accordingly allowance was made for the displacement of the spectrum for deuterons at forward angles as described above.

All the energy groups show a marked preference for emission at the forward angles. The ratio of the differential cross section for all particles emitted in the forward angular interval to that for the backward interval is 2·63 in good agreement with the value of 2·69 obtained by Haling *et al.* for the ratio of the differential cross section at 30° ± 15° to that at 150° ± 15°. However the absolute value obtained for the average differential cross section over the interval 16° to 48° is 19·5 ± 3 mb/steradian while that of Haling *et al.* is 9·8 mb/steradian at 30° ± 15°.

The asymmetry of the angular distributions of the high energy proton groups is probably due to the occurrence of direct interaction effects.

The preference for emission at forward angles of the low energy groups is another indication that they are deuterons. If they were protons from the (n, np) process as observed in heavier elements (March and Morton 1958), their angular distribution would be expected to be symmetrical about 90°, whereas a pick-up reaction of the type (n, d) would be expected to lead to the emission of deuterons at forward angles.

Acknowledgments

The authors wish to thank Professor P. I. Dee for his interest and encouragement; they also wish to thank Dr. H. Muirhead for useful discussions, Dr. A. M. Ward for help during the exposures, and Miss E. Rose and Miss J. Stewart for assistance with the microscope work. One of us (W. T. M.) would like to express his gratitude to the Department of Scientific and Industrial Research for a maintenance grant.

References

Allan, D. L., 1957, *Proc. phys. Soc. Lond.* A, **70,** 195.
Brown, G., Morrison, G. C., Muirhead, H., and Morton, W. T., 1957, *Phil. Mag.*, **2,** 785.
Colli, L., and Facchini, U., 1957, *Nuovo Cim.*, **5,** 309.
Endt, P. M., and Kluyver, J. C., 1954, *Rev. mod. Phys.*, **26,** 95.
Haling, R. K., Peck, R. A., and Eubank, H. P., 1957, *Phys. Rev.*, **106,** 971.
Hinds, S., Middleton, R., and Parry, G., 1958, *Proc. phys. Soc. Lond.*, **71,** 49.
March, P. V., and Morton, W. T., 1958, *Phil. Mag.*, **3,** 143.
Rotblat, J., 1951, *Nature, Lond.*, **167,** 550.

Etch Pits and Trigons on Diamond: I†

By F. C. Frank and K. E. Puttick‡
H. H. Wills Physics Laboratory, University of Bristol

and Eileen M. Wilks
Clarendon Laboratory, Oxford

[Received June 30, 1958]

Abstract

On the faces of a type I diamond octahedron of particularly good quality there have been observed clusters of trigons which appear to be associated with a centre of strain in the interior of the stone. The trigon patterns show features which can only have been the result of surface dissolution. These observations are discussed, and it is concluded that most trigons are etch pits; there is evidence that these particular trigons are centred on dislocations.

Possible explanations are considered for the fact that the usual laboratory etchants develop pits oppositely oriented to trigons.

§ 1. Introduction

The origin of the triangular depressions, commonly referred to as " trigons ", which are seen on all or practically all natural octahedral faces of diamonds, has long been a subject for dispute. The observation of these features has been notably advanced by Tolansky, who has given a fairly comprehensive description of them in published papers and a recent book. The two competing theories for their origin are (1) that they are etch pits or (2) that they are regions which have been surrounded by growth layers, but not filled in. Tolansky has argued strongly, but not, as he claims, conclusively, for the latter view. He has two lines of evidence : one that he found a case in which the base of a flat-bottomed trigon was at the same level as a neighbouring flat area, with an intervening plateau; the other that laboratory etching experiments do not reproduce the naturally occurring patterns. Chance cannot be excluded as the cause of the first of these : or indeed, it could be the result of a growth process without implying that this is responsible for all 'trigon' markings. They vary considerably among themselves, and the general family resemblance may to a large extent be simply attributed to the trigonal symmetry natural on a (111) face of diamond. The laboratory etching experiments provide negative evidence which can never be made complete. The case from these experiments is considerably weakened by the results of Omar and Kenawi (1957) who have etched diamonds (by

† Communicated by the Authors.
‡ Now at the Department of Metallurgy, University of Cambridge.

heating in low pressure air on a molybdenum strip) to produce patterns which have all the appearance of natural trigon markings, with one exception. The exception is that whereas the sloping sides of the natural pits on (111) are of the form $(1, 1, 1-\delta)$, with its permutations, making a bounding triangle in opposite orientation to the triangular face of the octahedron, those produced by Omar and Kenawi, in common with those of most other laboratory etching experiments, have the form $(1, 1, 1+\delta)$ making a triangle in the same orientation as the octahedral face. We may refer to these respectively as triangles in negative and positive orientation, and note that no other orientations of triangles are to be expected from the crystal symmetry : pits with any other bounding faces of a single form would have hexagonal outlines.

The observations to be described here were made on a good quality ' blue-white ' octahedral diamond of type I. On each face of this stone there is a fairly well-defined group of trigons, the approximate centre of which is in a line, perpendicular to the face, with the corresponding centre on the opposite octahedral face. The four lines intersect at a point within the stone (not its geometrical centre) which was the centre of a birefringent pattern observed in polarized light. Two such opposed faces, with the accompanying birefringent pattern, are shown in fig. 1 (*a*)–(*c*), Pl. 82.

A more detailed study of these trigon groups was made. For this purpose some method of contrast enhancement was necessary, and a very simple adaptation of a Vickers projection microscope was found to give good results. The 45° reflecting plate in this instrument (as used for metallography) is a half silvered aperture in a fully silvered plate, mounted on a movable slide. This may be partially withdrawn so that the fully silvered edge of the plate reflects the illuminating beam and at the same time obstructs part of the light reflected from the specimen. It has been pointed out by Zernike (1946) and demonstrated by Pratt and Lomer (1952) that such a stop in or near the back focal plane of the microscope gives rise to a ' schlieren ' effect which greatly accentuates apparent differences in surface slope. The best results were obtained in our case with the 16 mm objective, probably because the reflecting plate coincides most nearly with its back focal plane, while the loss of resolving power due to diminution of the objective aperture is not (as with lenses of higher power) particularly serious. A further gain in contrast can be obtained by inserting into the illuminating beam, slightly off centre, the circular stop provided for dark ground illumination.

The advantage gained with this arrangement can be seen by comparing figs. 2 and 3, Pl. 83, of the same field on the unsilvered diamond surface. Figure 2 is taken in normally incident light with the conventional metallurgical microscope; fig. 3 is a photograph by the schlieren method. Interferometric measurements have shown that the sides of the fainter pits to be seen in fig. 3 makes angles of the order of 10′ of arc with the main surface. Since this photograph was not taken with the stop in the position of maximum contrast, and these pits are not at the limit of visibility, it

does not seem unreasonable to suggest that with a silvered surface the angular sensitivity of this system could be increased to a minute or so of arc.

The trigons seen may be divided into two classes, ' strong ' and ' weak ', according to the inclination of their surfaces. All in the strong class, and almost all in the weak class, are of complete, i.e. non-truncated, inverse pyramidal form. In both classes a feature repeatedly observed is the precise contact of a corner of one triangular outline of a pit with a side of another. We consider this a very significant diagnostic feature for the origin of these pits. Wherever such contacts occur there is an associated depressed area, outside the individual pits, on either side of the contact. Such depressed areas have gently sloping floors, with orientations which may be approximately described as permutations of $(1+\epsilon, 1-\epsilon, 1-\epsilon')$, surrounded by steeper walls with the same $(1, 1, 1-\delta)$ slopes as the individual pits : each such outer wall is an extension of a face of an individual pit within it. This description applies to the greater part of the boundary of a depressed area, but there are portions of the boundary of a large depressed area where the step is relatively shallow and curves away from the $\langle 110 \rangle$ type of direction, and rarer places where it becomes straight again with a $(1, 1, 1+\delta)$ slope. Depressed areas may contain within them further depressed areas, whose steeper boundaries are again extensions of the faces of contained pits. The overall depth of all pits of the strong class on the one hand, or of all the weak class on the other, is about the same when reckoned from the outer plateau, that is, including the depth of the depressed areas in which they lie.

§ 2. The Formation of the Patterns

The process producing the pits, whether it be dissolution within, or growth without, must by its continuation enlarge them, and so, in time, cause neighbouring independent pits to impinge. The growth theory must, however, be subdivided into two versions : (i) that the trigon patterns are formed only in a final stage of growth ; and (ii) that they are present throughout the growth history of a diamond. Tolansky's discussion implies version (ii). For this version it is necessary that processes by which the pits are filled in, and are therefore conceivably capable of shrinking, also operate. On the assumption of etching, the outline of a pit may shrink by dissolution of the surrounding area. Consider therefore two adjacent pits as in fig. 4. They may approach the condition of contact either by enlargement from non-contact as in fig. 4 (*a*) or by shrinkage from overlapping as in 4 (*c*). The maintenance of contact indicated by our photographs, figs. 1 and 2, implies that as soon as this condition is passed, a new process operates so as to restore it. Passage from contact to fig. 4 (*a*) introduces no novel crystallographic feature into the situation : but passage from contact to fig. 4 (*b*) brings into existence two salient edges of form $\langle 1, 1, \bar{2}+\delta \rangle$ where the two pits meet, no salient edges of this kind being present before. We conclude

then that the development was in the direction contact to 4 (*b*). On the etching theory the interpretation is straightforward. It is natural to suppose that the presence of these salients, being of other form than the plainly resistant ⟨110⟩ edges, leads to accelerated dissolution, and produces the observed pattern in the manner detailed below. There does not, however, appear to be any means of interpreting the patterns from a growth theory. There is no basis in theory or analogous observation to suggest that the salient edges would accelerate growth. If, nevertheless,

Fig. 4

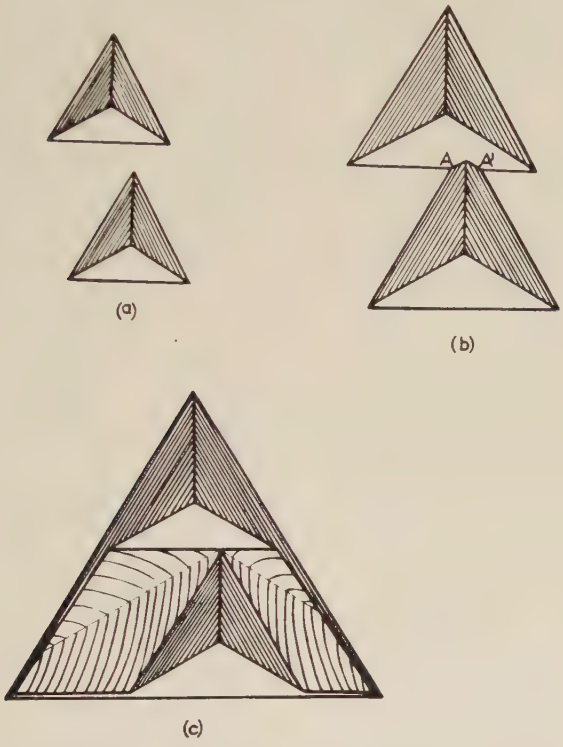

When two pits overlap, salient edges at A and A′ provide points of easy dissolution. Dissolution of the neighbouring surface proceeds until the position of exact contact is restored. A depressed area is formed enclosed by steps which are extensions of the original trigon faces.

they did that, so restoring contact by partially filling in the pits, we should be left without an interpretation of the adjacent depressed area which accompanies contacting pits. To explain the whole figure on the growth theory we require to understand how a change of situation at the point of contact causes growth layers to hold back at the remote boundaries of the depressed area. There does not seem to be any way in which this can be explained. Since on the other hand etching will explain the figures we conclude that etching produced them.

Along the ⟨110⟩ directions of diamond there are zig-zag chains of carbon atoms like those in the long-chain paraffins. Such chains parallel to any chosen ⟨110⟩ direction contain all the atoms of the crystal. The macroscopic habit of the crystal (always involving faces of the ⟨110⟩ zones, i.e. predominantly {111}, but also {001} and approximate {110} faces which are in fact more nearly ⟨110⟩-zone cylinders) together with the trigonal surface markings indicate that both in growth and in etching the extension or contraction of these ⟨110⟩ chains goes easier than the initiation of new ones or the breach of existing ones. We may reach a closer understanding of this by considering figs. 5 and 6. Figure 5 (*a*) shows in (111) projection the surface of a diamond which departs from (111)

Fig. 5

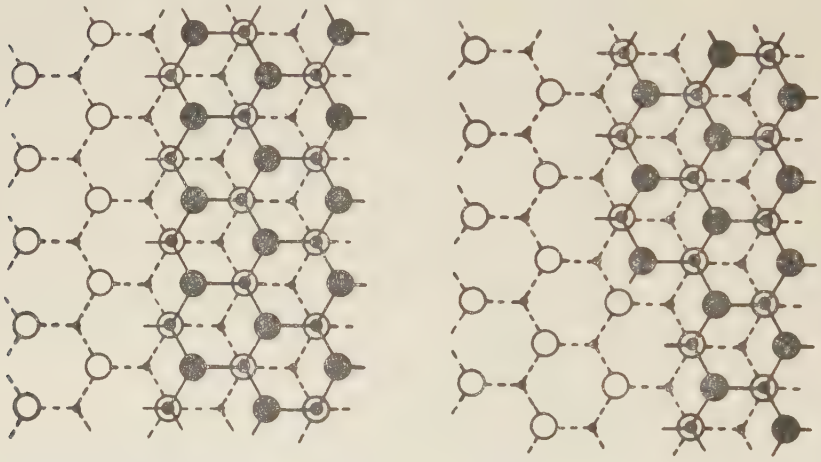

(*a*) Negative [110] step in (111): the monomolecular step in a $(1, 1, 1-\delta)$ vicinal face.

(*b*) Kinked negative step as in a $(1+\epsilon, 1-\epsilon, 1-\delta)$ vicinal face.

by having one monomolecular step along [110] of the kind present in $(1, 1, 1-\delta)$ vicinal faces. We shall call this a negative $[1\bar{1}0]$ step in the (111) face. All atoms of the peripheral zig-zag at this step are triply bonded to the crystal. An additional atom added anywhere is only singly bonded to the crystal. Figure 4 (*b*) shows this step with one kink in it, such as would be present in a $(1+\epsilon, 1-\epsilon, 1-\delta)$ vicinal face. The terminal atom at the kink is doubly bonded to the crystal: its removal leaves another doubly bonded atom, the removal of which leaves a kink of the same form as before. The same applies to the addition of atoms. The diamond crystal grows when atoms attach more frequently to such doubly bonded positions than they leave them, and dissolve when they leave more frequently than they attach. Growth or dissolution at such a step may be analysed into the production of such kinks and their propagation along the step.

Figures 6 (*a*) and 6 (*b*) show alternate configurations for a step along $[1\bar{1}0]$ of the kind present at a $(1, 1, 1+\delta)$ vicinal face. We call this a positive $[1\bar{1}0]$ step in (111). In either of these configurations the outermost row of atoms is doubly bonded to the crystal, and this bonding is

Fig. 6

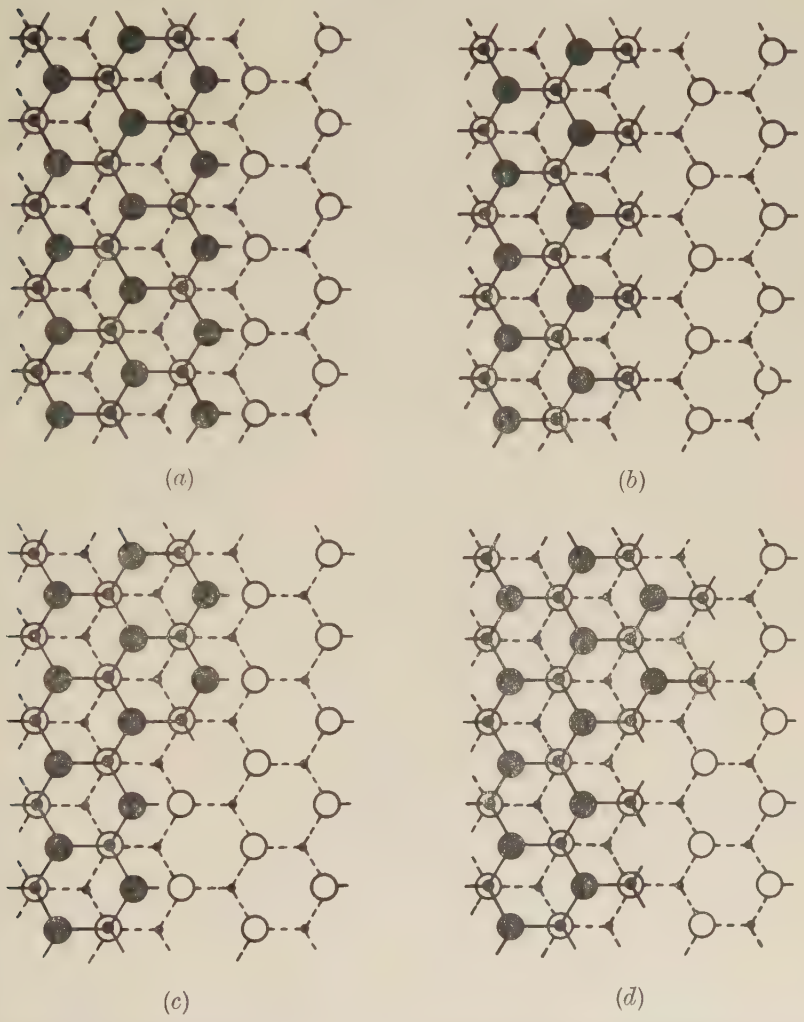

(*a*) Positive $[1\bar{1}0]$ step in (111): the monomolecular step characteristic of $(1, 1, 1+\delta)$ vicinal faces.
(*b*) Alternate configuration of the positive $[1\bar{1}0]$ step in (111).
(*c*) A kink in the positive $[1\bar{1}0]$ step, as in $(1+\epsilon, 1-\epsilon, 1+\delta)$ vicinal faces.
(*d*) Alternate configuration of the kinked positive [110] step in (111).

not changed when neighbouring atoms of the same row are removed. Removal of the outermost atom row from either of these configurations produces the other. Such steps can therefore be attacked piecemeal.

Their dissolution does not depend on kink propagation following a relatively difficult breach of the chain. The same applies in reverse for the addition of atoms in the growth process. The kink in this step, figs. 6 (*c*) and 6 (*d*), in fact provides one 'protected' atom, triply bound into the crystal, but a single 'protected' atom is of no great importance for the kinetics of dissolution or growth. The kink in a positive [110] step may be regarded as a short length of negative [101] or [01$\bar{1}$] step. Steps in any other orientation in the (111) face may be regarded as kinked positive or negative $\langle 1\bar{1}0\rangle$ steps. For example, there are two alternate configurations of a [11$\bar{2}$] step, in each of which there is an outermost row of atoms doubly bonded to the crystal, so that this type of step is also suitable for piecemeal attack, or growth.

This discussion leaves us in need of an explanation for the appearance of positive vicinals, $(1, 1, 1+\delta)$, in diamonds etched with potassium nitrate, or with oxygen, in the laboratory, and to a minor extent on nautrally etched diamonds as in fig. 3. It is suggested as a tentative hypothesis that in the presence of oxygen the positive $\langle 1\bar{1}0\rangle$ step becomes stabilized as –C–O–C–O– zig-zag chain, such as is present in the polyoxymethylene polymers of aldehydes, as shown in fig. 7. This suggests that to imitate

Fig. 7

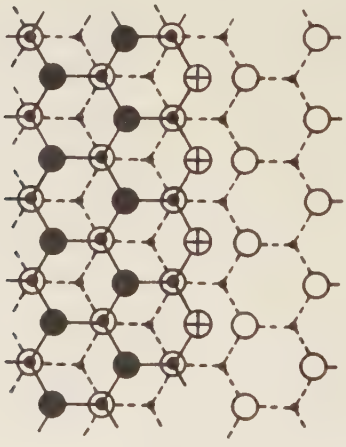

Positive step as in fig. 6 (*b*), with an additional line of oxygen atoms.

the natural patterns one should attempt to etch diamond with reagents furnishing only, or predominantly, monovalent atoms and radicles, such as halogens or hydrogen. Neither of these seems likely to have been the actual natural etchant, and etching by the water-gas reaction, which would be expected to attach predominantly hydrogen atoms and hydroxyl radicles to the diamond surface, is a plausible suggestion.

§ 3. Trigons as Indicators of Dislocations

The pyramidal form of most of these pits suggests that they may be centred on dislocations. This suggestion is supported by their location, in clusters on each face, around the foot of the perpendicular from the interior strain-nodulus: it is reasonable to suppose that the crystal grew around this centre, and that dislocations emanating from it would extend approximately along the normals to each face. The fact that there are essentially two populations of pits, deep and shallow, as may be seen in fig. 3 lends further support to this suggestion. Elementary dislocations in diamond would have Burgers vectors of the form $\frac{1}{2}\langle 110\rangle$. $\langle 110\rangle$ directions, considered in relationship to a (111) face, fall into two classes, half of them being parallel to the face, and the other half making an angle of 54° 44′ with it. The latter, having partially screw character with respect to the face, would be expected to provide points of particularly easy attack, and so give rise to ' deep ' pits. The former would make points of easier attack than the face in general, because of concentrated strain, but would probably not facilitate attack so much as the screw dislocations: they are more likely to be responsible for the shallow pits. This particular stone may be an unusually fortunate example. The relative rates of attack at the two kinds of dislocation end would be expected to vary widely with conditions in the medium: so also would the ratio of rate of attack at the dislocation itself to rate of lateral growth of the pit, which determines the steepness of its sides. In some circumstances there might be no attack except on the screw dislocations, and it is quite likely that only in fortunate cases do we have conditions of etching which produce pits on both classes of dislocations, while giving a good discrimination between them.

APPENDIX

This Appendix gives the results of a sample survey made by one of us (E. M. W.) of the slopes of the faces of pyramidal trigons on three diamonds. The first (classed as 'blue-white') is the stone with which the main text of the paper is concerned. The second is classed as 'fine white' and the third as 'glassy'. The figures for slope have been derived from measurements of lateral dimensions from photomicrographs, and of depth obtained by using either multiple beam Fizeau fringes or fringes of equal chromatic order (Tolansky 1948).

The reference surface with respect to which depth is measured is always the immediately surrounding flat, or nearly flat, area, which may itself be a depressed area with respect to the main surface. On this account slope has been taken as the preferable basis of comparison rather than depth. In general, however, 'steep' and 'deep' correspond; that is to say the lateral dimensions of pits on the diamonds studied do not vary very widely, nor does this variation appear to be correlated with depth: shallow trigons are on the average as wide as deep ones.

Not all diamonds are suitable for study, and some selection of specimens is necessary. Because of optical requirements the octahedron surfaces must be smooth, so only good quality stones can be used. The density of trigons on a face must not be too great, otherwise it becomes difficult to identify individual trigons in the focal plane of the spectrograph. On the other hand there must be adequate numbers of deep and shallow trigons to permit a numerical survey, and this condition eliminated some of the best quality stones which had no deep trigons and only a few shallow ones. The surface density of trigons on the stones finally chosen was of the order of 10^3 to 10^4 per cm^2, which was found to be a satisfactory compromise between the requirements.

In the course of the investigation some trigons with flat bases were observed. Although the number of flat-based trigons varies from stone to stone, they are in general rare. They have been disregarded in this survey.

The histograms, figs. A1, A2, A3 show the distribution of slopes for the three diamonds specified at the beginning of this Appendix. Each shows a bimodal distribution. Mean depths and slopes for the two groups in each of the three stones are presented in table A1.

Table A1. Mean Depths and Slopes of Pyramidal Trigons

Stone	Deep trigons			Shallow trigons		
	Depth Å	Slope minutes	Number measured	Depth Å	Slope minutes	Number measured
Blue white	9200	90	18	950	13	27
Fine white	5570	140	6	500	14	16
Glassy	3315	49	27	650	11	12

The variation in steepness found (within either the deep or the shallow group) would fairly certainly have been less if a survey had been limited to a restricted area on a stone, instead of pooling the results for a variety of places on several faces of any one stone, as was in fact done. That this is the case is shown by the results (table A2) for the five measured pits on the 'blue-white' stone (all of them deep ones) which fall in the area of Plate.

Table A2. Blue-White Diamond

Trigon number	Depth (Å)	Slope (min)	Reference surface
1	12170	117	main surface
2	8670	92	depressed area
3	7850	93	depressed area
4	11180	109	main surface
5	7690	107	depressed area

Fig. A1

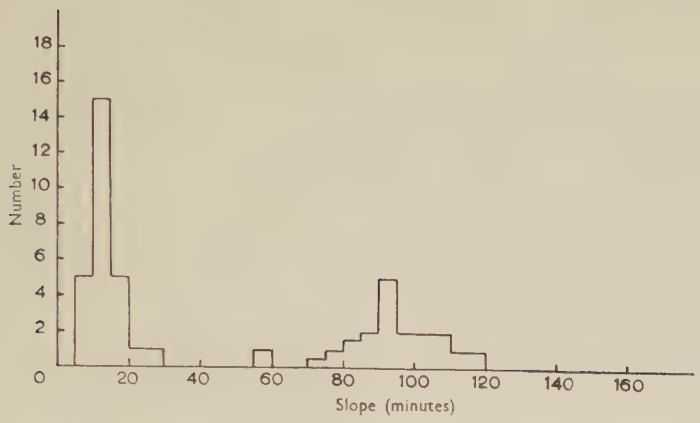

Histogram of trigon slopes: ' blue-white ' diamond.

Fig. A2

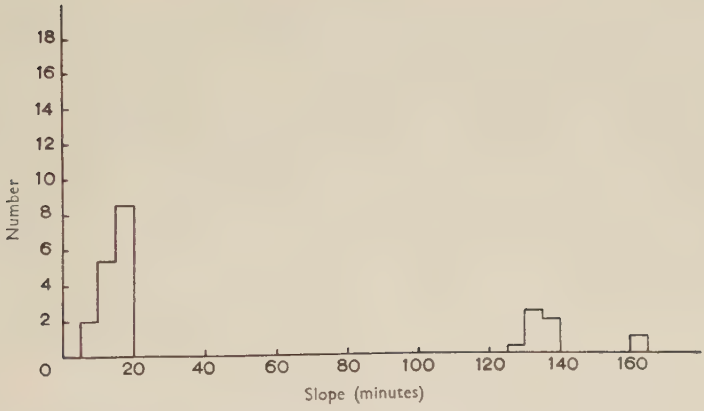

Histogram of trigon slopes: ' fine white ' diamond.

Fig. A3

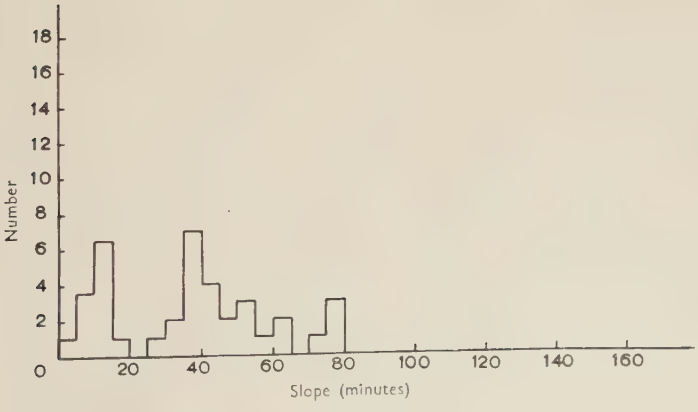

Histogram of trigon slopes: ' glassy ' diamond.

All of these have somewhat greater slope than the average of the deep pits on the stone, and the variance among them is only about half as great as that for all of the deep pits.

It will be noticed that the larger variation in depth is mainly due to the different reference surfaces with respect to which measurement is made. This likewise affects the lateral dimensions of the pits. Variation in lateral dimensions is to be expected on this account, and also because of variation of conditions over the surface of the stone. Thus, non-uniformity of lateral dimensions does not necessarily indicate non-uniformity of environment during the establishment of the surface topography, but uniformity of lateral dimensions is an indication of uniformity of environment. Consistently with this, the bimodal resolution in slopes is least clear in the histogram for the third stone, on which trigons had a relatively wide variation in lateral dimensions (about 3 : 1), is of intermediate sharpness for the first, with variation of about 1·5 : 1 in the lateral dimensions, and is very sharp for the second, for which the lateral dimensions of trigons was remarkably uniform (about 1·1 : 1 for the deep pits, 2 : 1 for the shallow ones).

No statistical significance attaches to the relative numbers of deep and shallow trigons in this survey, which are influenced by the varying requirements of measuring technique.

To sum up, it appears that at least for these three stones it is meaningful to classify trigons into two groups, deep and shallow, differing in the slope of their pyramidal faces by a factor of 5 to 10, despite considerable variation within groups, and wider variation from stone to stone. Other stones occur, with a relatively wide variation in trigon sizes, for which no such clear resolution into two groups is possible.

References

Omar, M., and Kenawi, M., 1957, *Phil. Mag.*, **2**, 859.
Pratt, P., and Lomer, W. M., 1952, *J. Inst. Metals.*, **80**, 409.
Tolansky, S., 1948, *Multiple Beam Interferometry* (Oxford: Clarendon Press).
Zernike, F., 1946, *Achievements in Optics*, ed. A. Bornvers (New York: Elsevier).

Etch Pits and Trigons on Diamond: II†

By F. C. Frank and K. E. Puttick‡
H. H. Wills Physical Laboratory, University of Bristol

[Received July 1, 1958]

Abstract

Some experiments on artificial etching of diamonds are described. Etching in steam and chlorine at temperatures of around 800°c produces etch pits in ' positive ' orientation (i.e. opposed to that of natural trigons). Wet hydrogen in the same temperature range and above gives inconclusive results. Etching in this medium may be greatly accelerated by the presence of some catalyst.

Diamonds heated in fused kimberlite at about 1450°c develop sharp-edged triangular pits in ' negative ' trigon orientation. The bearing of this observation on the natural history of diamond is briefly discussed.

§ 1. Introduction

In another paper Frank *et al.* (1958) have described surface features on diamond which strongly suggest that the shallow triangular pits traditionally called ' trigons ' can be formed by etching. It is natural to ask whether pits can be artificially etched which resemble those produced naturally; Omar and Kenawi (1957) have shown that pits developed by heating diamonds in low pressure air reproduce all the characteristics of trigons except that they are oppositely oriented. This note describes some experiments on diamond etching, one of which resulted in triangular pits in the same orientation as trigons.

§ 2. Etching in Gases

Frank *et al.* suggested that a non-oxidizing atmosphere of monovalent radicals such as the water-gas reaction might be responsible for natural etching. As a first attempt to imitate the process, therefore, a small octahedral diamond (whose natural surface features had been recorded by photography and replicating in Perspex) was heated in a quartz tube through which steam was continuously passed, to a temperature of 750°c for one hour. This resulted in a surface covered with flat-bottomed triangular pits, mainly with slightly rounded corners, about 2 μ in size and in ' positive ' orientation, i.e. parallel to the edges of the octahedral face and opposite to the trigon orientation. It was thought possible that some oxygen had been dissolved in the water from which the steam was generated, and a deoxidizer was added before a second heating to 820°c, again for one hour. This treatment etched the diamond more deeply,

† Communicated by the Authors.
‡ Now at the Department of Metallurgy, University of Cambridge.

but again with positively oriented pits, and also delineated many ring cracks and similar evidences of mechanical damage.

Other possible sources of monovalent ions are hydrogen or the halogens. An attempt was made to re-etch the diamond on which the first experiment had been made, with wet hydrogen at 820°c for an hour. This did not alter the appearance of etch pits previously formed, but it was noticeable that some very deep cavities were scored in the surface. A further attempt was made at 900°c, but the furnace burnt out after a few minutes. After all this treatment the stone appeared opaque and dark grey, suggesting the presence of a surface layer of graphite.

Another diamond was etched in wet hydrogen at 850°c for fifteen minutes (again terminated by the burning-out of the furnace). Most of the stones used in these experiments were cleaned in organic solvents and nitric acid before heating; this one, however, was only washed in xylol. Comparatively few pits were formed, most of which were so rounded that no crystallographic orientation was apparent. Through a low power stereoscopic microscope another phenomenon could be seen; a number of winding tunnels penetrating deeply into the interior of the stone (fig. 1, Pl. 84). This remarkably localized attack, originating mainly at points on the edge of the crystal, suggests some kind of catalytic action. It is known that the formation of methane by the direct union of carbon and hydrogen is catalyzed by hydrated iron oxide, particles of which may have been transferred from the steel tweezers used for manipulating the specimen.

Further attempts to etch a diamond in wet hydrogen at 1100°c and 1300°c again resulted in the development on the surface of rounded pits bearing no obvious relation to the crystal symmetry.

There remained the possibility that one of the halogens might be a suitable etching reagent for diamond. As a supply of pure liquid chlorine was available, this element was tried first. A tube of combustion glass containing a diamond was evacuated to backing pump pressure (about 10^{-3} mm of mercury) filled with chlorine to about half atmospheric pressure, and sealed. The tube was then heated for 17 hours at 800°c in a muffle furnace.

After this treatment the surface of the stone showed sharp-edged triangular pits which in many ways resemble natural trigons (fig. 2 (*a*), Pl. 85). Both flat-bottomed and pyramidal pits can be seen; but they are smaller than most trigons, ranging from the limit of resolution of the optical microscope up to 1–2 μ. As in other experiments, they are in positive orientation with respect to the crystal face. The etching also revealed a number of curious features which seem to have no crystallographic habit; the roughly rectangular markings in fig. 2 (*b*) and (*c*), Pl. 85. It is worth noticing a similar feature seen on the surface of the unetched blue white diamond examined by Frank *et al.*, an electron micrograph of which is shown (fig. 3, Pl. 86). It seems to be a series of small islands surrounded by a 'moat'. The replica surface has been

tilted to increase contrast in the photograph, so that the true angular relationships are distorted, but it also has no obvious relation to the symmetry. Such markings may represent etching of small inclusions in the diamond surface.

The foregoing experiments on etching of diamonds in gases are therefore generally inconclusive. The production of pits in positive orientation in water vapour and chlorine might in each case be ascribed to the undoubted presence of a trace of oxygen, while etching in a reducing atmosphere of wet hydrogen seems to have no well defined habit. It was therefore decided to try to dissolve a diamond in conditions resembling its natural environment.

§ 3. Etching in Blue Ground

It was observed by Luzi (1892) that a diamond dissolves at a temperature of 1770°† in fused kimberlite or blue ground, the altered igneous rock in which diamonds are found. After heating for half an hour, very deep corrosion figures of an oval or half-round shape were found, but as the diamonds were blackened, no doubt by graphite, it seems uncertain how far the effect was the result of graphitization followed by attack of the graphite. Luzi also noticed that his specimens were frequently covered with a red coating, which is stated to have been an oxide of iron.

We have carried out some experiments with this material, a sample of which from the Bultfontein mine was kindly given to us by Mr. White of the Geology Department, University of Bristol. The specimen was a small octahedron, with faces about 1 mm^2; careful microscopic examination revealed only one or two small, shallow trigons on each face. This stone was surrounded by pulverized blue ground in an alumina crucible, which was heated in graphite container by induction. A transparent quartz jacket enclosed the graphite, over which a slow stream of nitrogen was passed to minimize burning, and also any oxidation of the kimberlite.

The graphite was heated to 1450°C in about five minutes. The temperature was measured by sighting an optical pyrometer on to the inside surface of the container; the temperature of the specimen itself may have been considerably higher than this figure, which should be regarded as a lower limit. The point at which melting of the blue ground began was also difficult to determine, because it started at the bottom of the crucible, but it appeared to be about 1200°C. Melting was accompanied by considerable effervescence, probably as a result of the evolution of water vapour from the hydrated components of the rock. In the first experiment this effervescence caused the formation of a frothy cap of material over the top of the open crucible. Heating was continued for about ten minutes, and the sample was then cooled fairly rapidly by switching off the heater.

† The temperature scale does not seem to have been specified by Luzi, but Gardner F. Williams (The Diamond Mines of S. Africa) states that it was Reamur. It seems remarkable, however, that any diamond should survive for half an hour at 2200°C.

The porous material formed by the solidified froth was chipped away, and the diamond (which seemed to have been encased in a bubble of the melt) was recovered. It was blackened by a surface layer of graphite, and one side—presumably that actually in contact with the fused mineral throughout the heating, was considerably corroded with no recognizably crystallographic etching. This face had also a reddish tinge. The other faces exhibited a considerable number of sharp-edge triangular pits in 'negative' orientation, some of them several microns deep (fig. 3).

Since the diamond had been graphitized to an unknown depth, the possibility that the markings had been etched in the graphite could not be excluded. A second crystal, similar in size and quality to the first was heated in blue ground. The temperature rise was even more rapid than in the first experiment: 1450°c was attained in about two minutes, and the fused mineral did not form a cap obscuring the interior of the crucible. The heating was continued for seven minutes, at the end of which time it was noticed that the diamond had floated up to the surface melt. The heater was then switched off and the crucible cooled as rapidly as possible by increasing the flow of nitrogen.

This stone was found to be deeply etched, but with no graphite coating. (It is possible that surface graphitization had occurred and that the graphite was burnt away by a trace of oxygen in the nitrogen atmosphere after reaching the top of the melt.) The microstructure of the diamond near an apex of the octahedral face is shown in fig. 4, Pl. 86. The surface (previously almost featureless) is covered with shallow pits in the 'negative' orientation, characteristic of the natural trigons on diamond, fairly uniform in size and outlined by what seem to be grooves, giving a curious 'wormeaten' appearance to the crystal. There are also a number of pits which are extremely deep; the particular cluster in fig. 5, Pl. 87 are about 15 μ in depth, and others of 20 μ and more have been seen. Figure 5 is a photograph taken with the microscope focused on the bottom of another group. The shape of the pits seems to be roughly that of a steep-sided inverted pyramid, with a curious bump (indicated by a bright spot in the centre of the triangle) at the apex. It will be noticed that in spite of the very rapid rate of etching at these pits the corners are quite sharp, indicating that the 'negative' etch habit is very strongly marked.

The face which had been resting on the surface of the molten kimberlite, and had thus been in contact with it during the entire period of heating was, as before, so heavily attacked that any crystallographic etching had been obscured. This face, like the corresponding face in the previous experiment, was a reddish colour.

§ 4. Etch and Dissolution Habit of Kimberlite

Since pits can be etched in negative orientation, and Frank *et al.* have shown that features characteristic of dissolution are associated with trigons, it seems reasonable to assume that trigons are etch figures. It follows that the various curved shapes of diamond are also the result of

dissolution of the octahedral form, since any reaction which etches the negative ⟨110⟩ steps forming trigons will also develop the same type of step at the edge of the (111) face, as shown in fig. 6. The edges are thus rounded off and the octahedral face is gradually replaced by a number of curved surfaces. Fersmann and Goldschmidt (1911) showed how this dissolution habit leads to the so-called dodecahedral and hexakisoctahedral forms of crystal.

Since all the observed surface features and morphology of diamond can be accounted for by dissolution processes, it is of interest to know at what stage in the history of the crystal these could have occurred.

Fig. 6

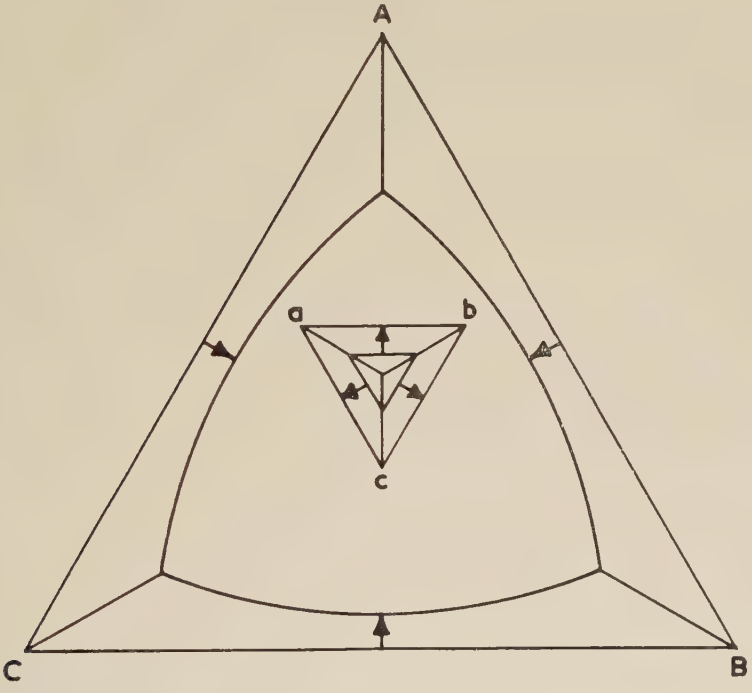

Formation of trigon (*a b c*) and dissolution of octahedral face from edges (*A B C*).

§ 5. Blue Ground and the Natural History of Diamond

Blue ground, or kimberlite, is found in South Africa in pipes and dykes formed by eruptions which probably occurred towards the end of the Cretaceous period; the upper layers have since been extensively eroded, possibly by some thousands of feet. The existing surface layers have been weathered to 'yellow ground'. Kimberlite is a complex mineral whose composition varies with the time and place of eruption, but in all cases it clearly derives from material having a high proportion of olivine.

$(Mg, Fe)_2SiO_4$. This has been largely altered by hydration to serpentine, $H_4Mg_3Si_2O_9$.

The rock has a porphyritic structure: that is, it consists of a fine grained matrix, in this case of mica and olivine, in which are embedded much larger crystals. In kimberlite these may be of, for example, olivine, phlogopite (Magnesia–mica), enstatite and diopside (pyroxenes), garnet, and occasionally diamond. Since any of these frequently occurs as inclusions in most of the others, it appears that they were all formed under the same conditions of great pressure and temperature at depths of several hundred kilometres, and were transported by the rise and eruption of fluid magma to their present position. After the eruption the liquid phase rapidly solidified to form the matrix of small crystals.

Two facts are relevant to the present inquiry. First, it was remarked by Williams (1932) that diamond inclusions in diamond are often rounded octahedra. Obviously a fluctuation in carbon saturation in the neighbourhood of a growing crystal caused partial resorption, after which conditions for further crystallization were restored.

A second observation worth noting is that most of the large transported crystals show clear signs of partial dissolution, arguing some universal change in conditions in the parent magma. This is generally assumed to have been a gradual fall in pressure during the rise of magma: it seems reasonable, therefore, to suppose that it was responsible also for the natural etching of diamond. It has been shown that at atmospheric pressure diamonds both dissolve and graphitize fairly rapidly in molten kimberlite, and that in an environment free of oxygen graphite forms at a temperature below 900°c in a few hours. Since stones are commonly found free of graphite (and from the traces which the formation of graphite leaves on a surface) and relatively lightly etched, the inference is that immediately after the eruption the kimberlite pipes were cooled by at least 400–500°c, and possibly much more, in a period of the order of minutes. This was no doubt the combined result of the release of pressure and of the consequent boiling off of water vapour and carbon dioxide. This cooling must in fact be an essential condition for the preservation of large diamonds; since the rate of cooling was presumably greatest at the surface, the upper layers may have been much richer in diamonds than the existing pipes. These upper layers were no doubt the source of alluvial diamonds. It is significant that the yield of all mines decreases with depth.

The particular reaction responsible for etching trigons cannot yet be certainly identified. However, the available evidence indicates that dissolution took place in the fluid magma, and in such an environment carbon must readily reduce the Fe_2O_3 present. It seems likely, therefore, that this reduction is the principal agent of natural dissolution of diamond. The reddish substance deposited or adsorbed on the surface of diamonds artificially etched in kimberlite, also suggesting that this oxide is involved, lends some support to this hypothesis.

Acknowledgments

We wish to thank Industrial Distributors Limited for giving us the diamonds for the investigation, Dr. G. W. T. White and Mr. J. H. Burrow for advice on the use of the induction heater, and Mr. M. B. Ives for help with some of the experiments. One of us (K. E. Puttick) was Royal Society Armourers and Brasiers Research Fellow in Metallurgy when the work was done.

References

von Fersmann, A., and Goldschmidt, V., 1911, *Der Diamant.*
Frank, F. C., Puttick, K. E., and Wilks, Eileen M., 1958, *Phil. Mag.*, **3**, 1262.
Luzi, W., 1892, *Ber. dtsch. chem. Ges.*, **25**, 2470.
Omar, M., and Kenawi, M., 1957, *Phil. Mag.*, **2**, 859.
Williams, A. F., 1932, *The Genesis of the Diamond* (London: Ernest Benn).

The Scattering of Long Wavelength Neutrons by Irradiated and Unirradiated Quartz†

By E. W. J. Mitchell and P. T. Wedepohl‡
Physics Research Laboratories, University of Reading

[Received June 23, 1958]

Abstract

Measurements have been made of the transmission of neutrons of wavelengths between 5 and 10 Å through 10 cm of unirradiated and pile irradiated Brazilian quartz crystals. The total transmission cross section of the unirradiated crystal varied as $\sigma_A = 0{\cdot}55 + 1{\cdot}63\lambda$ in the measured wavelength range. After irradiation with $6{\cdot}4 \times 10^{18}$ fast $n^\circ\,\mathrm{cm}^{-2}$, as indicated by the [S(n°p)P] reaction, additional scattering was found. This amounted to 0·18 barns per molecule between 12 and about 9 Å rising continuously below 9 Å. The measurements are discussed in relation to optical absorption measurements and radiation damage theory.

§ 1. Introduction

Antal *et al.* (1955) have shown how the concentration of defects in pile irradiated graphite can be determined from the induced long wavelength neutron scattering. The concentration is calculated in terms of experimentally determined parameters but a relatively large irradiation dose (*ca.* 10^{19} fast $n^\circ\,\mathrm{cm}^{-2}$) is required to observe the effect.

Because of the possibilities of collision induced recombination occurring during such heavy irradiations, for example, a displaced atom filling a neighbouring vacancy, direct comparison of the experimentally determined concentration with low dose damage theory is probably not valid. The object of the present experiment was to use the method to calibrate some other property—optical absorption in quartz—which could then be compared with radiation damage theory at lower doses.

In addition an attempt has been made to measure the wavelength dependence of the induced scattering. This is important because it was assumed by Antal *et al.* (1955) that the scattering is by isolated point defects. For wavelengths of the order of ångströms we should expect the scattering by isolated nuclei of dimensions of the order 10^{-4} Å to be independent of wavelength.

§ 2. Experimental

The experiment became possible in this country following the development by Dr. P. Egelstaff and his colleagues (1957) of a small volume of

† Communicated by Professor R. W. Ditchburn.
‡ Present address : Diamond Research Laboratory, South Africa.

liquid hydrogen moderator in the Harwell pile BEPO. These authors have already described the details of the neutron source, liquid air cooled beryllium filter, chopper and counting equipment.

In our experiment the neutron transmission has been measured of two crystals (A and B) of Brazilian quartz having dimensions $2 \times 2 \times 10$ cm. The crystals were supplied by Hilger and Watts Ltd. and were described as being of the highest optical quality. The uniformity of the visible absorption induced by irradiation is known to be an indication of quality, although the band is associated with aluminium impurity. In crystal B the visible absorption after irradiation was completely uniform throughout the crystal.

The neutron beam was defined by two cadmium sheet stops the apertures of which were just less than the specimen dimensions. A specimen holder was built which allowed each of the crystals to be moved reproducibly into the beam and which provided one straight through position. Measurements of the transmitted intensities I_A and I_B and of the incident intensity I_0 were made, counts being taken usually for 10 minutes at a time and repeated in a sequence ($I_A\ I_0\ I_B\ I_A\ I_0\ I_B \ldots$).

§ 3. Results

Both crystals were measured in the unirradiated condition. At this stage although some counts were made for $\lambda > 10$ Å the greatest numbers of counts were obtained betwen 4 and 10 Å. Approximately 10^4 counts were made on the beam transmitted by each specimen at each of six wavelengths between 4·4 and 6·0 Å, and 2×10^3 at six wavelengths between 6·2 and 10 Å. The measured transmissions decreased with increasing wavelength from 73% to 55%, the measurements on the two crystals agreeing within $\pm 1\%$ and frequently within $\pm \frac{1}{2}\%$. These results indicated that the crystals could be assumed to be identical for our purpose.

Crystal B was then irradiated in a hollow uranium slug in BEPO. This facility was kindly provided by the Metallurgy Division and the dose was estimated from the $^{32}_{16}\mathrm{S}$ (fast n°, p)$^{32}_{15}\mathrm{P}$ reaction. The threshold for this reaction is about 2 MeV and the dose received by the quartz was $6{\cdot}4 \times 10^{18}$ $n^\circ\,\mathrm{cm}^{-2}$ of energy between 2 and 4 MeV. The temperature during the irradiation was approximately 40°C.

Subsequently the transmissions of both A and B were redetermined. At this stage many more counts were made, varying from 10^5 for each crystal at wavelengths near 8 Å to $1{\cdot}8 \times 10^4$ near 11 Å. For the whole wavelength range we take the measurements on crystal A to be those for the unirradiated state and compare with those for B after irradiation. The transmission of the irradiated crystal was between 5% less, near 6 Å, and 2% less near 11 Å, than the unirradiated crystal.

No attempt was made to record accurately the change in length of crystal B with irradiation, but any such change must have been less than

0·5%. In any case we have used the length x_B cm measured after irradiation. Then we have:

$$I_A = I_0 \exp(-\sigma_A x_A N),$$
$$I_B = I_0 \exp(-\sigma_B x_B N') = I_0 \exp(-\sigma_B' x_B N)$$

where N and N' are the numbers of SiO_2 molecules per cm^3 before and after irradiation, and the σ's are total cross sections of all processes leading to removal of neutrons from the beam.

The densities of the two crystals were measured by weighing in air and water and the change was found to be:

$$\Delta\rho/\rho = -(0{\cdot}784 \pm 0{\cdot}002)\%.$$

A similar value of $-(0{\cdot}81 \pm 0{\cdot}10)\%$ was found by flotation in tetrabromoethane/ether for a 0·2 mm disc which was irradiated at the same time and in the same can as the large crystal.

The results for σ_A are shown in fig. 1 (*a*) for wavelengths between 5 and 12 Å. Some measurements were made below 4 Å using a crystal spectrometer and the transmission decreased rapidly with decreasing wavelength, corresponding to the occurrence of increasing numbers of Bragg reflections.

In fig. 1 (*b*) the quantity $(\sigma_B' - \sigma_A)$ is plotted as a function of wavelength. For all measurements the resolution of the chopper was such that the wavelength spread in the beam at each wavelength was about 0·8 Å.

§ 4. Discussion of Results

4.1. *Unirradiated Quartz*

If the specimen had been polycrystalline the limiting wavelength (2d) for Bragg reflections would have been 8·5 Å. However, the orientation of the crystal was such that an a-axis (e.g. the normal to (120)) was 6° from a line parallel to the beam. The orientation was determined from a back reflection Laue photograph. In this orientation we expect Bragg scattering to occur at 7·76 and 6·88 Å corresponding to (110) and (100) type reflections. These were not observed. Bragg reflection might be expected to be spread in a good quartz crystal over a wavelength range of about 0·01 Å, but the wavelength spread of the beam was 0·8 Å so that it is not surprising that other peaks were not resolved. Measurements at lower wavelengths using the spectrometer showed a strong peak near 3·5 Å, corresponding to a (200) reflection.

From fig. 1 (*a*) it will be seen that σ_A increases linearly with wavelength, but the extrapolation to zero does not go through the origin. Between 5 and 12 Å we find

$$\sigma_A \text{ (barns per molecule)} = 0{\cdot}55 + 0{\cdot}163\lambda.$$

This cross section will include contributions from absorption (Si), inelastic scattering by lattice vibrations, and scattering by impurity or other defects. Isotope and spin scattering are negligible for SiO_2.

According to Bacon (1955) the absorption cross section of Si is 0·06 b. per atom at 1·08 Å and since absorption is directly proportional to λ we have a contribution to σ_A of 0·056λ, b. per SiO_2 molecule. The theory of

inelastic scattering has not been worked out exactly for quartz. However, Cassels (1950) calculated for a body-centred cubic crystal whose Debye temperature (θ) was 453°K and whose atoms were of mass (M) 56, that $E(S)/S$ increased linearly with wavelength above about 5 Å. $E(S)$ is the inelastic scattering cross section and S the coherent scattering cross section. He found that $E(S)/S$ at a given wavelength was approximately proportional to $1/M\theta$. Using these results reasonable agreement is obtained with

Fig. 1

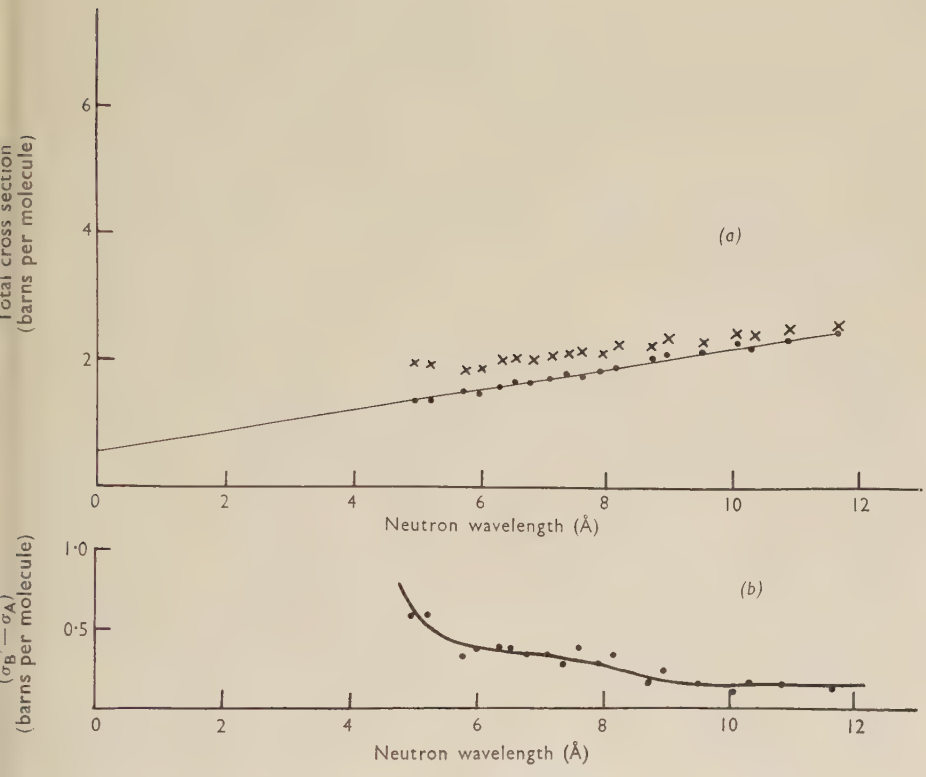

(*a*) The variation of the transmission cross section of quartz with neutron wavelength : . . . . . before irradiation ; × × × × × after irradiation. (*b*) The variation of the radiation induced scattering cross section with wavelength.

the measurements on aluminium (Cassells 1951), magnesium (Squires 1952) and carbon (Kothari and Singwi 1957). For quartz we have $S_{Si} = 2{\cdot}0$ b. per atom, $S_0 = 4{\cdot}2$ b. per atom (Bacon 1955) and $\theta = 760$°K. Then regarding the crystal as being composed of atoms of mass 20 units and $S = 3{\cdot}5$ b. we find, using Cassel's result, that in the region beyond about 5 Å $E(S) = 0{\cdot}11\lambda$, b. per molecule.

These two contributions, therefore, would be expected to give a cross section for $\lambda > ca.$ 5 Å of $\sigma \propto 0{\cdot}166\lambda$, b. per molecule, which is in fortuitously good agreement with the experimental value of $0{\cdot}163\lambda$.

We have now to consider whether the wavelength independent part of the total cross section can be ascribed to impurities or other defects. Absorption is wavelength dependent and need not be considered. Hydrogen seems to be the only likely impurity having a sufficiently high scattering cross section, 81 b. per atom, to give the required contribution. Approximately 0·2 atm% of H would have to be present. This is a higher concentration than one would have thought probable, but there is little quantitative data available and the number is feasible.

4.2. *Irradiated Quartz*

The additional scattering induced by the irradiation may be represented by an effective cross section per molecule (σ_d) given by:

$$\sigma_d = \sigma_B - \sigma_A = \frac{1}{N(1-\Delta N/N)x_B}\ln\left(\frac{I_0}{I_B}\right) - \frac{1}{Nx_A}\ln\left(\frac{I_0}{I_A}\right) \quad . \quad (1a)$$

or if $\Delta N/N \ll 1$ by:

$$\sigma_d = \sigma_B{}' - \sigma_A = \frac{1}{N}\left\{\frac{1}{x_B}\ln\left(\frac{I_0}{I_B}\right) - \frac{1}{x_A}\ln\left(\frac{I_0}{I_A}\right)\right\}. \quad . \quad . \quad (1b)$$

It will be seen from fig. 1 (*b*) that, for wavelengths greater than 9 Å, $(\sigma_B{}' - \sigma_A)$ is constant within the experimental spread and is equal to $0{\cdot}16 \pm 0{\cdot}03$ b. per molecule. As shown by the density measurements $\Delta N/N = 0{\cdot}8\%$ and the true σ_d—given by eqn. (1*a*)—should be greater than $(\sigma_B{}' - \sigma_A)$ by 0·02 for wavelengths between 9 and 12 Å. Thus we have σ_d in this region equal to $0{\cdot}18 \pm 0{\cdot}03$ b. per molecule.

For wavelengths less than 9 Å the induced scattering cross section increases with decreasing wavelength. This indicates that the scattering in the damaged crystal cannot be ascribed only to isolated point defects. Four factors may contribute to the wavelength dependence:

(i) Scattering by atoms in the amorphous regions which may be produced near the ends of tracks of knocked on atoms (Mitchell and Paige 1956).

(ii) Scattering by the atoms surrounding point defects, which atoms will not be expected to be in their normal lattice positions.

(iii) Scattering by aggregates of point defects. The constituents of such aggregates would have to be separated by about 5 Å or less.

(iv) A change in the inelastic scattering cross section arising from a radiation induced change in the vibrational spectrum of the crystal.

The last factor could be eliminated by measuring the transmissions at temperatures low enough for inelastic scattering to be negligible. It is hoped that this may be done in a future experiment. For the present we note that a change of 30° in the Debye temperature would not introduce a serious error and that changes of this magnitude have not been reported. Following Antal *et al.* (1955) it is assumed, therefore, that any change in the inelastic scattering may be neglected.

The net effect of (i) and (ii) is that a number of atoms, while remaining part of the SiO_4 network†, are displaced from their normal positions. It is likely that the increased scattering from these factors will be in the normally diffracting region, less than 9 Å.

Finally we should expect that aggregates, such as close pairs of like interstitial atoms having separations of about 5 Å, would scatter less at wavelengths beyond 9 Å than would two isolated interstitial atoms. If the effect is important the defect concentration calculated below would be an underestimate of the number of displaced atoms.

With this qualification we interpret σ_d for wavelengths greater than 9 Å as arising from scattering by point defects alone. Assuming that the displaced atoms are in the ratio of 2 oxygen to 1 silicon then:

$$\sigma_d \text{ (b. per molecule)} = 2g(\sigma_{Si} + 2\sigma_O), \quad . \quad . \quad . \quad . \quad (2)$$

where g is the fraction of atoms displaced, and σ_{Si} and σ_O are the scattering cross sections for silicon and oxygen nuclei. The essential feature of the method of Antal *et al.* (1955) is that the atomic scattering cross sections are known from other nuclear scattering experiments. Bacon (1955) gives $\sigma_{Si} = 2{\cdot}0$ and $\sigma_O = 4{\cdot}2$ b. per atom. Thus for $\sigma_d = 0{\cdot}18 \pm 0{\cdot}03$ b. per molecule we find $g = (0{\cdot}86 \pm 0{\cdot}10)\%$.

Using the result found by Kinchin and Pease (1955) that a primary knock on of energy E produces $E/2E_d$ displacements we find that $6{\cdot}4 \times 10^{18}\, n^\circ\, cm^{-2}$ having energies between 2 and 4 Mev would produce a total fraction of displaced atoms of *ca.* 10%. At such a concentration replacement collisions have to be considered so that a direct comparison with the experimental value is not possible.

We make the comparison with low dose theory as follows. There is an absorption band in the ultra-violet (C-band, 5·7 ev) induced by pile irradiation. For low doses the absorption increases approximately linearly as $\mu_{max}(cm)^{-1} = D \times 10^{-17}$, where D is the equivalent thermal dose for the irradiation conditions described by Mitchell and Paige (1956). Crawford (private communication) have shown that for doses corresponding to $\mu_{max} > 100\ cm^{-1}$ the rate curve departs increasingly rapidly from the linear rate and eventually goes through a flat maximum. This could also be associated with the occurrence of replacement collisions.

The absorption in the thin specimen, which was irradiated in the same can as the larger crystal, was 194 cm^{-1} at the C-band peak and had an estimated width at $\frac{1}{2}$-absorption of 1·3 ev. The width agrees as well as can be expected with the value of 1·4 ev found at lower doses. Assuming that the fraction (x), of defects in the state of ionization which gives the 5·7 ev absorption, is the same for the two conditions of irradiation and that the f-value is independent of the concentration of centres, we have:

$$\mu_{HD}/1 = g_{HD}/g_{LD} \quad . \quad . \quad . \quad . \quad . \quad . \quad . \quad (3)$$

where g_{HD} is the concentration of displaced atoms determined above—the subscript HD referring to 'high dose'—and g_{LD} is the fraction which must

† Point defects are not parts of the network.

be present to produce each 1 cm^{-1} of absorption in the low dose experiments. This required an equivalent thermal dose of $10^{17}\,n^{\circ}$ cm^{-2}. Thus g_{LD} is $4{\cdot}4\times10^{-3}\%$ per $D=10^{17}\,n^{\circ}\,cm^{-2}$.

According to the calculations of Mitchell and Paige (1956), g_{LD} per 10^{17} equivalent thermal dose is between $30\times10^{17}/N$ and $45\times10^{17}/N$ where N, the total number of Si and O atoms per cm^3, is $7{\cdot}86\times10^{22}$. By calculation, therefore, we find that $3{\cdot}8\times10^{-3}\% < g_{LD} < 5{\cdot}7\times10^{-3}\%$.

Finally, the measurements of the heavily irradiated crystals lead to a value of (xf) equal to $3{\cdot}7\times10^{-3}$ for the C-band absorption, where f is the oscillator strength for the transition.

§ 5. Conclusions

The main conclusions of this work are:

(i) The transmission of long wavelength neutrons through crystalline quartz can be reasonably accounted for by inelastic scattering and Si absorption.

(ii) The scattering between 5 and 12 A induced by pile irradiation cannot be explained in terms of isolated point defects alone.

(iii) The scattering for $\lambda > 9$ Å taken in conjunction with optical absorption data leads to a reasonable numerical agreement with radiation damage theory. Because of the various uncertainties, however, the agreement is not as good as the numbers indicate—there possibly being an uncertainty of a factor of about 5.

Acknowledgments

We should like to thank Dr. P. Eglestaff, A.E.R.E., Harwell, for making it possible for us to do this experiment. We are also grateful to him and to various members of his group for their advice—particularly to Mr. G. McCallum and Dr. F. J. Webb.

For his interest and help in obtaining the crystals we wish to thank Professor R. W. Ditchburn, and P. T. W. is grateful to Dr. J. F. H. Custers, Director of the Diamond Research Laboratory, Johannesburg, for permission to work at A.E.R.E. during the Summer of 1957.

Finally, we should like to thank Mr. J. D. Rigden for assistance with the density and optical measurements, and Dr. R. J. Elliott for helpful discussions.

References

Antal, J. J., Dienes, G. J., and Weiss, R. J., 1955, *Phys. Rev.*, **99,** 1081.

Bacon, G. E., 1955, *Neutron Diffraction* (Oxford: University Press).

Butterworth, I., Egelstaff, P. A., London, H., and Webb., F. J., 1957, *Phil. Mag.*, **2,** 917.

Cassels, J. M., 1950, *Progress in Nuclear Physics*: I, ed. O. R. Frisch (London: Butterworth; Berlin: Springer); 1951, *Proc. roy. Soc.* A, **208,** 527.

Kinchin, G. H., and Pease, R. S., 1955, *Rep. Prog. Phys.*, **18,** 1.

Kothari, L. S., and Singwi, K. S., 1957, *Phys. Rev.*, **106,** 230.

Mitchell, E. W. J., and Paige, E. G. S., 1956, *Phil. Mag.*, **1,** 1085.

Squires, G. L., 1952, *Proc. roy. Soc.* A, **212,** 194.

Activation Energies for High Temperature Creep of Polycrystalline Zinc†

By W. J. M. Tegart
Department of Metallurgy, The University, Sheffield
and Oleg D. Sherby
Department of Metallurgical Engineering, Stanford University, California;
formerly Department of Metallurgy, The University, Sheffield

[Received July 1, 1958]

Abstract

The creep of polycrystalline zinc above 0·5 T_m (T_m= absolute melting temperature) appears to be controlled by two thermally activated processes acting additively. One process, predominating between 0·5 and 0·6 T_m, is believed to be associated with dislocation climb since the experimentally determined activation energy for creep is about equal to the energy for self-diffusion, namely, about 21·0 kcal per mole. The other process, predominating between 0·8 and 1·0 T_m, is believed to be associated with prismatic slip since the activation energies for these two processes are both equal to about 38·0 kcal per mole.

§ 1. Introduction

Extensive experiments on the high temperature creep of polycrystalline pure metals reveal that the experimental activation energy for creep, Q_c, is about equal to the respective activation energy for volume self-diffusion, Q_d (Sherby *et al.* 1954, Frenkel *et al.* 1955, Weertman and Shahinian 1956, Sherby and Lytton 1956, and Sherby 1958). This equality appears to be well established for twelve pure metals, namely, the face-centred cubic metals, Al, Ni, γ-Fe, Au, Cu, and Pb; the body-centred cubic metals, α-Fe and β-Tl; the hexagonal close packed metals, Mg, α-Tl, and Cd; and face-centred tetragonal indium. A recent publication on self-diffusion in platinum suggests that $Q_c \simeq Q_d$ for this metal also ($Q_c = 56$ kcal per mole (Sherby *et al.* 1954) and $Q_d = 67$ kcal per mole (Kidson and Ross 1957)). These correlations suggest that creep of most polycrystalline metals is controlled by dislocation climb. The activation energies for creep of single crystals under single slip conditions do not conform with the activation energies for volume self-diffusion (Gilman 1956, Lytton *et al.* 1958). Such evidence suggests that dislocation climb might not be the important process in these cases.

Although the creep of zinc has been extensively studied, the activation energy for creep does not appear well defined. All known experimental data on activation energies for creep and self-diffusion of zinc are given in

† Communicated by the Authors.

tables 1 and 2. Sherby *et al.* (1954) suggested that Q_c for polycrystalline zinc was about equal to Q_d (about 23 kcal per mole) from analyses of limited data on creep of zinc obtained in the temperature range 40–70°C by Pomp and Länge (1936). However, Cottrell and Aytekin (1950) obtained a value of Q_c for polycrystalline zinc considerably lower than Q_d, in fact about 12 kcal per mole in the temperature range 95–120°C. Further, Gilman (1956) suggested that creep of polycrystalline zinc, at least above 250°C, was controlled by prismatic flow for which Q_c was equal to 38 kcal per mole. In view of the discrepancy in the results for low temperatures and the possibility that Q_c for polycrystalline zinc may be temperature dependent above $0{\cdot}5\ T_m$ in contrast to the other metals so far examined, the present investigation was undertaken to determine Q_c over the temperature range from 70°–400°C.

Table 1. Activation Energies for High Temperature Creep of Zinc

Q_c (kcal/mole)	Reference	Purity (%)	Temp. Range (°C)	Creep Stress (kg/cm²)
A. Polycrystalline zinc				
26·0	Pomp and Länge (1936)	99·0	40–70	450–750
12·0	Cottrell and Aytekin (1950)	Spec. pure	95–120	80–120
38·0 (implied)	Gilman (1956)	99·999	298	15–40
B. Single crystals of zinc				
29·0 (Basal)	Cottrell and Aytekin (1950)	Spec. pure	85–110	2–5
5·0 (Basal)	Gilman (1956)	99·999	180–407	0·8–2
38·0 (Prismatic)	Gilman (1956)	99·999	255–407	40–100

§ 2. Material and Experimental Techniques

The material used was 'Crown Special' zinc (> 99·99 wt% zinc) with traces of silver (0·0001%), cadmium (0·002%), copper (0·0002%), iron (0·003%) and lead (0·0005%), and was received in the form of extruded bar, $\frac{7}{8}$ in. diameter. These bars were warm rolled at approximately 150°C to $\frac{5}{16}$ in. diameter and then machined into solid cylindrical specimens $\frac{1}{4}$ in. in diameter and $\frac{3}{8}$ in. tall. The initial batch was annealed in an argon atmosphere at 395°C for $1\frac{1}{2}$ hours. The resulting average grain size was determined to be about 0·06 in., although some fine grains were still present in the final annealed material. Later, a further batch was

annealed at 403°C for 1 hour in a salt bath (KNO_3 and $NaNO_3$) yielding a smaller average grain diameter of 0·015 in.

Creep tests were performed under compression since suitable equipment was available. This equipment is described in another paper on the creep properties of alpha and beta thallium (Sherby 1958). It was possible to measure creep strains to a sensitivity of 0·00025, and all strains recorded in this investigation are reported as true strain ϵ, where $\epsilon = \ln(1+e)$, e being the engineering strain. The stress was maintained constant by periodically adding lead shot to the direct load weight pan as creep proceeded. It was possible to maintain the stress constant to $\pm\frac{1}{2}\%$ of the predesired stress throughout any one test. Tests were usually terminated by $\epsilon = 0{\cdot}15$ and virtually no barrelling of the specimen was observed to take place up to such strains.

Table 2. Activation Energies and D_o for Self-Diffusion in Zinc

Investigators and reference	Single crystal				Polycrystal	
	$Q\parallel$ kcal/mole	$Q\perp$ kcal/mole	$D_0\parallel$ cm²/sec	$D_0\perp$ cm²/sec	Q kcal/mole	D cm²/sec
Jaumot and Smith† (1956)	22·0	24·9	0·076	0·39	22·7	0·19
Jaumot and Smith‡ (1956)	22·0	23·5	0·068	0·12	23·5	0·11
Shirn *et al.* (1953)	21·8	24·3	0·13	0·58	—	—
Miller and Banks (1942)	20·4	31·0	0·05	0·09	—	—
Liu and Drickamer (1954)	19·6	25·9	0·021	1·60	—	—
Gertsriken and Pryanishnikov (1957)	—	—	—	—	26·4	4·3

† Sectioning technique. ‡ Absorption technique.

Temperatures were maintained constant by using either (*a*) silicone oil baths for the lower temperature creep tests (60°C to 250°C) or (*b*) salt baths, containing equal mixtures of KNO_3 and $NaNO_3$, for tests above 250°C. Specimen temperatures were maintained constant to within $\pm\frac{1}{2}$°C. Cyclic temperature creep test techniques (Tietz and Dorn 1956, Sherby 1958) were used to determine creep rates under a given constant stress and from these data activation energies were calculated. A typical example of such a creep test is shown in fig. 1 where the creep rates as a function of strain for a given stress, under cyclic temperature conditions, are recorded. The observed experimental activation energies, Q_c, were calculated from the relationship

$$\frac{\dot{\epsilon}_1}{\dot{\epsilon}_2} = \frac{\exp(-Q_c/RT_1)}{\exp(-Q_c/RT_2)} \quad . \quad . \quad . \quad . \quad . \quad . \quad . \quad (1)$$

where $\dot{\epsilon}_1$ = creep rate at given creep stress and strain at temperature T_1, in degrees absolute, and $\dot{\epsilon}_2$ = creep rate at same stress and strain at temperature T_2, and R = gas constant = 1·987 calories per mole.

Metallographic observations were carried out on flat surfaces prepared on specimens by mechanical abrasion followed by chemical polishing in Vinaver's solution (Vinaver and Druelle 1955) till all the surface deformation was removed.

Fig. 1

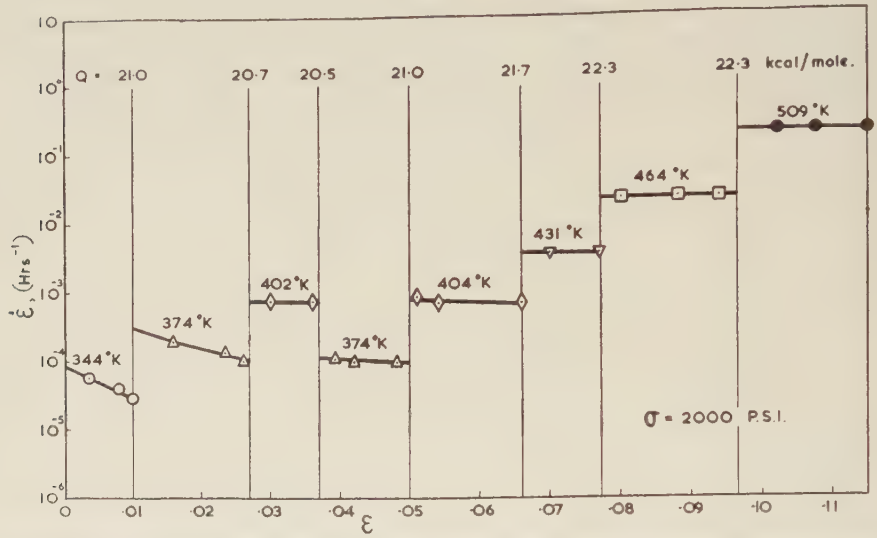

Creep rate ($\dot{\epsilon}$)–true creep strain (ϵ) curves for use in evaluation of the activation energies for creep of pure polycrystalline zinc (99·99%) under constant stress.

§ 3. Results and Discussion

All of the values for the experimental activation energies for creep of polycrystalline zinc determined in this investigation are recorded in fig. 2. The temperature range covered was from about 350°K up to about 680°K. No clear cut variation of the activation energy for creep was noted with the creep strain, cf. the typical example in fig. 1, and furthermore there appeared to be no systematic variation of Q_c with the creep stress (fig. 2). However, fig. 2 reveals a very definite dependence of Q_c on temperature. The results suggest the presence of at least two processes with differing activation energies. A process with a low activation energy appears to be operating below $0{\cdot}6\,T_m$ while a process with a high activation energy operates above $0{\cdot}8\,T_m$. These results are thus quite different from those obtained for other pure polycrystalline metals where only one thermally activated process appears to operate above about one-half of the absolute melting temperature (Sherby *et al.* 1954).

Considering first the low temperature results, it is seen that Q_c for Zn is about 21 kcal per mole which is approximately the value reported for self-diffusion (table 2). This equality between Q_c and Q_d suggests that

creep of polycrystalline Zn in this temperature range may be controlled by some type of dislocation climb process. Previous workers (Cottrell and Aytekin 1950, Cahn *et al.* 1953–54, Ramsey 1951–52) have examined polycrystalline zinc specimens after slow straining in this temperature range and have observed basal slip and subgrain formation, the subgrain boundaries being at right angles to the slip plane. Similar structures were observed in the present investigation. These observations suggest that the rate controlling process in this temperature range is the climb of edge dislocations away from pile-ups in the basal plane to form subgrain boundaries. The mechanism of such a climb process in h.c.p. metals has not yet been established. One of the difficulties associated with the development of a mechanism is the nature of the barriers in the basal plane. If only basal slip is operative, the blocking of edge dislocations by sessile dislocations is impossible. However, in polycrystalline aggregates of h.c.p. metals, the deformation is inhomogeneous and it seems likely that the barriers here are sessiles formed by interaction of basal and non-basal slip.

Fig. 2

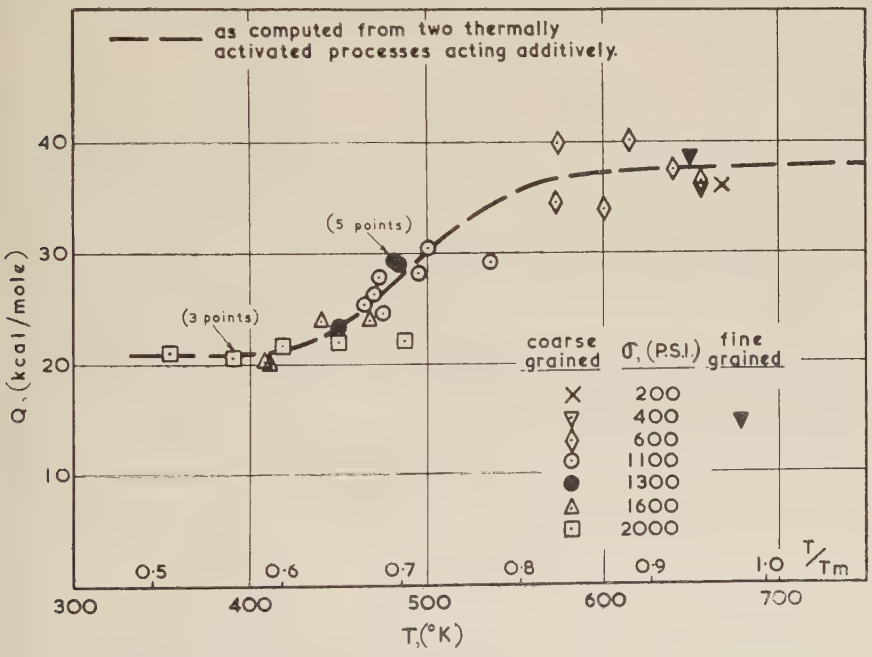

Effect of temperature on the observed experimental activation energy for creep of polycrystalline zinc.

Cottrell and Aytekin (1950) have also determined activation energies for creep of pure zinc polycrystals and single crystals in the low temperature range, but their results (table I) do not agree with the values obtained in this investigation. This discrepancy is not clearly understood, but a

possible explanation is that Cottrell and Aytekin only determined their activation energies over a small range of temperature, 25°c, and a small error in determination of creep rates would have resulted in a large error in the value of Q_c.

Considering now the high temperature process, it is seen that above $0{\cdot}8\,T_m$, Q_c for zinc is about 38·0 kcal per mole. This value is identical to the value obtained by Gilman (1956) for creep of pure single crystals oriented for flow on the prismatic plane. Attempts were made to observe crystallographic slip after creep at 375°c. However, in harmony with the observations of Cahn *et al.* (1953–54), no visible slip could be associated with creep at such temperatures. This observation suggests that very fine slip may be operating at these temperatures. It is also possible that surface diffusion may obliterate the slip lines which would normally be visible. The fact that identical values of Q_c were obtained for creep of polycrystalline zinc and prismatic creep of zinc single crystals, however, constitutes strong indirect proof that prismatic slip controls the creep of zinc polycrystals above $0{\cdot}8\,T_m$.

The data in fig. 2 suggest the presence of two thermally activated processes. These two processes can contribute to creep by acting either additively or sequentially. Each process can be described by an equation of the form:

$$\dot{\epsilon}_i = w_i \exp(-Q_i/RT), \qquad \sigma = \text{const.} \quad . \quad . \quad . \quad . \quad . \quad (2)$$

where $\dot{\epsilon}_i$ = creep rate for ith process, W_i = the weight factor for the ith process, and Q_i = thermal activation energy of ith process. If creep is controlled by two thermal processes acting sequentially then the observed rate of creep is primarily determined by the slowest process. If the thermal activation energies and W's are different, an inversion in the rate controlling process can occur as a function of temperature. An exact analysis of the creep rate under such circumstances is difficult since it requires a knowledge of the dependence of creep rate of each process on the creep stress. However, this approach predicts a decrease in Q_c as the temperature is increased and therefore cannot explain the present results on the creep of zinc.

On the other hand, if two thermal processes act additively, the creep rate, at a given stress, can be described by the equation

$$\dot{\epsilon} = w_1 \exp(-Q_1/RT) + w_2 \exp(-Q_2/RT). \quad . \quad . \quad . \quad . \quad (3)$$

This equation predicts a low value of activation energy at low temperatures and a high value at high temperatures with intermediate values of Q in the intermediate range of temperatures. The results on zinc (fig. 2) agree with such an additive process. If we assume that eqn. (3) can describe the creep of zinc above $0{\cdot}5\,T_m$, a value for the observed activation energy, Q_{obs}, can be calculated, as

$$Q_{obs} = -\frac{R\,d\ln\dot{\epsilon}}{d(1/T)} = \frac{w_1 Q_1 \exp(-Q_1/RT) + w_2 Q_2 \exp(-Q_2/RT)}{w_1 \exp(-Q_1/RT) + w_2 \exp(-Q_2/RT)}. \qquad (4)$$

If one arbitrarily assigns a value of unity for W_1, W_2 can be calculated from a knowledge of Q_{obs} in the intermediate temperature range. Substituting $Q_{obs}=30{\cdot}0$ kcal per mole at $T=500°K$ into eqn. (4), W_2 was found equal to $2{\cdot}5\times10^7$. It is now possible to calculate the variation of the observed activation energy with temperature giving the dotted curve shown in fig. 2. It is interesting to note that eqn. (4), with the above values, predicts a rather broad temperature range (150°c) of intermediate values of Q_{obs} in agreement with the experimental observations and this suggests that the proposed hypothesis might be substantially correct.

The major difficulty of such a model is the large ratio of W_2/W_1 needed to explain the experimental results. Recent work by Weertman (1955, 1957 b) makes it possible to calculate a theoretical value for W_2/W_1. Under conditions where dislocation climb is the controlling process, he has developed an equation for steady state creep which can be expressed as follows (Weertman 1955):

$$\dot{\epsilon}=S\exp(-Q_d/RT)\sigma^{2\cdot9} \quad . \quad . \quad . \quad . \quad . \quad . \quad . \quad (5)$$

where Q_d = activation energy for self-diffusion, σ = creep stress and S is a structure constant to

$$\frac{12L''L'M^{1/3}\bar{\sigma}^{1\cdot1}D_0}{\mu^3kT}$$

where $\bar{\sigma}$ is the critical stress to operate a Frank–Read source, L'' is related to subgrain size, L' = grain size, M = number of Frank–Read sources per unit volume, μ = shear modulus, k = Boltzmann's constant, T = absolute temperature and D_0 = diffusivity constant. Assuming values appropriate to zinc†, we obtain

$$\dot{\epsilon}=2{\cdot}8\times10^6\exp(-Q_d/RT)\sigma^{2\cdot9},\text{hr}^{-1}. \quad . \quad . \quad . \quad . \quad (6)$$

Furthermore, Weertman (1957 a) has also attempted to explain the high activation energy for prismatic creep of zinc single crystals by using Gilman's suggestion (Gilman 1956) that the controlling process might be that of overcoming a large Peierls stress on the prismatic plane. Weertman's equation for creep under such conditions is similar to that for creep controlled by climb and can be approximately described for the case of zinc by

$$\dot{\epsilon}=5{\cdot}7\times10^8\exp(-Q_p/RT)\sigma^{2\cdot9},\text{hr}^{-1} \quad . \quad . \quad . \quad . \quad (7)‡$$

where $Q_p=38\,000$ calories per mole and σ is the creep stress in kg/cm².

Thus with Weertman's models for creep, the ratio W_2/W_1 is equal to about 200, which differs considerably from 10^7 as determined in this work. If the interpretation of the results obtained by means of two thermally activated processes is correct, then it is apparent that the

† $L''=0{\cdot}02$ cm, $M=10^9/\text{cm}^3$, $L'=0{\cdot}1$ cm, $\bar{\sigma}=1$ kg/cm² from Gilman's data on basal creep (Gilman 1956), $\mu=3{\cdot}8\times10^5$ kg/cm² (Gilman 1956), $k=1{\cdot}4\times10^{-22}$ kg cm/°c, $T=400°K$, $D_0=360$ cm²/hr (table 2).

‡ Weertman's theoretical equation is considerably more complex than eqn. (7), but his calculated curve of $\epsilon\exp(Q_p/RT)$ *v* σ can be accurately described by eqn. (7) for creep stresses ranging from 4 to 200 kg/cm².

theoretical analyses will have to be modified before a complete description of high temperature creep in zinc can be given. Furthermore, Weertman's equations predict that the creep rate should vary with (creep stress)^3, but this is clearly not the case for the present work as shown in fig. 3. A recent modification of the original dislocation climb equation by Weertman (1957 a) has yielded a stress exponent equal to 4·5. Calculations of W_2/W_1 from eqn. (7) and Weertman's modified climb equation are now dependent upon the creep stress. At $\sigma = 70\,\mathrm{kg/cm^2}$, $W_2/W_1 = 7 \times 10^3$ which is still considerably below 10^7.

Fig. 3

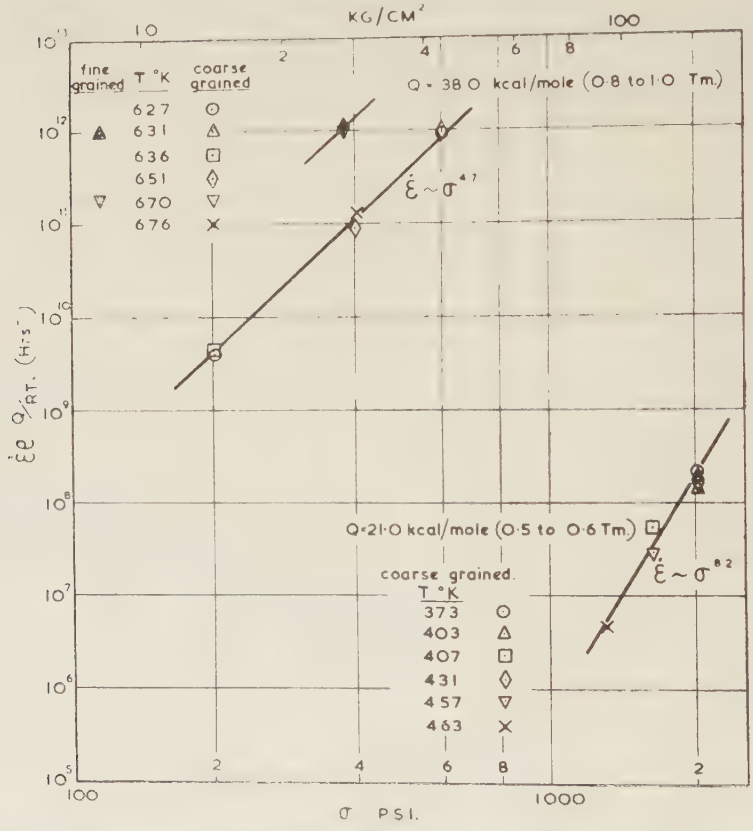

Effect of stress on the steady state creep rate of polycrystalline zinc (99·99%) at high temperatures.

The results of this investigation raise the question of whether other hexagonal close-packed metals have similar changes in their activation energies for creep. One might expect that the creep behaviour of those metals whose slip systems change with temperature would reveal several activation energies. Unfortunately little data are available to check this idea. In magnesium, a change from basal to pyramidal slip occurs at

about 220°c ($0{\cdot}53\,T_m$) (Schmid 1931) but analyses of creep tests in the range 0·4 to $0{\cdot}65\,T_m$ (Sherby and Frenkel 1954) suggest that the activation energy for creep is constant and equal to that for self-diffusion. It seems desirable to determine activation energies for creep of magnesium from 0·5 to $1{\cdot}0\,T_m$, using the cyclic temperature method, to check and extend these results. The creep of polycrystalline cadmium in the range 0·5 to $0{\cdot}8\,T_m$ (Frenkel *et al.* 1955) is associated with a constant activation energy about equal to that for self-diffusion. However, no observations of slip mechanisms appear to have been reported for cadmium at high temperatures. For polycrystalline thallium, creep in the range 0·5 to $0{\cdot}8\,T_m$ (Sherby 1958), at which temperature it transforms to a body-centred cubic structure, is associated with an activation energy equal to that for self-diffusion. However, no investigation of slip systems in thallium has yet been reported. Clearly, further work is necessary to establish the relation of creep to crystallographic flow mechanisms in hexagonal metals.

§ 4. Conclusions

1. The experimental activation energies found for creep of pure polycrystalline zinc above one-half the absolute melting temperature tentatively suggest that creep of this material is controlled by two thermally activated processes acting additively.

2. At low temperatures, 0·5 to $0{\cdot}6\,T_m$, a low activation energy process is dominant, with $Q_c = 21{\cdot}0$ kcal per mole. This value suggests that creep is controlled by dislocation climb.

3. A high activation energy process is dominant in the temperature range 0·8 to $1{\cdot}0\,T_m$ with $Q_c = 38{\cdot}0$ kcal per mole. It is suggested that creep in this temperature range is controlled by crystallographic flow on the prism plane.

4. Recent creep theories do not describe completely the high temperature creep of polycrystalline zinc.

Acknowledgments

This work was carried out during the tenure of a University Research Fellowship (W.J.T.) and a U.S. National Science Foundation Post-Doctoral Fellowship (O.D.S.). The authors wish to thank Professor A. G. Quarrell for provision of facilities, and encouragement during the work. The authors are also grateful to Imperial Smelting Corporation, Avonmouth, for analyses of the zinc used in this investigation.

References

Cahn, R. W., Bear, I. J., and Bell, R. L., 1953–54, *J. Inst. Metals*, **82**, 481.
Cottrell, A. H., and Aytekin, V., 1950, *J. Inst. Metals*, **77**, 389.
Frenkel, R. E., Sherby, O. D., and Dorn, J. E., 1955, *Acta Met.*, **3**, 470.
Gertsriken, S. D., and Pryanishnikov, M. P., 1957. All Union Conference on the Application of Radioactive and Stable Isotopes in the National Economy and Science, Moscow Edition of the Academy of Sciences, SSSR.

Gilman, J. J., 1956, *Trans. Amer. Inst. min. (metall.) Engrs*, **206**, 1326.
Jaumot, Jr., F. E., and Smith, R. L., 1956, *Trans. Amer. Inst. min. (metall.) Engrs*, **206**, 137.
Kidson, G. V., and Ross, R., 1957, *International Conference on Radioisotopes*, Paris.
Liu, T., and Drickamer, H. G., 1954, *J. chem. Phys*, **22**, 312.
Lytton, J. L., Shepard, L. A., and Dorn, J. E., 1958, *Trans. Amer. Inst. min. (metall.) Engrs*, **212**, 220.
Miller, P. H., and Banks, F. L., 1942, *Phys. Rev.*, **61**, 548.
Pomp, A., and Länge, W., 1936, *Mitt.-K.-Wilh.-Inst. Eisenforsch.* **18**, 51.
Ramsey, J. A., 1951–1952, *J. Inst. Metals*, **80**, 167.
Schmid, E., 1931, *Z. Elektrochem.*, **37**, 447.
Sherby, O. D., 1958, *Trans. Amer. Inst. min. (metall.) Engrs* (to be published).
Sherby, O. D., and Frenkel, R. E., 1954, *Trans. Amer. Inst. min. (metall.) Engrs*, **200**, 690.
Sherby, O. D., and Lytton, J. L., 1956, *Trans. Amer. Inst. min. (metall.) Engrs*, **206**, 928.
Sherby, O. D., Orr, R. L., and Dorn, J. E., 1954, *Trans. Amer. Inst. min. (metall.) Engrs*, **200**, 71.
Shirn, G. A., Wajda, F. S., and Huntington, H. B., 1953, *Acta Met.*, **1**, 513.
Tietz, T. E., and Dorn, J. E., 1956, *Trans. Amer. Inst. min. (metall.) Engrs*, **206**, 156.
Vinaver, W., and Druelle, P., 1955, *Rev. Met.*, **52**, 612.
Weertman, J., 1955, *J. appl. Phys.*, **26**, 1213; 1957 a, *Ibid.*, **28**, 362; 1957 b) *Ibid.*, **28**, 1185.
Weertman, J., and Shahinian, P., 1956, *Trans. Amer. Inst. min. (metall.) Engrs*, **206**, 1223.

On the Delay Time in Plastic Flow of Indium Antimonide†

By J. W. Allen
Services Electronics Research Laboratory, Baldock, Herts.

[Received April 15, 1958; and in revised form June 6, 1958]

Abstract

The delay time before the onset of plastic deformation has been studied as a function of temperature and stress for indium antimonide in uniaxial compression. The temperature range was 150–350°c, and the stresses were about 10^6–10^7 dynes/cm^2. An empirical relation of the form $\tau = \text{const.}\ \sigma^{-n}T \exp(E/kT)$ has been found. A theory of dislocation production is advanced to explain these results.

§ 1. Introduction

When a small force is applied to a single crystal of indium antimonide there is a delay before flow begins (Allen 1957). A similar phenomenon is observed in germanium and silicon (Gallagher 1952). Various interpretations of this have been suggested, and it was the aim of the present work to provide data on the variation of the delay time with stress and temperature in order to distinguish between these interpretations. The observations have, in fact, suggested a new model which seems to be in better accord with the experiments than previous ones.

Since plastic flow is to be interpreted in terms of a dislocation mechanism both the number of dislocations and their movement will be involved. We have chosen to concentrate on the former in our experiments since the onset of plastic flow in these materials is marked by a very rapid increase in dislocation density. The etch-pit technique offers a convenient way of measuring this density.

§ 2. Experiment

In the experiment a single crystal block was compressed under a given stress at a given temperature and the time under these conditions which elapsed before the dislocation density increased was measured. This was repeated for a range of temperatures and stresses.

The specimens were rectangular blocks, 2·8 mm × 0·9 mm × 0·6 mm, with a (111) face on one of the long narrow sides. They contained an average of fifteen dislocations each (determined by etch-pit count) and were cut from a region of the bulk crystal where the dislocation density was reasonably uniform. They were compressed in a piston and cylinder arrangement in air. Under the conditions of the experiment only very light oxidation occurred even at the highest temperatures used. In

† Communicated by the Author.

order that the stress should be a pure linear compression the piston was made to a sliding fit in its cylinder, and soft lead platens wrapped in thin pure aluminium foil were used to distribute the stress uniformly and to prevent frictional forces along the surface. (The aluminium wrapping was necessary to prevent alloying between the lead and the indium antimonide: for one reading at 350°c pure aluminium was substituted for the lead.)

The cylinder and piston and the specimen were heated separately in a furnace to the required temperature, after which the specimen was placed between its platens in the cylinder and a load was applied. After a suitable time the load was removed and the specimen was taken from the furnace, thereby quenching it to room temperature in a few seconds. It was polished chemically and etched to show dislocations (for details of these procedures and of 111 etch see Allen (1957)) and examined under the microscope. If flow had not begun it was replaced in the furnace and loaded for a further time, and the sequence repeated until flow was observed to have begun. The delay time (also known as the incubation period) was taken to be the total time under load before the onset of flow.

Some points here require further attention. If the specimen is heated and then etched with 111 etch without polishing then etch-pits are produced which are irrelevant to our present purpose, i.e. they do not mark dislocations which penetrate into the bulk crystal. It might be objected that dislocation loops are formed at the surface and would in course of time move through the crystal. Our results would then be misleading, since such loops are removed at each polishing. However, it is found that within the limits of the experiment the delay time is independent of the number of periods of heating (each followed by etching) of which it is the sum: we therefore conclude that in this experiment at least surface sources of the type described should be negligible. These remarks only apply to specimens with carefully prepared surfaces and with a reasonably high number of dislocations present in the bulk. With a smaller initial number of dislocations the results are governed by the behaviour of surface sources. In practice, after a few preliminary experiments the delay time expected under a given set of conditions could be estimated, and the heating periods used were one of about two-thirds the estimated time followed by further periods of about a sixth of that estimated, these being repeated until flow began. In this way about three or four etchings were used for each sample whatever the actual length of the delay time, and this meant that the decrease in size of the specimens due to etching was approximately the same for all of them.

In the initial stages of deformation dislocations were not produced uniformly throughout the crystal, but appeared in localized groups which for reasons which will become apparent later we call avalanches. This is shown in fig. 3, Pl. 88. On tracing the dislocations through the bulk material it is found that considerable cross-slip has taken place. Linear arrays in well-defined glide planes did not occur until a much later stage.

It is thought that this effect is characteristic of the deformation mechanism and is not due to a lack of homogeneity in the stress: this is, of course, difficult to prove, but all possible precautions were taken to make the stress homogeneous, and the avalanches did not seem to be particularly associated with the upper and lower surfaces of the specimen, where stress concentrations may be expected to arise.

Fig. 1

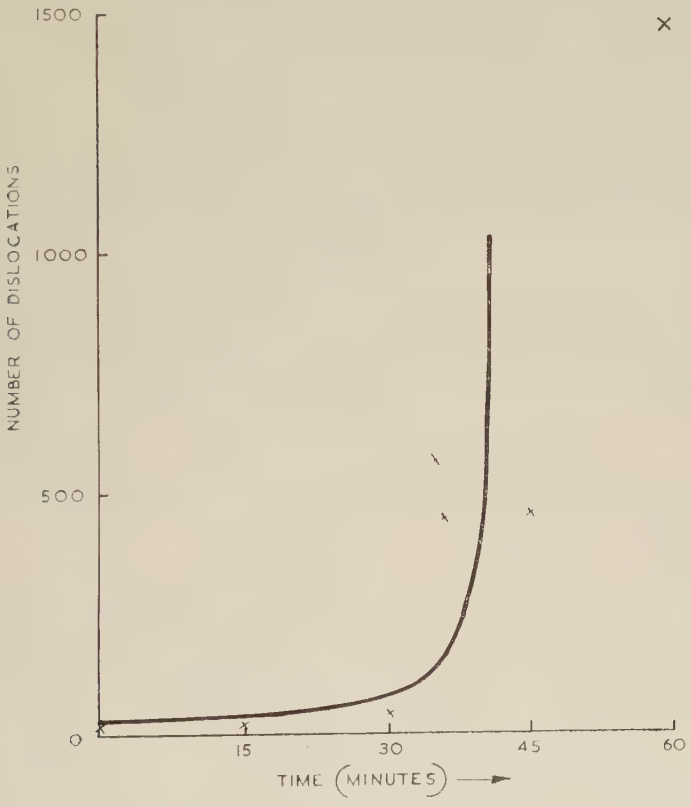

Etch pit count as a function of time of compression at 300°c for a series of InSb specimens. The solid line is that of eqn. (2).

In order to find how the dislocation density increases with time a subsidiary experiment was performed in which a series of InSb blocks were held at the same temperature under the same stress for different times. The etch-pit count as a function of time of heating is given in fig. 1 and it will be seen that the onset of flow is reasonably well defined. In the main experiment flow was deemed to have occurred when the dislocation density had increased by a factor of about four as judged by eye (corresponding to the appearance of an average of two avalanches). This somewhat

arbitrary criterion leads to consistent results, since a factor of two in the dislocation density when flow has begun corresponds to only a small change in the time, as may be seen from fig. 1.

§ 3. Results and Errors

The values of the delay time as a function of temperature and load are presented in the table. The load given therein is the actual weight used in the compression: the orientation of the crystal was such that 100 gm wt gives a shear stress of $1{\cdot}6 \times 10^6$ dynes/cm^2 on the (111) plane most favourably oriented for slip. The stress is proportional to the load within the accuracy set by the scatter in specimen area. The variation in this area was $\pm 6\%$ initially, and the area decreased by 1% on each etching. However, since the number of etches used was approximately the same for each sample, and since they were applied at roughly the same fraction of the delay time, the total inaccuracy in the stress, taken as proportional to load, should not be greater than $\pm 8\%$. The temperatures were measured with a calibrated chromel–alumel thermocouple inserted in the cylinder and were controlled to ± 5°c. Most of the temperature variation was in the first few minutes after loading the specimen. The method of estimating the delay time described above should give values with an uncertainty not greater than $\pm 15\%$ and the scatter of values obtained when a number of samples are compressed under the same conditions is within these limits.

Delay Time in Minutes as a Function of Applied Load and Temperature

Temperature (°c)	Load (gm wt)					
	47	66	160	260	455	900
150	—	—	—	—	210	60
200	—	—	200	—	30	—
250	210	70	25	10	5	—
300	40	—	6	—	0·75	—
350	—	—	1	—	—	—

§ 4. Theory

The localized arrays of dislocations formed in the initial stages of deformation suggest an avalanche mechanism, i.e. that dislocation sources are produced by the interaction of dislocations, and that these sources produce further dislocations which interact to produce more sources, and so on. If s is the number of sources per cm^3, n is the density of dislocations per cm^2 and v is their velocity, then in the model the rate of production of sources follows a bimolecular law

$$\frac{ds}{dt} = \beta v n^2, \qquad \ldots\ldots\ldots \quad (1)$$

where β is some constant. As a rough approximation we assume that each source gives off a constant number γ of dislocation loops before these produce a new source and then work-hardens. Observation of the dislocation arrays shows that this number is of the order of 10 in these experiments. Under this assumption the rate of increase of dislocations will be proportional to the rate of increase of sources, that is $dn/dt = \alpha v n^2$. One then has

$$\frac{n}{n_0} = \frac{1}{1-\alpha v n_0 t} = \frac{1}{1-t/\tau_1} \quad . \quad . \quad . \quad . \quad . \quad . \quad . \quad (2)$$

where n_0 is the initial dislocation density and $\tau_1 = (\alpha v n_0)^{-1}$. Equation (2) is plotted as the full curve in fig. 1 and is seen to predict a rapid increase of dislocation density after an initial delay period which is a fraction nearly equal to unity of τ_1.

The mathematical description contained in eqns. (1) and (2) is open to some criticism. Equation (1) is statistical in nature and therefore cannot obtain in the early stages of the compression, for the dislocations initially are so few and so far apart that some time must elapse before any interactions occur at all. It is also implicit in eqn. (1) that all the dislocations are able to move and that their velocities are randomly distributed in space. If those dislocations lying near one preferred glide plane may move more rapidly than others then the number of interactions is more nearly proportional to the first power of n, giving an exponential increase with time in place of the expression in eqn. (2). Again, at a later stage of the deformation work-hardening will set in and this will prevent the divergence to infinity of n as t approaches τ_1. However, the treatment should provide a useful approximation to the actual behaviour of the system.

In the experimental part (§ 2) the incubation period was taken to be the time at which $n \sim 4n_0$, so from eqn. (2) one finds τ to be $\frac{3}{4}\tau_1$. Since this is inversely proportional to the dislocation velocity we require for the interpretation of our results this velocity as a function of stress and temperature. If the dislocations are surrounded by an impurity atmosphere, as seems reasonably certain in these materials, the velocity will be limited by the drag of this atmosphere. Cottrell and Jaswon (1949) have given a theoretical treatment of the effect and have formally solved the problem. They express the impurity atmosphere distribution as a series of hyperbolic Mathieu functions, and show that the force on the dislocation can be expressed as the gradient of the potential energy of an impurity atom, integrated over all the impurity atmosphere. Given the parameters of interest, namely the temperature T, the diffusion coefficient of impurities D, the dislocation velocity v and the coefficient A which occurs in the expression for the interaction energy V of an impurity atom in the strain field of a dislocation, namely

$$V = A \sin\theta/r \quad . \quad . \quad . \quad . \quad . \quad . \quad . \quad . \quad (3)$$

one can find by numerical methods the force F required to maintain the dislocation in a state of steady motion. However, their treatment is not

suited to the inverse problem of determining the parameters from the experimental results, nor does it lead to explicit relations between the parameters.

We have therefore taken the basic equations of Cottrell and Jaswon's formulation, namely the differential equations describing the movement of impurities and the conservation of their number together with the integral which relates the force on the dislocation to the perturbation of the impurity atmosphere, and by suitable transformation of variables we have derived the following functional relation:

$$\frac{vA}{DkT} = f\left(\frac{F}{\mu c_0 A}\right) \qquad \ldots\ldots\ldots \quad (4)$$

Fig. 2

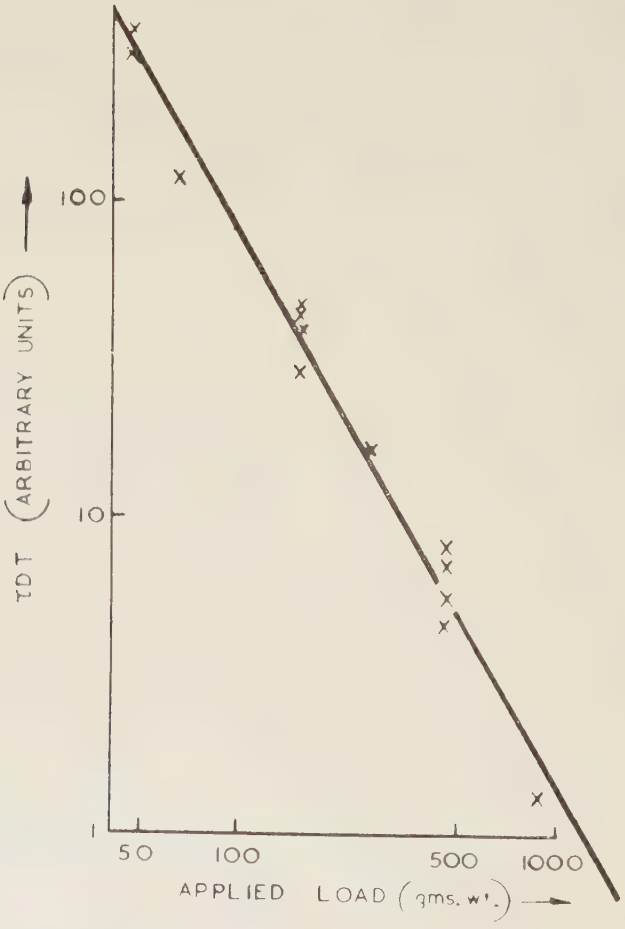

Logarithmic plot of τDT against applied load, showing the functional relationship between these quantities.

in which μ is the number of solvent atoms in unit volume, and c_0 is the impurity concentration far from a dislocation. These two factors and the quantity A vary only slightly with temperature and may therefore be taken as constants in our experiment. Remembering that the incubation period τ is inversely proportional to the dislocation velocity, one finds

$$\tau DT = g(F). \quad . \quad . \quad . \quad . \quad . \quad . \quad . \quad (5)$$

§ 5. Comparison of Theory and Experiment

It is expected that the diffusion constant of impurities will be of the form $D_0 \exp(-E/kT)$ where D_0 and E are independent of temperature. From eqn. (5) it follows that E can be found from the slope of a plot of $\ln \tau T$ against T^{-1} at constant stress F. This procedure yields a value of 0·78 ev. If one then plots τDT against F, using this value for E, the results should lie on a single curve. All the results given in the table are plotted in this manner in fig. 2. It is seen that a good representation of them is given by the equation

$$\tau DT = \text{const } F^{-1\cdot 74} \quad . \quad . \quad . \quad . \quad . \quad . \quad . \quad (6)$$

in accordance with the functional requirement of eqn. (5).

§ 6. Discussion

Not much significance is to be attached to the exact value of the exponent 1·74 in eqn. (6) since this is a power-law approximation to an expression which is expected to be much more complex. In fact we have performed a similar analysis of some results of Treuting (1955) for germanium and have found an expression of the type of eqn. (6) with an exponent 1·37. One point, however, deserves attention and this is that previous treatments of this type of microcreep have been based on the assumption that the velocity is proportional to the stress, in accordance with Einstein's diffusion relation (Cottrell 1953). But the number of impurities bound near the dislocation might be expected to decrease as the dislocation velocity increases: pictorially, the moving lattice washes away some of the impurity atmosphere. This gives a velocity increasing with stress faster than linearly and this agrees with our result.

So far the drag on the dislocation has been attributed to impurities but it may well be that the production of interstitials and vacancies is of greater effect. There are then two processes to consider, namely the production of defects and their diffusion away. If the former is the limiting process than Friedel (1956) has shown that the velocity should be linearly related to the force by the Einstein equation, while if the latter process is limiting then the treatment we have given should still be correct with defects taking the place of impurities. It may be noted that the diffusion energy for self-diffusion of antimony in InSb is 0·75 ev (Boltaks and Kulikov 1957), not significantly different from the value

0·78 e v which appears in our results. This is almost certainly a coincidence, since the same correlation between the energies does not hold for germanium.

Seitz (1952) has proposed a rather different explanation of the delay time in which he assumes the existence of Frank–Read sources which initially cannot multiply because the active length is locked by impurities. If a stress is applied then thermal vibrations enable the source to free itself from the impurities and slip begins. In this model the activation energy derived from a plot of $\ln \tau$ against T^{-1} is interpreted as the energy binding impurities to a dislocation. Although the experimental values, of the order of an electron-volt, are rather high for this interpretation this may be due to the addition of a bonding energy to the elastic interaction. Seitz treats only a single source and does not consider how the effects of a number of sources will add to give the behaviour of the whole crystal. Unless all the sources acting are roughly of the same length the sharp onset of flow due to a single source will be smeared out. This objection can be met by assuming that the probability of occurrence of a Frank–Read source is a rapidly decreasing function of its length, for example, $\exp(-l/b)$. Then since at a given stress there will be a minimum length for an active source the active source lengths will have a distribution sharply peaked at a certain value, and so all sources will begin to multiply at roughly the same time. A more serious objection to Seitz' theory is that it would seem to predict the appearance of well defined slip lines in the initial stages of deformation followed later by interaction configurations, contrary to the observations.

The crucial experiment which would distinguish clearly between the mechanism of Seitz and the avalanche mechanism would be that of determining dislocation velocities as a function of stress and temperature, rather than the delay time. This has not been found possible so far because the presence of impurities at a dislocation causes its etch-pit to be rather diffuse, and this renders the unambiguous identification of individual dislocations in our crystals as grown extremely difficult. The dislocations introduced by deformation do not have dense impurity atmospheres, of course, and so can be identified easily. A related problem prevents the determination of the relation between delay time and dislocation density predicted by eqn. (2), for until the locking impurities are identified it will not be possible to produce crystals with different dislocation densities but the same impurity atmosphere concentration. Correlation between τ and n_0 can therefore only be qualitative at this stage, but crystals with high dislocation density do seem to have short delay times.

No hypothesis has been advanced above concerning the detailed mechanism of dislocation multiplication in the avalanche, i.e. as to how interacting dislocations can produce sources so oriented that the newly produced dislocations can also interact. A number of such mechanisms are possible in principle, but more detailed information on dislocation dispositions is needed to determine which are acting in practice.

Acknowledgments

Acknowledgment is made to the Admiralty for permission to publish this paper. I should also like to thank Dr. O. Simpson for his advice and encouragement.

References

Allen, J. W., 1957, *Phil. Mag.*, **2**, 1475.
Boltaks, B. I., and Kulikov, G. J., 1957, *J. tech. Phys., Moscow*, **27**, 82.
Cottrell, A. H., 1953, *Dislocations and Plastic Flow in Crystals* (Oxford: University Press), p.138.
Cottrell, A. H., and Jaswon, M. A., 1949, *Proc. roy. Soc.* A, **199**, 104.
Friedel, J., 1956, *Les Dislocations* (Paris: Gauthier-Villars), p. 72.
Gallagher, C. J., 1952, *Phys. Rev.*, **88**, 721.
Seitz, F., 1952, *Phys. Rev.*, **88**, 722.
Treuting, R. G., 1955, *J. Metals*, **7**, 1027.

An Electron Diffraction Study of Ice Deposits formed on Silver Iodide†

By N. D. Lisgarten
Physics Department, Imperial College, London, S.W.7

[Received July 16, 1958]

Abstract

Oriented deposits of hexagonal ice have been formed by condensing water vapour on to silver iodide substrates at temperatures of about −100°c and examined by electron diffraction methods. A feature of the diffraction patterns, obtained from the oriented hexagonal ice, is the appearance of strong spots in the 'forbidden' h k.4 positions. At lower substrate temperatures only unoriented deposits of cubic ice were obtained.

§ 1. Introduction

Some ten years ago Vonnegut (1947) discovered that, in suitable circumstances, small particles of silver iodide were highly effective as nuclei for the formation of ice crystals. When particles of silver iodide were introduced into a supercooled cloud in laboratory experiments, ice crystals began to form at a temperature of about −5°c and at about −15°c most of the particles of silver iodide appeared to serve as ice nuclei. (If no nuclei are present, the spontaneous formation of the ice crystals does not occur until the temperature falls below −40°c.) Vonnegut's discovery has led to several large-scale efforts to produce artificial rainfall by 'seeding' suitable supercooled clouds with smokes of silver iodide. Although it is not possible to say whether these attempts have been successful, the ice nucleating properties of the silver iodide are beyond doubt and it is of interest, therefore, to investigate the manner in which ice is formed on a single crystal of this substance.

Vonnegut chose silver iodide for his nucleation experiments with ice because of the geometrical similarity of the hexagonal lattice of silver iodide and the hexagonal lattice of ice. If the hydrogen atoms of the ice lattice are ignored, the atomic arrangement consists of two interlocking 'close-packed' hexagonal arrays of oxygen atoms, the dimensions of the unit cell being at 0°c,

$$a = 4{\cdot}52\ \text{Å}; \qquad c = 7{\cdot}37\ \text{Å}.$$

The hexagonal lattice of silver iodide also consists of two similarly interlocking 'close-packed' arrays, one formed by the silver atoms and the other by the iodine atoms. At room temperature the unit cell dimensions for hexagonal silver iodide are

$$a = 4{\cdot}59\ \text{Å}; \qquad c = 7{\cdot}51\ \text{Å}.$$

† Communicated by the Author.

The dimensions quoted above have been obtained from the experimental results of Megaw (1934) for ice, and Wilman (1940) for silver iodide, by multiplying their values by 1·002 to convert from X.U. to Å.

The fact that the geometry of the crystal lattices of ice and silver iodide are so closely related suggests that the first step towards establishing the mechanism of nucleation is to conduct experiments to see whether there is any tendency for ice to grow as a single crystal, oriented in some particular manner, on a single crystal of silver iodide. Jaffray and Montmory (1957) have observed oriented ice deposits on silver iodide by means of an optical microscope and electron diffraction methods have been used, for the first time it is believed, in obtaining the results given below. These electron diffraction experiments were conducted at temperatures below $-90°$C; it is impossible to maintain thin deposits of ice above this temperature as they evaporate very rapidly under the vacuum conditions necessary to operate an electron diffraction camera.

§ 2. Preparation of Silver Iodide Substrates and Experimental Procedure

Because it is difficult, if not impossible, to obtain suitable crystals of silver iodide prepared by the usual methods of crystal growth, recourse to the following procedure was made. Silver was evaporated from a hot tungsten wire *in vacuo* and allowed to deposit on to thin pieces of freshly cleaved mica which were maintained at a temperature of about 270°C during the deposition process. This produced monocrystalline and apparently atomically flat layers of silver having their (111) faces parallel to the cleavage face of the mica (see Newman and Pashley 1955). The pieces of mica carrying the layers of silver were then subjected to chemical attack by suspending them in an atmosphere in equilibrium with a weak solution of iodine in water. By this means the oriented silver layers were converted to oriented layers of silver iodide. It was necessary to conduct the exposure of the silver to the iodine vapour in darkness, as it was found that daylight, particularly when bright, brought about the decomposition of the silver iodide, leaving a mainly randomly arranged deposit of silver crystallites as the final product.

The chief orientations of silver iodide (which frequently occur as a mixture of two forms—one cubic and the other hexagonal—at room temperature), observed by means of electron diffraction on the silver layers, were as follows:

(*a*) (111) cubic AgI parallel to Ag (111),
[$1\bar{1}0$] or $\bar{1}10$ parallel to Ag [$2\bar{1}\bar{1}$].

(*b*) (00.1) hexagonal AgI parallel to Ag (111),
[10.0] parallel to Ag [$2\bar{1}\bar{1}$].

These orientations and also others which are less common have been examined by Pashley (1951). Figure 1, Pl. 89 shows an electron diffraction pattern obtained from an oriented layer of silver iodide. This pattern

is common to both cubic—[$2\bar{1}\bar{1}$] azimuth—and hexagonal—[$1\bar{1}.0$] azimuth—forms of silver iodide. Not infrequently the cubic form predominated although occasionally patterns consistent with a largely hexagonal orientation were obtained. A pattern from a cubic deposit—[$1\bar{1}0$] and [$\bar{1}10$] azimuths—is shown in fig. 2, Pl. 89.

Specimens of silver iodide so prepared were mounted in a special low temperature unit which enabled the silver iodide to be maintained at any desired temperature down to about $-170°$C. The low temperature unit was then placed in the electron diffraction camera and deposits of ice were formed from water vapour injected on to the silver iodide substrate from a glass apparatus connected to the camera. Ice, contained within the glass apparatus and maintained at a suitably low temperature, constituted the source of water vapour. The complete apparatus and method of obtaining such deposits of ice are described more fully by Blackman and Lisgarten (1957).

§ 3. Experimental Results and Discussion

It is convenient to consider the results of the ice deposition experiments in three parts. The first deals with deposits on the silver iodide substrate at an initial temperature of about $-100°$C or a little higher. As soon as the deposits were formed the temperature of the substrate was allowed to fall as rapidly as possible to about $-130°$C so that the diffraction patterns could be observed and recorded without fear of the ice evaporating. In this series of experiments orientation of the ice was obtained. A pattern recorded from such a deposit is illustrated by fig. 3, Pl. 90 which shows diffraction spots due to hexagonal ice—[$1\bar{1}.0$] azimuth—superimposed on the corresponding array of diffraction spots due to the silver iodide. (Figure 4 gives the indices of the diffraction spots due to the ice.) In this particular experiment, the substrate consisted of a largely cubic orientation of silver iodide and the identity of the hexagonal ice was easily established by examining the diffraction pattern associated with the other principal azimuth. Thus, several of the diffraction spots due to the oriented ice – ice [10.0] azimuth—cannot be associated with corresponding diffraction spots due to the cubic silver iodide. When the temperature of the substrate was raised, it was possible to observe the disappearance of the diffraction spots due to the hexagonal ice as the ice evaporated. The remaining pattern due to the cubic silver iodide was generally similar to that shown in fig. 2. Another example of a pattern from an oriented deposit of hexagonal ice is shown in fig. 5, Pl. 90. Here the deposit was somewhat thicker than that of the deposit illustrated by the pattern of fig. 3. The diffraction spots as observed on the fluorescent screen of the camera were relatively bright and the ring system which can also be seen in fig. 5 is consistent with a random array of hexagonal ice crystallites. On warming, the bright diffraction spots and rings due to the ice were observed to disappear leaving a poor pattern of weak spots from the silver iodide together with

some rather diffuse rings indicative of the formation of silver; this resulted from the decomposition of the silver iodide under the action of the electron beam.

The second type of experiment was conducted with the substrate at an initial temperature of about −130°c, in which region it was expected that cubic ice would be formed. Only unoriented deposits of crystallites of cubic ice were observed on the silver iodide in this case. For the third kind of experiment, the substrate temperature was lowered to about −165°c and in this region 'amorphous' ice was obtained. Deposits of this type were then heated slowly until the cubic form appeared. No orientation of the ice was observed in these experiments.

Fig. 4

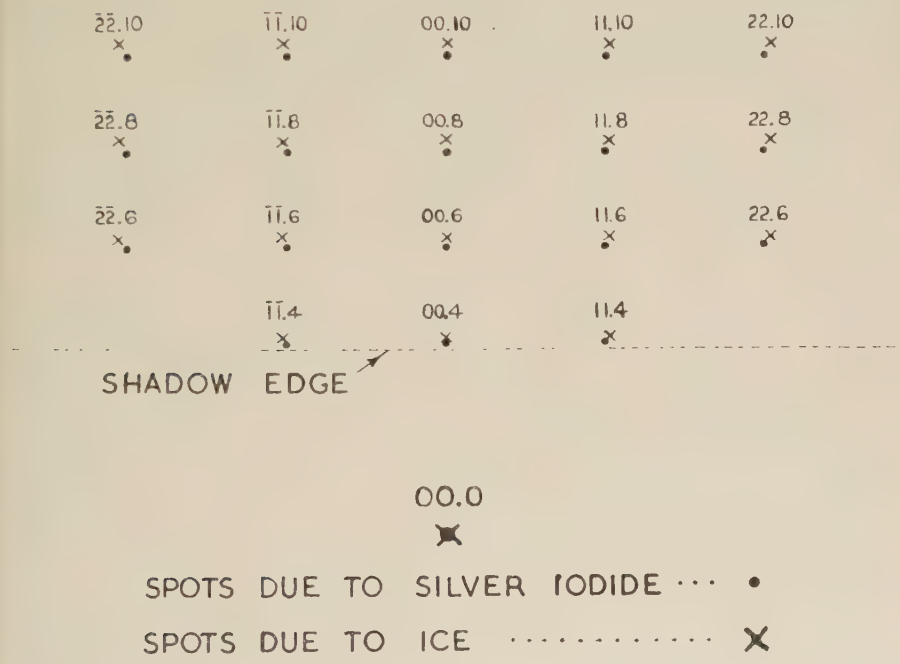

Analysis of the pattern shown in fig. 3, Pl. 90. The indices given refer to the spots due to the hexagonal ice.

The fact that there appears to be a temperature limit (at about −100°c) below which orientation of the ice on the silver iodide cannot be obtained is not entirely unexpected and analogous cases are known. For example, silver forms an unoriented deposit on a mica base at room temperature, but forms excellent monocrystalline layers on mica which has been heated to about 270°c. What is perhaps surprising is that orientation of the ice on the silver iodide does occur at such low temperatures; it seems reasonable to conclude, therefore, that at higher temperatures the silver iodide is a very efficient 'orienting agent'.

A prominent feature of the diffraction patterns obtained from the oriented hexagonal ice is the occurrence of fairly strong diffraction spots in the 'forbidden' h k.4 positions. These can be observed in figs. 3 and 5 and their positions are indicated by the diagram in fig. 4. In the case of fig. 3, the h k.4 ice spots are just separated from the silver iodide spots and since the cell dimensions of the ice are slightly smaller than the corresponding cell dimensions of the silver iodide, the spots due to the ice appear at slightly greater distances from the central spot of the diffraction pattern than do those due to the silver iodide. As in the case of the 'forbidden' rings (e.g. hexagonal 00.4 and cubic 222) of the electron diffraction patterns obtained from unoriented aggregates of ice crystallites (Honjo *et al.* 1956, Blackman and Lisgarten 1957) there arises the problem of accounting for the corresponding 'forbidden' diffraction spots in these h k.4 positions in the patterns from the oriented layers of hexagonal ice. The 00.4 spots are the hexagonal counterparts of the 222 reflections which have been observed in the case of single crystals of silicon (see Heidenreich 1950) as well as in the case of diamond itself. The 222 spots observed in the reflection patterns from silicon and diamond are almost certainly due to dynamical scattering effects. In the case of ice one must expect on the basis of the Pauling (1935) ice model that the hydrogen atoms play some part in producing these h k.4 spots. It is unlikely that the hydrogen atoms are solely responsible for the effects observed in the reflection patterns from the oriented ice deposits. The h k.4 spots are almost of the same intensity as the others, whereas if one examines a transmission pattern from unoriented hexagonal ice of roughly the same thickness, the h k.4 rings are very weak compared with other rings. If the relatively strong h k.4 spots were produced solely by diffraction from hydrogen atoms, there would be no reason to expect the corresponding rings from the transmission patterns to be relatively so weak. It is therefore concluded that the h k.4 spots in the patterns from the oriented ice are produced mainly by dynamical interaction or multiple diffraction from oriented but different crystals.

Measurements made on reflection patterns of the type shown in fig. 3 indicate that, at a temperature of about $-130°$C, the dimensions of the lattice of silver iodide are between 2 and 3% greater than dimensions of the ice lattice. According to Blackman and Lisgarten (1957), the lattice dimensions for ice at $-110°$C are

$$a = 4{\cdot}493 \text{ Å}; \qquad c = 7{\cdot}337 \text{ Å}.$$

These values are about $2\frac{1}{2}$% less than the room temperature lattice dimensions of silver iodide (Wilman 1940) already quoted. It follows, then, that the lattice dimensions of silver iodide do not change appreciably between room temperature and $-110°$C. To check this point, ring patterns from silver iodide were recorded at the above two temperatures and the diameters of the rings compared. There was no difference between the two within the errors of observation, which were estimated to be about 0·2%.

Acknowledgment

The author wishes to express his thanks to Dr. M. Blackman for helpful discussions during the course of these experiments which were carried out as part of the Imperial College interdepartmental research programme on water, organized by Dr. B. J. Mason of the Meteorology Department. The programme was supported by the Department of Scientific and Industrial Research and the Rockefeller Foundation.

References

Blackman, M., and Lisgarten, N. D., 1957, *Proc. roy. Soc.* A, **239,** 93.
Heidenreich, R. D., 1950, *Phys. Rev.*, **77,** 271.
Honjo, G., Kitamura, N., Shimaoka, K., and Mihama, K., 1956, *J. phys. Soc. Japan*, **11,** 527.
Jaffray, J., and Montmory, R., 1957, *C.R. Acad. Sci., Paris*, **244,** 859.
Megaw, H. D., 1934, *Nature, Lond.*, **134,** 900.
Newman, R. C., and Pashley, D. W., 1955, *Phil. Mag.*, **46,** 927.
Pashley, D. W., 1951, *Proc. roy. Soc.* A, **210,** 354.
Pauling, L., 1935, *J. Amer. chem. Soc.*, **57,** 2680.
Vonnegut, B., 1947, *J. appl. Phys.*, **18,** 593.
Wilman, H. 1940, *Proc. phys. Soc., Lond.*, **52,** 323.

Grain Boundary Etching on Pure Aluminium†

By I. Braun
Institute of Technology, Haifa, Israel

and F. C. Frank and G. Meyrick
H. H. Wills Physics Laboratory, Bristol

[Received July 14, 1958]

Abstract

In the etching of recrystallized aluminium (both of 99·99% purity, and zone-refined material) in Lacombe and Beaujard's etchant, the grain boundaries are found to resist attack immediately after electropolishing, but to become susceptible to severe attack after periods of a few days at room temperature. It is suggested that this behaviour is due to diffusion of impurities along the grain boundaries, into the oxide film.

§ 1. Introduction

It is generally agreed that etch pits occur on the surface of aluminium at places where there is a change, either physical or chemical, in the composition of the oxide film. Such changes may be associated with the points of emergence of dislocations; the presence of impurity precipitates; or more probably, combinations of the two. Clear evidence that dissolution can occur where dislocations meet the surface is given by the alignment of pits along the traces of sub-boundaries on aluminium crystals in the work of Lacombe and Beaujard (1948), Lacombe (1947) and Cahn (1949). The pits composing these alignments are sometimes irregularly spaced, which suggests that the presence of a dislocation alone is insufficient to promote etching. Instead, it is more reasonable to suppose that an etch pit will form only on a dislocation upon which impurities have precipitated. This conclusion, that regions of the surface susceptible to attack are produced by the combination of impurities and dislocations was reached by Wyon and Crussard (1951) and also by Forty and Frank (1955).

When aluminium polycrystals are etched with Lacombe and Beaujard's etchant soon after polishing, pits rarely occur along the grain boundaries. Specimens grown from the melt show characteristic 'clear lanes' along the grain boundaries; these lanes being bounded by high density regions of etch pits on rapidly grown polycrystals (Forty and Frank). This does not occur when the samples are prepared by recrystallization; instead, the pits are fairly uniformly distributed over the surface, different grains being discernible by the variations in the orientation of the etch figures

† Communicated by the Authors.

and the appearance of some grain boundaries as lines on the surface. In the above treatments grain boundaries are usually not severely attacked. Lacombe and Beaujard (1948) observed that intercrystalline attack only developed on boundaries between crystals having large differences in orientation. Lacombe (1947) has produced marked dissolution along grain boundaries after prolonged immersion in a 10% solution of hydrochloric acid. Again Wyon *et al.* (1956), using Lacombe and Beaujard's etchant have demonstrated the dependence of boundary etching on purity and quenching treatments.

In the course of the work described here, it was found that by giving polycrystalline aluminium suitable room temperature anneals between polishing and etching with Lacombe and Beaujard's etchant the grain boundaries were made susceptible to attack so that they were marked by lines of pits usually overlapping one another. This result suggests that during the interval between polishing and etching, impurities were able to diffuse along the grain boundaries to the surface, in sufficient quantities to change its constitution enough to allow it to be readily etched.

§ 2. Experimental Procedure

The observations were made partly on aluminium of 99·99% purity but mainly on the same material further purified by the method of zone refining. The aluminium was refined in the same manner as described by Braun *et al.* (1958), although in this case the treatment was carried to a further stage, eighteen passes being given to the ingot. After the third and tenth pass a portion of the impure end was cropped and replaced by an equal amount of the starting material, so that the length of the rod remained the same.

This treatment produced aluminium of sufficient purity to enable it to recrystallize at −45°C in six to seven days after a 95% compressional deformation. Three single crystal specimens from different parts of an ingot prepared in the above way, showed residual resistances of 1/3000, 1/3500 and 1/3900 of the room temperature value. (These ratios were measured by Dr. D. Shoenberg at Cambridge.)

To facilitate the production of etch figures, portions of the metal were cold rolled and cut into plates of dimensions about $2\frac{1}{2} \times 1 \times 0{\cdot}2$ cm. These plates were then divided into three groups; groups A and B consisting of refined material and group C of 99·99% aluminium. Batch A was allowed to recrystallize at room temperature for a day, whereas B and C were annealed at 600°C for six days and then cooled in calm air.

After these recrystallization treatments all the specimens were carefully polished, first on a rotating flat wheel covered with selvyt cloth soaked in Brasso and then electrolytically in a bath of 66% acetic anhydride and 33% perchloric acid, cooled in ice. The surfaces were finally washed under a jet of water, rinsed in alcohol and dried with ether.

Etching was carried out in Lacombe and Beaujard's etchant maintained below 10°C, and followed by the same washing procedure as after polishing. The manner in which the etching was performed was somewhat complicated,

each specimen being exposed to the etchant several times. Between each etch the surfaces were not repolished, but the aluminium was stored in a desiccator at room temperature. Again, some specimens received their first etch immediately after polishing, while others were stored for several days before treatment. This procedure made it possible to examine the etch patterns produced in the normal way, i.e. on etching immediately after polishing; and also to follow the changes produced by ageing at room temperature.

§ 3. Results

The results obtained fall into three categories, namely:

(*a*) Observations on surfaces etched immediately after polishing.

(*b*) Observations on the same surfaces as (*a*) when etched again after various times of storage at room temperature.

(*c*) Observations on specimens which received their first etch after ageing at room temperature.

(*a*) *Etching Carried Out Immediately after Polishing*

For the 99·99% pure specimens of group C, an etch of 5–10 seconds duration was enough to produce a high density of small pits, fairly uniformly distributed over the surface. The presence of grain boundaries had little marked effect on the distribution of pits; although very occasionally some pits lay along the boundaries. Usually, however, the boundaries were seen by the variations in the orientations of the pits or when the surface was viewed slightly out of focus. Figure 1† shows a region in which the grain boundary pitting is a maximum for such a specimen. The surface is slightly out of focus to show up the grain boundaries. A feature of the photograph is the tendency for many of the pits to form lines; this is probably due to the fact that this specimen was not electropolished sufficiently long to remove all the traces from mechanical polishing.

A marked change in the configurations was observed on the pure material comprising groups A and B compared to those seen in the case of group C. The general density of pits was much smaller, a fact which allowed the etching times to be considerably lengthened. In addition to the expected increase in resistance to dissolution, it was found that the distribution of pits was not uniform, but varied from one grain to another depending on orientation as found by Lacombe and Beaujard (1948). The least densities of pits occurred in grains whose surfaces were close to the (100) orientation, while the highest densities were found on those surfaces close to the (111) orientation, the orientations being estimated from the shapes of the pits, which tend to be bounded by cube faces with the etchant used. A striking example of this is shown in fig. 2, which shows a region of the surface of a specimen of group B (which had been annealed for six days at 600°C) after an etch of 60 seconds. Figure 3 shows a part of the severely attacked grain at high magnification, and reveals the orientation as fairly

† All figures are Plates

close to (111). Two pits found on a neighbouring grain which was only slightly pitted, are shown in fig. 4; these pits being square and flat bottomed indicate that the orientation is near (100).

In general, most of the grain boundaries on the surfaces of the pure material in groups A and B were visible as lines. Lacombe and Beaujard suggested that these traces were not steps due to unequal dissolution of neighbouring grains during polishing or etching, as they were unable to produce a relief effect using oblique illumination. In our case such steps were present on some boundaries after electropolishing, as was shown by interference fringes (fig. 5). Other boundaries, however, did not affect the fringes in any discernible way. Etching did not seem to affect the situation greatly, and no grooves along the boundaries could be detected.

There were usually no pits formed along the grain boundaries of group A specimens (refined material recrystallized at room temperature), but occasionally small portions were attacked, this tendency being even less for group B aluminium which had been annealed at 600°C.

(*b*) *Further Etching after Various Room Temperature Ageing*

It has been mentioned that all the specimens when etched immediately after polishing showed a small amount of grain boundary attack. This only happened at a few places on the surfaces examined, the majority of boundaries being unaffected. The extent of this attack could not be increased by lengthening the etching time, as this merely produced deeper troughs at places where pitting did occur. However, when the surfaces were given another etch after suitable room temperature anneals, the majority of grain boundaries were delineated by troughs of overlapping etch pits. The periods of ageing required were shorter for the aluminium of group A, which had been recrystallized at room temperature, than for groups B and C which had been annealed at 600°C.

In the case of the group A specimens, a time of six days between the etches was sufficient to produce widespread grain boundary attack. Figure 6 shows a region of maximum grain boundary 'troughing' produced by the first etch; the same field of view after a second etch six days later is shown in fig. 7. Another typical result obtained after the second etch is shown by fig. 8.

Group B specimens (refined and annealed at 600°C) showed little grain boundary attack when etched for the second time, six days after the first etch. 'Troughing' was however quite extensive following a third etch two weeks later (fig. 9).

The behaviour of the impure aluminium comprising group C was more or less the same as that of group B with regard to the grain boundary attack. The first and second etches, separated by a room temperature anneal of six days, yielded little boundary pitting, while most grain boundaries showed continuous troughs after the third etch a fortnight later. Figure 10 shows a surface which was etched twice, once immediately after polishing which yielded a configuration similar to fig. 1, and again after three weeks ageing.

(*c*) *Ageing between Polishing and the First Etch*

A number of specimens from group A, which had been recrystallized at room temperature, were stored in a desiccator for six days after polishing. When they were etched at the end of this interval, it was found that the majority of the boundaries were pitted (fig. 11) but the extent of the attack was not as great as when the ageing period had been preceded by an etch immediately after polishing. It was not possible to increase the extent of the troughing by etching again without delay as this only deepened the troughs which already existed. However when a further ageing period of three days was allowed to elapse before etching dissolution was widespread along the grain boundaries, e.g. fig. 12 which shows the same field of view as fig. 11.

§ 4. Interpretation

If an etch pit is formed on the surface of aluminium where there is a singularity in the constitution of the oxide film, such as an impurity precipitate associated with the point of emergence of a dislocation, then we can explain the resistance to solution (when etched immediately after polishing) where a grain boundary intersects the surface by suggesting that this region does not possess sufficient impurities to render it susceptible to attack. Suitable room temperature anneals after polishing enable the traces of the grain boundaries on the surface to be readily etched. This must mean that during the ageing treatments the impurity content of the oxide film along the grain boundaries increases. Moreover, the only conceivable way in which the impurities could accumulate at the surface is by diffusion in the grain boundaries.

Experiments on the self-diffusion of silver by Hoffman and Turnbull (1954) have shown that the rate of diffusion along the grain boundaries is appreciably greater than in the bulk of the crystals for temperatures well below the melting point. Achter and Smoluchowski (1951) also observed greater diffusivity along grain boundaries for the diffusion of silver into copper. It seems reasonable to suppose that the impurities in the aluminium would, at room temperature, be able to diffuse more readily in the grain boundaries than elsewhere, and provided they collected in the oxide film, this would lead to selective attack along the grain boundaries.

The fact that the duration of the room temperature anneal required to produce extensive grain boundary pitting in group A (recrystallized at room temperature) was much less than for B and C (annealed six days at 600°C) is probably explained by the different treatments given to the groups before polishing.

During the process of recrystallization impurities have ample opportunities to occupy many of the available sites on the grain boundaries. An impurity atom on the grain boundary will remain there, provided its adsorption energy to the boundary is great enough to prevent it diffusing into the bulk of the metal. This is more likely to be true at room temperature than at 600°C. Consequently it is possible that aluminium recrystallized at room temperature (group A) would possess a higher concentration

of impurities on the grain boundaries than aluminium which had been annealed at 600°C for six days (group B). If this is true then group A aluminium would require a shorter ageing time (to render the boundary traces on the surfaces attackable) than group B.

In the case of the aluminium which was allowed to recrystallize at room temperature it might be expected that in addition to a general high concentration of impurities on the grain boundaries some portions of large angle boundaries might possess large enough accumulations of impurities to be attacked immediately after polishing, provided these regions are intersected by the plane of polish. A small amount of this was in fact observed and, moreover, such an occurrence on the surfaces of group B was very rare.

It might, at first, be expected that the material comprising group C (99·99%) pure would exhibit marked grain boundary attack after shorter periods of room temperature ageing than in the case of group B, because of its greater impurity content. No marked evidence of this was observed, the behaviour of the two groups being more or less the same.

A possible explanation is that the impurities in the material, as received, were in such stable precipitates that very little change occurred during annealing at 600°C, with the result that only small quantities were available for diffusion at room temperature. Even if the impurities were all in solution at 600°C they would tend to form precipitates on cooling; leaving only a small amount still dissolved (in addition to small precipitates which may possibly redissolve) to take part in the diffusion processes we are considering.

If such a situation is true, it may well happen that the times of room temperature anneal required to stimulate grain boundary etching would be approximately the same for groups B and C, as is observed in practice.

Acknowledgment

One of the authors, G. Meyrick, wishes to express his gratitude to the Department of Scientific and Industrial Research for a maintenance grant.

References

Achter, M. R., and Smoluchowski, R., 1951, *J. appl. Phys.*, **22,** 1260.
Braun, I., Marshall, S., Frank, F. C., and Meyrick, G., 1958, *Phil. Mag.*, **3,** 208.
Cahn, R. W., 1949, *J. Inst. Metals*, **76,** 211.
Forty, A. J., and Frank, F. C., 1955, *J. phys. Soc. Japan.*, **10,** 656–663.
Hoffman, R. E., and Turnbull, D., 1954, *Acta. Met.*, **2,** 419.
Lacombe, P., 1947, '*Strength of Solids*', *Report on Bristol Conference* (London: The Physical Society).
Lacombe, P., and Beaujard, L., 1948, *J. Inst. Metals*, **74,** 7.
Wyon, G., and Crussard, C., 1951, *Rev. Metall.*, **48,** 121.
Wyon, G., Marchin, J. M., and Lacombe, P., 1956, *Rev. de Met.*, LIII, No. 12,

The Runaway Effect in a Fully Ionized Plasma†

By E. R. Harrison
Atomic Energy Research Establishment, Harwell

[Received July 21, 1958]

Abstract

The conditions for producing runaway electrons in a fully ionized gas are considered, using Chandrasekhar's coefficient of dynamic friction. The runaway currents emitted continuously from linear plasmas are then estimated and are shown to be in agreement within an order of magnitude with the results from some preliminary experimental work. The rate of increase of runaway currents in closed circuits, such as toroidal plasmas, is estimated and is found to be proportional to t^2 (t=time). From some recently published results with toroidal plasmas it is shown that the runaway current, provided it is contained and is not drastically affected by the magnetic fields, can rapidly become comparable in value with the conduction current. In the experimental work with linear plasmas, x-rays were observed having an energy greater than the applied potential difference to the apparatus.

§ 1. Introduction

It is readily shown that in a fully ionized plasma there must always be some fraction of the electrons which will be decoupled by an electric field, no matter how small this field might be, and will then be continuously accelerated. Thus, in addition to the conduction current there will always be a 'runaway' current. Hoyle (1949) and Parker (1957) have invoked the idea of runaway particles in connection with the physics of solar flares; Gibson (1957) and Linhart (unpublished) have discussed the subject from the point of view of toroidal discharges.

In the present paper the subject is treated briefly and the runaway currents emitted continuously from linear plasmas are estimated; similarly, runaway currents in closed circuits such as toroidal plasma are also estimated. As one might expect, the value of these currents is critically dependent on the strength of the electric field.

Given conditions which are otherwise steady, a runaway current constrained to flow in a closed circuit increases at a rate of approximately t^2, where t represents time. A runaway current in many cases can therefore become comparable in value with the conduction current and have an appreciable effect in the hydromagnetic behaviour of plasmas.

The results of some preliminary experimental work with neutralized runaway electron beams, emitted endwise from linear plasmas, are shown to be within an order of magnitude agreement with the theory.

† Communicated by the Author.

§ 2. The Runaway Effect in a Fully Ionized Plasma

Let an electron of mass m_1 and charge e_1, having an initial velocity v_1, move through a plasma containing particles of mass m_i, charge e_i, density n_i, and temperature T_i. Chandrasekhar (1942, 1943) has investigated a similar problem of a star moving through a star field having a Maxwell–Boltzmann velocity distribution. On making suitable substitutions in Chandrasekhar's expressions one finds that the mean rate of increase Δv in the direction of the initial velocity, due to encounters producing small deflections, is

$$\langle \Delta v_{\parallel} \rangle_1 = - \sum_i \frac{D_i n_i}{m_1^2 v_1^2} \left(1 + \frac{m_1}{m_i}\right) \left(1 - \frac{\delta n_i}{n_i}\right) \quad . \quad . \quad . \quad (1)$$

in which δn_i is the number of the ith particles having speeds $v_i \geqslant v_1$, and $D_i = 4\pi e_1^2 e_i^2 \ln \Lambda$, where Λ is the mean ratio of the Debye shielding distance to the impact parameter for large angle scattering (Spitzer 1956). In a plasma consisting of electrons ($i=1$) and positive ions ($i=2$), with $n_1 \simeq n_2 = n$, the coefficient of dynamic friction given by eqn. (1) becomes

$$\langle \Delta v_{\parallel} \rangle = - \frac{D_1}{m_1^2 v_1^2} (3n - 2\delta n_i - \delta n_2). \quad . \quad . \quad . \quad . \quad . \quad (2)$$

When an electric field E, having an angle θ to the velocity v_1, produces a rate of change of momentum opposite to and greater than the dynamic friction, the mean electron velocity increases. Thus, provided the δn_i are small, there is a critical speed v_c given by $Ee_1 \cos\theta + m_1 \langle \Delta v_{\parallel} \rangle = 0$, such that all electrons having $v > v_c$ and a velocity component in the same direction as E gain energy continuously and contribute to a runaway flux. To a sufficient approximation it will be assumed that the fraction of electrons qualifying for the runaway state is $\delta n_1 / 2n$, and the critical speed is

$$v_c \simeq (3D_1 n / E e_1 m_1)^{1/2} \quad . \quad . \quad . \quad . \quad . \quad . \quad . \quad (3)$$

always provided it exceeds the most probable random speed of the electrons (and therefore also of the ions) and thus allows the non-dominant terms of eqn. (2) to be neglected. Therefore, the assumption made is that $x_c > 1$, where

$$x_c = v_c (m/2kT)^{1/2} = (3Dn/2EekT)^{1/2} \quad . \quad . \quad . \quad . \quad . \quad (4)$$

and $m_1 = m$, $e_1 = e$, $T_1 = T$; or, alternatively, the present treatment applies only for an electric field satisfying $E < E_m$, in which

$$E_m = 6 \times 10^{-8}\, n/T \text{ volts cm}^{-1} \quad . \quad . \quad . \quad . \quad . \quad . \quad (5)$$

and $\ln \Lambda \simeq 13$.

So far only electrons have been considered. However, a necessary condition for a runaway ion is that it has initially an energy at least as great as the most probable electron speed, and therefore for most purposes such ions can be neglected.

§ 3. Estimation of Runaway Currents

3.1. *General Considerations*

On integrating the Boltzmann equation for the runaway electrons, one obtains

$$\frac{\partial n_r}{\partial t} + \frac{c}{e}\,\mathrm{div}\,\mathbf{j}_r = \int \Delta f_r(v)\, d^3v \quad . \quad . \quad . \quad . \quad . \quad . \quad (6)$$

where n_r is the number density, $\mathbf{j}_r$ the current density, and $\Delta f_r(v)$ is the rate at which electrons qualify for the runaway state per unit volume of phase space at velocity v. In this treatment the effect of a magnetic field is not considered; the presence of a magnetic field parallel to E, however, should not appreciably affect the result. When $x_c > 1$ it can be assumed as a first approximation that for a zero electric field the integral expression on the right-hand side of eqn. (6) is equal to one half the rate at which electrons are scattered out of a $v > v_c$ spherical region of velocity space. Hence,

$$\int \Delta f_r(v)\, d^3v = \tfrac{1}{2}\int_{v_c}^{\infty} 4\pi v^2 f(v)\tau^{-1}\, dv$$

where $f(v)$ is the Maxwell–Boltzmann distribution function and $\tau \simeq v/\langle \Delta v_{\parallel} \rangle \simeq v^3 m^2/3Dn$. Thus, eqn. (6) is now very approximately

$$\frac{\partial n_r}{\partial t} + \frac{c}{e}\,\mathrm{div}\,\mathbf{j}_r = \Psi(x_c) \quad . \quad . \quad . \quad . \quad . \quad . \quad . \quad . \quad (7)$$

$$\Psi(x_c) \simeq \frac{3n^2 D \exp(-x_c^2)}{2(2\pi m)^{1/2}(kT)^{3/2}x_c^2}$$

and numerically $\Psi(x_c) = 107n^2 \exp(-x_c^2)/T^{3/2}x_c^2$.

3.2. *Continuous Runaway Currents in Linear Plasmas*

For a uniform electric field in a steady-state plasma of length z, $\partial n_r/\partial t = 0$ and eqn. (7) can be integrated to give

$$\begin{aligned} j_r &= ez\Psi(x_c)/c \\ &= 1{\cdot}7 \times 10^{-17} n^2 z \exp(-x_c^2)/T^{3/2}x_c^2 \text{ amp cm}^{-2}. \quad . \quad . \quad . \quad (8) \end{aligned}$$

For example, when $n = 10^{13}$ cm^{-3}, $T = 10^5$°C, $E = 2$ volt cm^{-1}, then $x_c^2 = E_m/E = 3$, and the runaway current amounts to 0·9 amp cm^{-2} per unit length of plasma. The extreme limit for the validity of the present treatment corresponds to $x_c = 1$, or $E = 6$ volts cm^{-1} in the present example, giving a current density of 20 amp cm^{-2} per cm of plasma. For comparison, the random current density amounts to 80 amp cm^{-2}. For an applied electric field greater than E_m, as given by eqn. (5), the velocity distribution will tend to become appreciably asymmetric and it is therefore unlikely in a steady state condition that a substantially greater current will be achieved. Owing to the rapid way in which $\Psi(x_c)$ varies, appreciable runaway current in linear laboratory discharges is only realized when the electric field is at least of the same order of magnitude as E_m.

If $V = Ez$ is the electric potential difference across the plasma column an alternative expression for eqn. (8) is

$$j_r = j_R \frac{eV}{kT} \exp(-x_c^2) \quad . \quad . \quad . \quad . \quad . \quad . \quad . \quad (9)$$

for a random current density of $j_R = ne(kT/2\pi m)^{1/2}/c$.

3.3. *Runaway Currents in Toroidal Plasmas*

Consider now a fully ionized uniform plasma in which the runaway current can form a closed circuit, as for example, a toroidal shaped plasma. Let this current be contained in the plasma for a time t seconds. For a uniform plasma div $\mathbf{j}_r = 0$, and eqn. (7) may be integrated to give a runaway electron density of

$$n_r = t\Psi(x_c) \quad . \quad . \quad . \quad . \quad . \quad . \quad . \quad (10)$$

provided that in all other respects the plasma is in a steady state condition. A steady state condition implies either that the random electrons are being replenished, or that the loss of random electrons is small in the time t. If, however, the initial random electron number density n is not a constant, then

$$n_r/n \simeq t\Psi(x_c)/\{n + t\Psi(x_c)\}. \quad . \quad . \quad . \quad . \quad . \quad . \quad (11)$$

In a similar discharge (Thonemann *et al.* 1958) with $n \simeq 10^{14}\,\mathrm{cm}^{-3}$, $T \simeq 5 \times 10^5$ °c† one finds $n_r/n \simeq 8\,\mathrm{sec}^{-1}$ from eqn. (10) when the electric field is 1 volt cm^{-1}. For an electric field of 2 volt cm^{-1}, n_r/n increases initially at a rate of $6 \times 10^3\,\mathrm{sec}^{-1}$; the runaway flux if it is totally contained achieves a value of $1/\epsilon$ of the initial random electron density in a time of the order 100 μsec.

Since $\partial j_r/\partial t = n_r e^2 E/mc$, one finds from eqn. (10) (again assuming that other conditions are steady) that the circulating runaway current is

$$\begin{aligned} j_r &= t^2 e^2 E\,\Psi(x_c)/2mc \\ &= 1{\cdot}5 \times 10^{-2}(nt)^2 E \exp(-x_c^2)/T^{3/2}x_c^2\,\mathrm{amp\,cm}^{-2} \quad . \quad . \quad (12) \end{aligned}$$

for a containment time t. Or, using eqn. (11)

$$j_r \simeq ne^2 E\{t - n \ln(1 + t\Psi(x_c)/n)/\Psi(x_c)\}/mc. \quad . \quad . \quad . \quad (13)$$

On inserting the previous values for n and T one finds that in an electric field of $E = 0{\cdot}8$ volt cm^{-1} the runaway current density is $7 \times 10^9 t^2\,\mathrm{amp\,cm}^{-2}$ and in 100 μsec achieves a value approaching the conduction current density which is of the order 100 amp cm^{-2}. It must be emphasized that this method of estimating runaway fluxes has neglected the effect of magnetic fields, and the true results may therefore be considerably modified for example by a transverse field of the kind occurring in a pinched discharge.

† In the present context these values of n and T are used purely as an example and the precise values are not therefore important.

It is interesting to notice that in an idealized closed runaway circuit the current density increases as t^2 and, unlike the linear plasma case, is independent of the linear dimensions of the circuit. In astrophysics, where the time scale is large, it would appear that runaway currents can become important if not predominant even when $x_c \gg 1$.

§ 4. Description of Apparatus

The apparatus that was used in an attempt to produce and study low and high energy runaway electron beams is substantially as shown diagrammatically in fig. 1, and in some respects is described elsewhere (Harrison and Dawton 1958). Section (*a*) consists of a water-cooled low voltage arc operating continuously at a gas pressure of 50–100 μHg. A plasma

Fig. 1

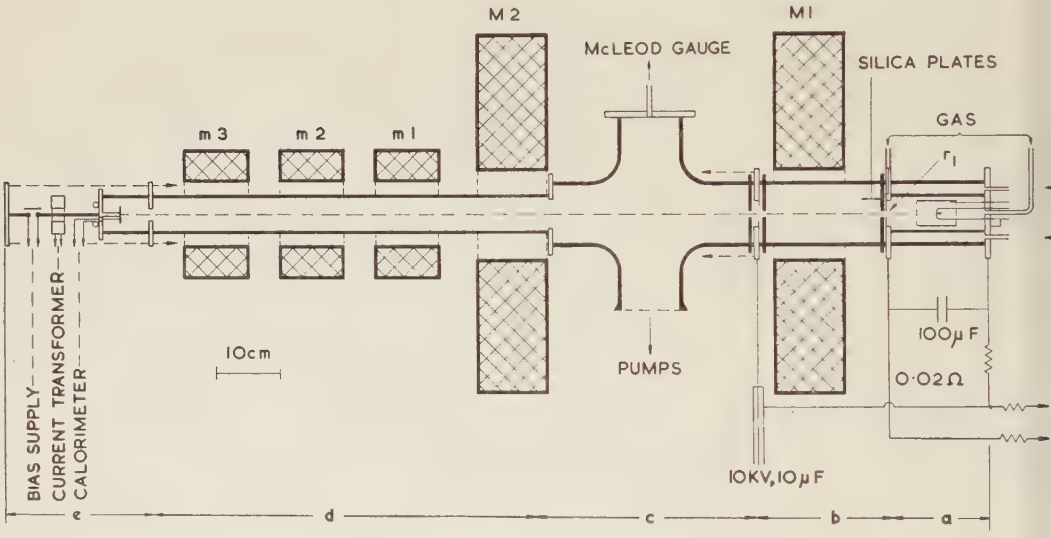

Schematic diagram of apparatus for producing runaway electron beams.

beam is drawn through an aperture of radius r_1 into the next section (*b*), by an applied electric field, and is prevented from diverging by an axially directed magnetic field of approximately 2000 oersteds. The magnetic field is continued into the succeeding sections, although in (*d*) and (*e*) it is reduced in value to around 300 oersteds. To some extent the pressures in (*a*) and (*b*) can be independently controlled. A neutralized beam consisting largely of runaway electrons enters (*c*), where the apparatus is pumped, and is guided by the magnetic field through (*d*) and (*e*) and finally strikes a water-cooled calorimeter target (Harrison 1957). The current returns along six parallel conductors equally spaced round the beam.

§ 5. Low Energy Runaway Electron Beam

For continuous low energy beams of a few hundred ev the first aperture had a radius of $r_1 = 0{\cdot}25$–$0{\cdot}50$ mm in a tungsten disc. Argon was used in all the experiments; attempts to produce low energy neutralized beams with hydrogen were unsuccessful. Figure 2, Pl. 97 shows a runaway beam of electrons produced from an argon discharge.

With applied voltages varying from 200 to 450 volts, beam currents between 0·1 to 1·0 amperes were achieved without any great difficulty. Ion bombardment caused considerable erosion of the tungsten aperture disc, and it was therefore necessary to change this electrode frequently. A typical result was as follows; a beam of 0·7 amperes, having an apparent radius of 1–1·5 mm was produced with 320 volts. The pressures in sections (*a*), (*b*) and (*c*) were 70, 1 and 0·2 μHg; respectively. From the temperature of the calorimeter-target the mean energy of the electrons was found to be 173 ev. On biasing the target over a voltage range of $+30$ to -50 with respect to the aperture-disc electrode immediately preceding it, the temperature was found to vary linearly and it was deduced that the beam contained relatively few electrons with an energy less than 50 ev.

The beams contained very considerable 'hash', and occasionally fluctuations similar to relaxation oscillations were observed (Cutler 1956). An examination of the hash revealed a low frequency, large amplitude component in the neighbourhood of 1 Mc/s which agreed moderately well with the expected frequency of the ion plasma oscillations (Pierce 1948).

From probe measurements made with plasma beams in weak magnetic fields, it was estimated that within a factor of 2 the electron density and temperature were $n \simeq 10^{13}$ cm^{-3} and $T \simeq 10^5$°c. For a plasma column of length $z = 20$ cm the maximum beam current, neglecting the effect of the magnetic field, is 3 amperes from eqn. (8), which agrees within an order of magnitude with the experimental results. The minimum electric field necessary for this current, by eqn. (5), is 6 volts cm^{-1} giving a total potential drop across the plasma column in section (*b*) of at least 120 volts. No doubt there is some residual electric field in the sections (*c*), (*d*) and (*e*), but it is unlikely that these regions will contribute appreciably to the runaway flux owing to the low random electron current density. This point of view receives some confirmation from the fact that when the calorimeter target was biased the beam power varied proportionately.

§ 6. High Energy Runaway Electron Beams

To produce higher energy beams the apparatus was connected to a 10 μF condenser and pulsed at a rate of 1 sec^{-1} at voltages up to 10 kv. Across the low voltage arc of section (*a*), which was kept continuously running, was connected a 100 μF condenser. The radius of the first aperture was

increased to 1–2 mm. The results with hydrogen were substantially the same as those with argon except that slightly higher pressures were necessary. With argon the approximate pressures in sections (*a*), (*b*) and (*c*) were 50, 5 and 0·5 μHg, respectively.

So far the experimental work is incomplete and only preliminary results can be given. It was found that the performance was critically dependent on the pressure in (*b*). When the pressure was too high the discharge in (*b*) of about 10^4 amperes was accompanied by a loud noise; as the pressure was reduced the discharge became silent. Infrequently, these 'silent discharges' were accompanied by the emission of sparks from the target. The discharge, including the beam current reaching the target, usually lasted for approximately 1 msec. As with the low energy beams, considerable hash was observed. A large amplitude component of around 10 Mc/s was readily identified. For optimum conditions the current at the target, measured with a current transformer, was in the region of 200 amperes.

The target current was disappointingly small. The results, however lend support to the idea that substantially larger currents cannot be achieved by using electric fields of $E > E_m$. From the increased pressure in (*b*) one would then expect the current to be of the order of magnitude given when some allowance is made for the increase in the electron temperature. The mean temperature of the calorimeter-target, together with the current measurements, confirmed that the mean kinetic energy of the beam in electron volts was close to that given by the supply voltage.

Measurements of the x-ray emission from the target, using a proportional counter and aluminium filters, revealed the interesting fact that the x-rays had a mean energy of 25–35 kev, although the beam energy had a maximum value of 10 kev. One possibility is that some of the electrons are accelerated owing to variations in the beam current. The maximum possible energy gained by this method is readily estimated. Thus, if eV_0 is the initial energy of a beam of intensity $\frac{1}{2}I_0(1+\cos\omega t)$ and L is the inductance of the system, the maximum energy possible is given by

$$V = V_0 + \tfrac{1}{2}L\omega I_0.$$

For $L \simeq 2\times10^{-6}\,H$ and $\omega/2\pi \simeq 10^7$, this gives a value of 22 kv. Since the beam hash contained higher frequencies it would appear that the x-ray emission can be explained by an acceleration mechanism of this kind.

Acknowledgment

The author is indebted to J. D. Lawson for his encouragement and interest, to A. Gibson, J. G. Linhart and W. B. Thompson for discussions on this subject, and to I. H. Hurdle and G. Soulby for experimental assistance.

References

Chandrasekhar, S., 1942, *Principles of Stellar Dynamics* (Chicago: University Press); 1943, *Astrophys. J.*, **97,** 255.
Cutler, C. C., 1956, *Proc. Inst. Radio Engrs, N.Y.*, **44,** 61.
Gibson, A., 1957, *Third International Discharge Conference. Venice*, p. 365.
Harrison, E. R., 1957, *J. sci. Instrum.*, **34,** 242.
Harrison, E. R., and Dawton, R. H., 1958, *J. Electron. and Control*, **5,** 29.
Hoyle, F., 1949, *Some Recent Researches in Solar Physics* (Cambridge: University Press).
Parker, E. N., 1957, *Phys. Rev.*, **107,** 830.
Pierce, J. R., 1948, *J. appl. Phys.*, **19,** 231.
Spitzer, L., 1956, *Physics of Fully Ionized Gases* (New York: Interscience).

CORRESPONDENCE

On the Temperature Dependence of Yield Stress for Aluminium

By W. D. Sylwestrowicz and D. F. Gibbons
Bell Telephone Laboratories, Inc., Murray Hill, New Jersey

[Received July 31, 1958]

The temperature dependence of yield stress for aluminium has been investigated by Cottrell and Stokes (1955) for single crystals and for polycrystalline material by Sylwestrowicz (1958). In both cases, the yield stress shows a strong dependence on temperature. A question has been raised, would the ratio of the yield stress to elastic modulus, σ/G, also depend on temperature? The answer to this question is of significant importance for the theoretical consideration of the mechanism of strain hardening. In the majority of the proposed theories, the only factor dependent on temperature is the elastic modulus and this dependence is linear. Therefore, it should be expected that the ratio σ/G should be independent of temperature. Using the values of Young's modulus of

Temperature in °K	G^{-1}	Temperature in °K	G^{-1}
293·3	4·071	173·2	3·817
273·3	4·024	153·2	3·782
253·2	3·979	143·2	3·764
233·2	3·937	133·2	3·747
213·2	3·894	77·2	3·663
193·2	3·853		

Köster (1948), in the range from liquid nitrogen to room temperature, this ratio, σ/E, is still strongly temperature dependent for polycrystalline material (Sylwestrowicz 1958). For single crystals, the temperature dependence of σ/E is also strong at low temperatures but decreases near room temperature, Cottrell and Stokes (1955). The next question arises, what would be the result if the values of macroscopic elastic moduli are replaced by the elastic moduli measured in a single crystal in the plane and direction of the primary slip? Since all theories of deformation are based on phenomena occurring on atomic dimensions, it is appropriate to use the value of the elastic modulus in the plane of slip. The shear modulus G

in the slip plane, {111}, can be expressed in terms of the three elastic moduli for crystals of cubic symmetry and is

$$G^{-1} = \tfrac{1}{3}[S_{44} + 4(S_{11} - S_{12})].$$

The isothermal elastic moduli, S_{11}, S_{12}, S_{44} have been measured as functions of temperature down to 60°K (Sutton 1953) and the values for G have been calculated as a function of temperature according to the above expression and are given in the table.

Although these values apply to the primary slip plane, the temperature dependence for the secondary slip planes would not be expected to differ appreciably. For room temperature and that of liquid nitrogen, the ratio $G_{\text{R.T.}}{}^{-1}/G_{\text{L.N.}}{}^{-1}$ is equal to 1·11 and is again smaller than would be needed to make the ratio σ/G independent of temperature, as the ratio of $\sigma_{\text{R.T.}}/\sigma_{\text{L.N.}}$ for aluminium is about 0·74.

References.

Cottrell, A. H., and Stokes, R. J., 1955, *Proc. roy. Soc.* A, **233**, 17.
Köster, W., 1948, *Z. Metallk.*, **39**, 1.
Sutton, P. M., 1953, *Phys. Rev.*, **91**, 816.
Sylwestrowicz, W. D., 1958, *Trans. Amer. Inst. min. (metall.) Engrs*, **212**.

The Evolution of Extragalatic Nebulae and the Origin of Metagalactic Radio Emission†

By G. R. Burbidge

Kellogg Radiation Laboratory, California Institute of Technology and Yerkes Observatory, University of Chicago

[Received June 23, 1958]

In a paper bearing this title, Bruce (1958) has attempted to argue that the jet in the elliptical galaxy NGC 4486 (Messier 87) is due to an electric discharge mechanism. His last reference to the observations is to those of Baade and Minkowski (1954). However, it should be pointed out that in 1955 Shklovsky (1955) and others predicted that the jet in M 87 was due to synchrotron radiation in the optical frequency range, in which case it was possible that it would have a high degree of polarization. Following this Baade (1956) with the 200-inch telescope at Palomar detected polarization in the jet amounting in parts to some 40%. Then the author (Burbidge 1956) was able to calculate that the total energy of high energy particles and magnetic field necessary to account for the jet in this way was

† Supported in part by the joint programme of the Office of Naval Research and the U.S. Atomic Energy Commission.

at least of the order of 10^{55} ergs. This theory is the only one able to explain easily the high degree of polarization. It is also generally accepted at the present time that the synchrotron mechanism is the most plausible explanation of the non-thermal radio sources, of which M 87 is one, both inside and outside our Galaxy.

References

Baade, W., 1956, *Ap. J.*, **123**, 550.
Baade, W., and Minkowski, R., 1954, *Ap. J.*, **119**, 215.
Bruce, C. E. R., 1958, *Phil. Mag.*, **3**, 539.
Burbidge, G. R., 1956, *Ap. J.*, **124**, 416.
Shklovsky, I. S., 1955, *Astr. J., Moscow*, **32**, 215.

The Evolution of Extragalactic Nebulae and the Origin of Metagalactic Radio Emission

By C. E. R. Bruce

Electrical Research Association Laboratory

[Received July 8, 1958]

In comment on Dr. Burbidge's letter (Burbidge 1958) I should like to emphasize that my sole purpose in writing my original letter was to point out that the discovery of the 'jet' in NGC 4486 and of its being a radio source, fulfilled a prediction made in 1944 that such 'jets' should exist in nebulae of the type of NGC 4486. I was certainly well aware of Shklovsky's suggestions and of earlier rather similar work of Alfven (Alfven and Herlofson 1950). However, Dr. Burbidge will agree that the great difficulty confronting all such theories, is, as Cowling (1957) and others have emphasized, to account for the magnetic field. As I have pointed out in the E.R.A. Report mentioned in my earlier letter (Bruce 1958), this difficulty would appear to be obviated by the electrical discharge theory.

I should also like to refer to still later work of Woltjer (1958) in Leiden, which has appeared since my E.R.A. Report was written. Shklovsky and many others have drawn attention to the close similarity between the radiation emitted by NGC 4486 and that emitted by the Crab Nebula. In the latter, however, a much more detailed study of the polarization of its light is possible. As a result of such a study Woltjer has shown that the varying directions of the polarization can be accounted for if electric currents flow along the filaments. So that another fourteen year old prediction of mine would seem to be fulfilled.

Furthermore in recent communications (Bruce 1957) I have shown that the magnetic pinch effect in these electrical discharge channels will give rise to relatively high pressures therein and to jets of gas along their length. In the long-period variables and combination-spectra stars the

observed velocities of the hot gas in which the emission lines originate agree with those calculated on this view from the observed temperature of the gas in these stars. The conditions in these two types of stars cover a range of 10 to 1 in velocity, and 100 to 1 in temperature. In accordance with this theory, Woltjer has observed that the filaments of the Crab Nebula are also the sites of jets of gas reaching around 1000 km per second.

References

Alfven, H., and Herlofson, N., 1950, *Phys. Rev.*, **78**, 616.
Bruce, C. E. R., 1957, *Observatory*, **77**, 107, 153; 1958, E.R.A. Report Ref. Z/T117.
Burbidge, G. R., 1958, *Phil. Mag.*, **3**, 1327.
Cowling, T. G., 1957, *Magnetohydrodynamics* (London : Interscience Publishers Ltd.), p. 32.
Woltjer, L., 1958, *Bull. astr. Insts. Netherlds*, **14**, 39.

Measurements of Unit Cell and Physical Dimension Changes of Molybdenum after Neutron Irradiation

By J. Adam and D. G. Martin
Metallurgy Division, Atomic Energy Research Establishment, Harwell

[Received July 22, 1958]

Unit cell and physical dimension changes of molybdenum have been measured after irradiation at 30°C and also after subsequent annealing.

The physical dimension measurements were made on randomly oriented polycrystalline bars $\frac{5}{16}$ in. × $\frac{5}{16}$ in. × 1 in. which had been annealed at 750°C ; the end faces were ground and lapped parallel to one microinch. Changes in sample length were measured to an accuracy of 2 parts per million in a temperature controlled room on a calibrated mechanical comparator (magnification 4500), using unirradiated samples as standards. Specimens were supplied by Johnson Matthey Ltd. and Murex Ltd. Both batches had 0·01% of iron as principal impurity and showed no significant difference in behaviour on irradiation and subsequent annealing.

Unit cell measurements were made on photographs taken in a precision x-ray powder camera (Adam 1954) temperature controlled at 25·5°C. Errors due to non-uniformity of film shrinkage were eliminated by printing an accurate scale on each film before processing. The final value of the unit cell size, which was accurate to about 15 parts per million, was derived using the standard Nelson and Riley (1945) extrapolation. For the powder used (Hopkin and Williams Ltd.†) $a = 3{\cdot}14725 \pm 0{\cdot}00005$ Å assuming the wavelength of copper $K\alpha_1$ radiation equal to 1·54050 Å.

† Irradiation experiments on bars and powders were started independently and materials from different sources were used. No impurities were detectable spectroscopically in the powder.

All samples were irradiated *in vacuo* inside a hollow uranium cylinder in the Harwell reactor BEPO. The irradiation position and the method of neutron dose measurements were the same as Kinchin and Thompson's (1958). In this position the fast and slow neutron fluxes are approximately equal.

Figure 1 illustrates the fractional expansion in unit cell and physical dimensions as functions of the measured slow neutron dose. Each irradiated sample was annealed for one hour at successively higher temperatures and its dimensions measured. The fractional decrease in length obtained from a typical specimen, showing two principal annealing stages at 180°C and 550°C is given in fig. 2. 40% of the original elongation anneals during the first stage and is independent of neutron dose. The fractional decreases in the unit cell expansion measured on a powder annealed for one hour at 200°C and 700°C are approximately the same. Unfortunately the X-ray measurements are an order of magnitude less accurate than those of physical dimensions and therefore the shape of the annealing curve cannot be obtained from them.

An annealing peak at 180°C has been observed by Kinchin and Thompson (1958) who measured the electrical resistivity and stored energy after neutron irradiation, and also during the recovery of the cold worked metal (Martin 1957).

It is possible to estimate the concentration of defects from the observed strain. Tewordt (1958) has shown that the changes in unit cell size of copper for 1% of interstitials and vacancies are $+0{\cdot}6$ and $-0{\cdot}2\%$ respectively. Since a similar value is obtained for vacancies by combining Girifalco and Streetman's (1958) calculations of the relaxation of a vacancy in molybdenum with elasticity theory (Eshelby 1954), it will be assumed that Tewordt's results apply also to molybdenum. The concentration of defects derived from theoretical considerations of radiation damage (Kinchin and Pease 1955) is of the order of a hundred larger than that estimated from the observed expansion after irradiation ; this suggests that at least one fundamental defect is mobile at 30°C. Although caution must be exercised in comparing quantitatively the unit cell and physical dimension changes because of the difference in purity of samples, it can be accepted that the increase in physical dimensions is larger. Since any uniform distribution of defects within the lattice would affect cell dimension and macroscopic changes similarly, to account for the larger macroscopic expansion we must postulate that new lattice sites were formed during irradiation. This could occur if single interstitial atoms possessed a lower activation energy of migration than vacancies. The defects remaining in the lattice after irradiation at 30°C producing unit cell expansion are thus either interstitials trapped by impurity atoms or clusters of interstitials. The depths of the traps or the sizes of clusters are probably not identical because of the wide range of temperature over which annealing takes place. The annealing peak at 180°C can be attributed to a particular trap depth or cluster size distribution or

Fig. 1

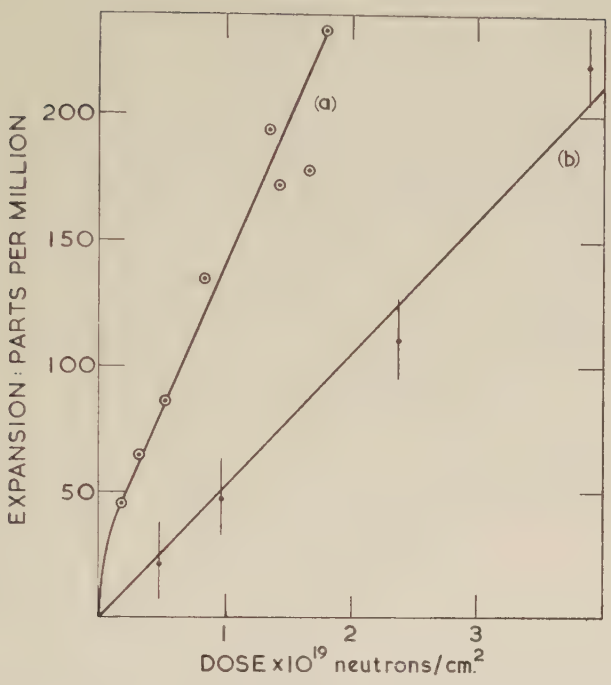

The fractional increase in (*a*) length and (*b*) unit cell size as a function of neutron dose.

Fig. 2

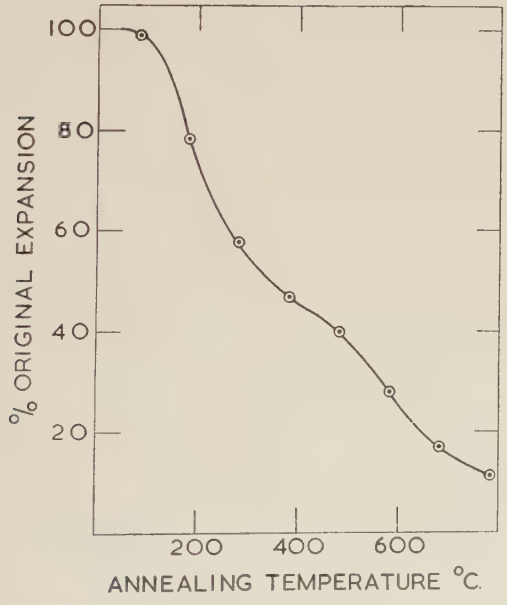

The fractional decrease in length on annealing as a function of temperature. Original expansion = 170 p.p.m.

alternatively the annealing process may be accelerated by vacancy movements if these become appreciable at about 180°C.

References

Adam, J., 1954, *J. sci. Instrum.*, **31**, 131.
Eshelby, J. D., 1954, *J. appl. Phys.*, **25**, 255.
Girifalco, L. A., and Streetman, J. R., 1958, *J. phys. chem. Solids*, **4**, 182.
Kinchin, G. H., and Pease, R. S., 1955, *Rep. Progr. Phys.*, **18**, 1.
Kinchin, G. H., and Thompson, M. W., 1958, *J. nucl. Energy*, **6**, 275.
Martin, D. G., 1957, *Acta Met.*, **5**, 371.
Nelson, J. B., and Riley, D. P., 1945, *Proc. phys. Soc. Lond.*, **57**, 160.
Tewordt, L., 1958, *Phys. Rev.*, **109**, 61.

The Properties of Beryllium-11

By D. E. Alburger and D. H. Wilkinson‡
Brookhaven National Laboratory, Upton, New York

[Received August 21, 1958]

Ajzenberg and Lauritsen (1955) suggested that the energy difference between the ground states of ^{11}Be and ^{11}B should be about 11·5 Mev and that ^{11}Be should therefore be stable by about 0·5 Mev against neutron emission. In this case the Q-value for the reaction ^{11}B(n, p)^{11}Be would be about $-10{\cdot}7$ Mev. Nurmia and Fink (1958) discovered a beta-activity of half-life $14{\cdot}1 \pm 0{\cdot}3$ seconds induced in boron by the 14 Mev DT neutrons and ascribed it to ^{11}Be. We have studied this body, made in the same way. We have confirmed its assignment to ^{11}Be and have determined certain properties of the decay. The work was carried out, using NaI(Tl) and plastic scintillation detectors both singly and in coincidence and the measurements are presented briefly in the table.

The energies of the ^{11}B states in the first column are taken from the literature (Ajzenberg and Lauritsen 1955). The entry " % betas " gives the percentage of all ^{11}Be beta-decays that take place to the ^{11}B state in question. " % gammas " gives the abundance of the various gamma-rays per ^{11}Be decay. The half-life entered for the ground state was measured on beta-particles of energy greater than 3·0 Mev. That for the 2·14 Mev state was measured on the gamma-rays from that state. The third half-life quoted was measured on all gamma-rays of greater than 3·0 Mev. The closeness of these half-lives and the agreement between our measured gamma-ray energies (fifth column) and the known energies of the various states of ^{11}B confirm the assignment of the activity to ^{11}Be. We combine these measurements to give an average half-life of $13{\cdot}57 \pm 0{\cdot}15$ sec. Our

† Work performed under the auspices of the U.S. Atomic Energy Commission.
‡ Permanent address : Clarendon Laboratory, Oxford University, Oxford, England.

various measured beta-particle transition energies (second column) may be combined with the known energies of the ^{11}B states to yield : $^{11}\text{Be} - ^{11}\text{B} = 11{\cdot}48 \pm 0{\cdot}15$ MeV which corresponds to a mass defect for ^{11}Be : $M - A = 23{\cdot}39 \pm 0{\cdot}15$ MeV.

The log *ft* values of the various beta-ray decay branches are rather large but those leading to the 6·76 and 7·99 MeV states probably indicate allowed transitions. The parity of the former state is probably odd (Cox and Williamson 1957) which gives odd parity for ^{11}Be if indeed the transition leads to that state but of this we cannot be sure from our data. The beta-decay to the $\frac{5}{2}-$ state at 4·46 MeV is strongly forbidden while transitions to the $\frac{3}{2}-$ ground state and $\frac{1}{2}-$ state at 2·14 MeV are considerably faster although still surprisingly slow for allowed transitions. This suggests $J = \frac{1}{2}-$ for ^{11}Be which is as expected from its position in the 1p-shell.

B state (MeV)	E_β (MeV)	% betas	log *ft*	E_γ (MeV)	% gammas	Half-life (sec)
	$11{\cdot}48 \pm 0{\cdot}15$	61	6·77	—	—	$13{\cdot}68 \pm 0{\cdot}15$
·138	$9{\cdot}32 \pm 0{\cdot}15$	29	6·63	$2{\cdot}121 \pm 0{\cdot}010$	32	$13{\cdot}47 \pm 0{\cdot}20$
·459	—	$\leqslant 0{\cdot}2$	$\geqslant 8{\cdot}2$	—	—	
·034	—	$\leqslant 0{\cdot}2$	$\geqslant 8{\cdot}2$	—	—	
·758	$4{\cdot}65 \pm 0{\cdot}2$	6·5	5·93	(i) $6{\cdot}76 \pm 0{\cdot}03$ (ii) $4{\cdot}64 \pm 0{\cdot}02$	4·4 2·1	
·808	—	—	—	—	—	
·298	—	$\leqslant 1{\cdot}5$	$\geqslant 6{\cdot}4$	—	—	$13{\cdot}48 \pm 0{\cdot}20$
·987	$3{\cdot}6 \pm 0{\cdot}2$	4·1	5·53	(i) $7{\cdot}97 \pm 0{\cdot}03$ (ii) $5{\cdot}86 \pm 0{\cdot}04$	1·7 2·4	
·568	—	$\leqslant 0{\cdot}3$	$\geqslant 6{\cdot}3$	—	—	
·927	—	$\leqslant 0{\cdot}15$	$\geqslant 6{\cdot}3$	—	—	

Although the speed of the two beta transitions of highest energy may suggest first-forbidden transitions (even parity for ^{11}Be) the strong relative discouragement of the transition to the 4·46 MeV state argues against this. It seems most likely that ^{11}Be is $J = \frac{1}{2}-$ and that we have two rather retarded allowed transitions whose theoretical analysis should be very interesting in view of the fact that the independent-particle model wave functions are fairly well known in this region (Kurath 1956).

We have considered the possibility that the 13·6 sec period belongs to an isomeric state in ^{11}Be but we have found no evidence for this in a search for low-energy gamma-rays accompanying the decay.

We would like to thank Mr. Stuart Crampton for his help.

References

Ajzenberg, F., and Lauritsen, T., 1955, *Rev. mod. Phys.*, **27**, 77.
Cox, S. A., and Williamson, R. M., 1957, *Phys. Rev.*, **105**, 1799.
Kurath, D., 1956, *Phys. Rev.*, **101**, 216.
Nurmia, M. J., and Fink, R. W., 1958, *Phys. Rev.*, **1**, 23.

REVIEWS OF BOOKS

Biophysical Chemistry. Volume I. 'Thermodynamics, Electrostatics and the biological significance of the properties of matter.' By J. T. Edsall and J. Wyman. (Academic Press 1958.) £5.

A textbook such as the present one must first be judged by the quality of its treatment of certain of the basic principles of physical chemistry. Edsall and Wyman are to be congratulated on producing a book which could well serve as a standard text for advanced undergraduates on thermodynamics and the properties of ionic solutions. The greatest care has been taken in presenting the physical ideas which motivate the choice of mathematical methods. Only in the use of Caratheodory's rather than a more elementary treatment of the second law of thermodynamics is the reader's understanding of abstract mathematics tested more than is absolutely necessary.

By the clever choice of examples the authors have succeeded in introducing so much material dealing with the properties amino acids, peptides, polyphosphates, etc., that the sections on the physical chemistry of electrolytes also form a detailed introduction to this aspect of biophysics. This material taken together with the chapters on the constitution and structure of biological materials make up an excellent introduction to the more biological parts of the subject.

This book can be wholeheartedly recommended both to students and to biologists who wish to brush up their physical chemistry. L. E. O.

Electric Conduction in Semiconductors and Metals. By W. Ehrenberg. (Oxford: Clarendon Press). [Pp. 389.] 63*s*.

This is mainly about semiconductors. The first half derives the electrical transport properties of solids, first in the mobility approximation and then more rigorously from the Boltzmann equation. The properties of actual semiconductors are then summarized. The final chapters give the theory of rectification and transistor action. Although there is a good deal of mathematics it is all relatively elementary, and should easily be followed by physicists working on semiconductor devices. Perhaps Chapter 7 is a little too heavy: the brute-force solution of the Bloch integral equation is extremely complicated to explain, and has little direct physical significance. Also, it is surprising that the concept of 'deformation potential' is not mentioned. The book as a whole will be useful for the careful detailed derivation from first principles of a number of standard formulae, and for the discussion and clarification of various difficult points which are not adequately treated elsewhere. J. M. Z.

A History of Mathematics. By J. F. Scott. (London: Taylor & Francis, Ltd.) [Pp. x+266, with six plates.] 3 guineas.

Dr. Scott now follows his specialist works on seventeenth century mathematics with a general survey of the history of mathematics from its beginnings to the early nineteenth century.

For such a task the first requisite of the author is a sound knowledge of the literature, particularly as it affects the periods with which he is least familiar. Unfortunately, this knowledge Dr. Scott does not always possess. His bibliography includes the great classics of Montucla and Cantor, but it omits most of the important modern works on the history of mathematics. In some fields these modern works have compelled a revision of earlier views, and

accounts based on earlier books are no longer acceptable. This is particularly the case with Babylonian mathematics, a field in which exciting developments have taken place in recent decades. Dr. Scott takes the surprising course of quoting the work of the man chiefly responsible as reported in a textbook for undergraduate mathematicians, and he pays the penalty.

On Dr. Scott's home ground of the seventeenth century, and on topics where recent research has added little of importance, this book is of value. Elsewhere it must be used with caution. M. A. H.

Dislocations and Mechanical Properties of Crystals. By J. C. Fisher, W. G. Johnston, R. Thomson and T. Vreeland Jr. (New York: John Wiley & Sons, Inc.; London: Chapman & Hall.) [Pp. xiv+634.] 120*s*.

This book describes the proceedings of an International Conference on dislocations held at Lake Placid in September 1956. The Conference was organized by the U.S. Air Force Office of Scientific Research, the Air Research and Development Command and the General Electric Research Laboratory, and covered eight main fields.

It is not possible in a short review to do more than indicate a few general impressions. One notes, on one hand, the elegant and beautiful experimental techniques that have been developed in recent years to observe directly the presence of dislocations; on the other, the underlying theoretical uncertainty as to whether these techniques do, in fact, always reveal the most relevant dislocations. Secondly one is impressed by new theoretical mechanisms that continue to be elaborated in an attempt to explain more adequately such problems as work-hardening, yield-point phenomena and the effect of reversed stresses. Thirdly one is struck by those areas in which dislocation theory appears to provide a remarkably successful synoptic explanation of a whole class of experimental phenomena, such as Lücke and Granato's work on internal friction. But chiefly there remains the impression of a Conference in which the participants discussed freely and openly their own and each other's ideas. If for no other reason the editors are to be congratulated on conveying so effectively an atmosphere of vigorous and thought-provoking discussions. As a result they have produced an account of recent advanced experimental and theoretical studies in the field of dislocations that is both authoritative and stimulating. D. T.

Mass Spectroscopy. By Henry E. Duckworth. (Cambridge: University Press, 1958.) [Pp. ix+206.] 35*s*.

In the past decade mass-spectrometers have been incorporated in many kinds of apparatus used to study phenomena which depend on atomic or molecular mass. In nuclear physics, for example, the masses of stable and radioactive isotopes, neutron absorption cross sections, fission yields and nuclear moments have been studied. Chemical and biological processes are more easily interpreted when isotopic abundances are measured, and these also play an important rôle in geological dating. The possibility of mass analysis of reaction products has led to great advances in molecular physics and the understanding of dissociation processes and chemical reactions.

This monograph contains a concise description of two aspects of mass-spectrometry, firstly, the design and operation of different types of instrument, and secondly, the application to various fields of research and measurement. The first six chapters are concerned with the design principles, the ways of obtaining sufficient resolution and intensity, and the techniques used for the production and detection of the ion beams. No attempt is made to cover the engineering, electronic and vacuum technology. The remaining five chapters

are devoted to the determination of atomic masses and isotopic abundances, applications in nuclear physics, the study of ionization and dissociation of molecules under electron bombardment and finally, applications to geology. Tables of isotopic abundances are included, and there is a generous bibliography. The book gives a very good indication of the sort of research which is possible when a mass-spectrometer is included in the apparatus and typical modern instruments are described in ample detail. K. S.

Atomic Physics and Human Knowledge. By Niels Bohr. (New York : John Wiley & Sons, Inc.) [Pp. 101.] $3.95.

This collection of articles, extending over the years 1932–57, is a ' theme with variations ' on the principle of complementarity. Although only one of the essays attempts anything like a systematic treatment (Bohr's discussions with Einstein) their main interest lies perhaps in the evidence they yield of the repeated attempts of the author to arrive at a clearer statement of the complementary idea (cf. pp. 6, 19, 25, 39, 60, 72, 90, 99). This is said to " symbolise the fundamental limitation, met with in atomic physics, of the objective existence of phenomena independent of the means of their observation " (p. 7). Elsewhere it is a " consistent generalisation of the idea of causality " (p. 27); or again, it " characterises " the " mutual exclusion " of certain experimental procedures designed, e.g. to measure spatio-temporal *and* momentum or energy aspects, (p. 61). The principle, then, draws our attention to certain incompatibilities. Does it do more than this ? By 1955 a still sharper definition is adopted: the mutual exclusiveness of certain experimental situations stems from the " very definition " of the clocks and measuring rods adopted (p. 90). However, even here the complementary principle only tells us that this exclusiveness " *must be termed* complementary . . . . " (*Ibid.*, my italics).

Bohr also attempts to apply the complementarity idea to the spheres of biology, psychology and cultural history. Here he seems less sure, and it is indeed questionable whether analogies suggested by the *term* complementarity are relevant to the extension of the *concept* beyond the ground of quantum mechanics. Thus, in the free-will controversy, man as actor and as object are hardly complementary aspects in the quantum sense. And in the biological sphere, the theory that complementarity applies to the organism as a living and as a dead object of study is based on the weak analogy of some sort of limitation of investigation as a feature shared with the physical situation.

Gerd Buchdahl.

[The Editors do not hold themselves responsible for the views expressed by their correspondents.]

Fig. 1

(*a*)

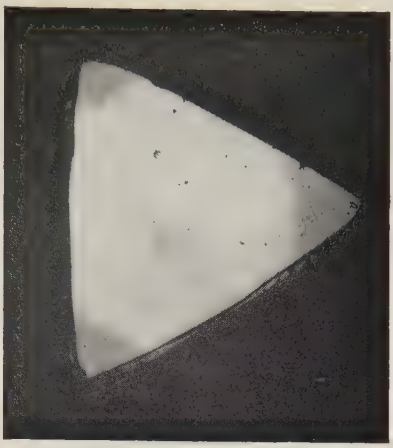

(*b*)

(*c*)

(*a*), (*b*): opposed faces of a ' blue-white ' octahedral diamond;
(*c*) birefringent region within this diamond, seen through face (*a*).

Fig. 2

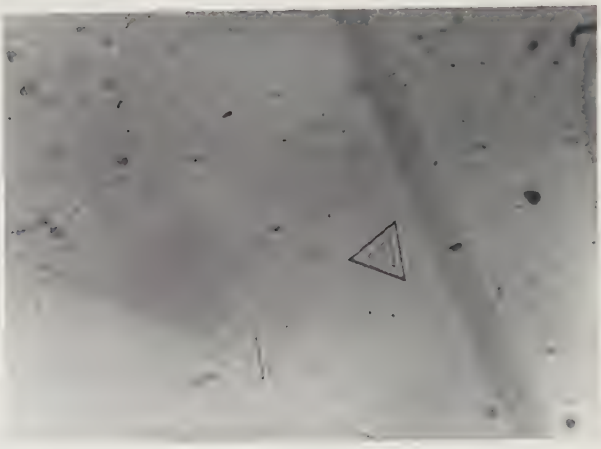

Central area of fig. 1 (*a*)—normal photomicrograph.

Fig. 3

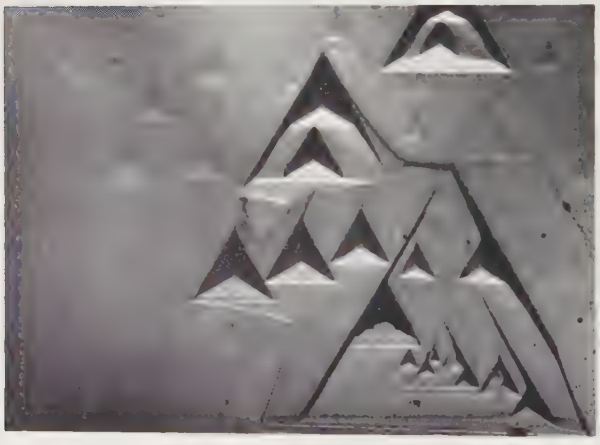

Central area of fig. 1 (*a*)—' schlieren ' illumination.

Original magnification ×160; these two figures are reduced by one-half.

Fig. 1

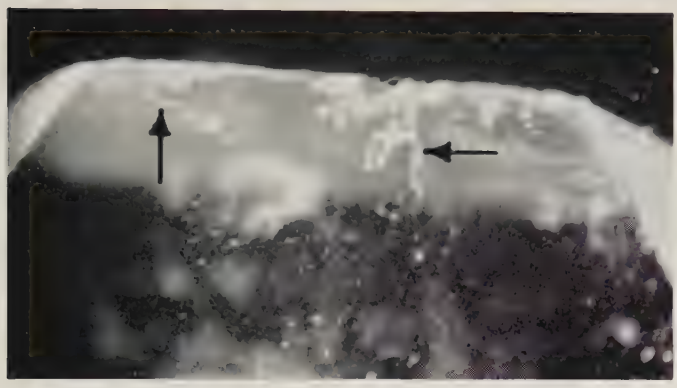

(*a*) Below upper face.

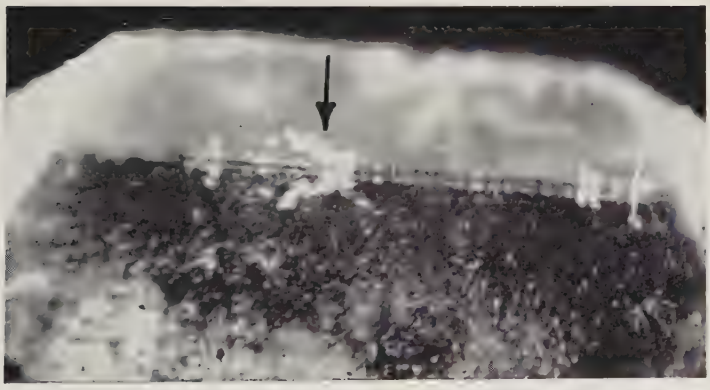

(*b*) Originating from lower edge. (The reflections of tunnels can be seen in the adjacent octahedral face.)

Tunnels (indicated by arrows) penetrating into a diamond etched in wet hydrogen at 820°C. ×20.

Fig. 2

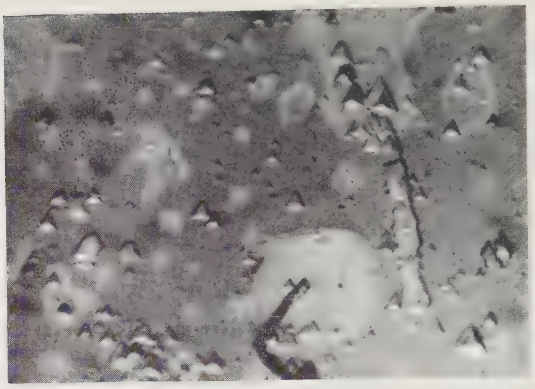

(*a*)

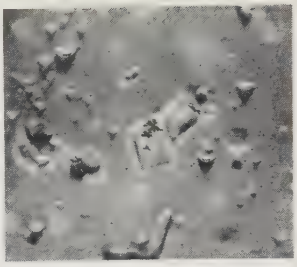

(*b*)

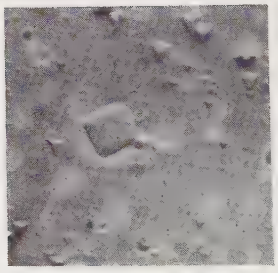

(*c*)

(*d*)

(*a*)–(*c*) Diamond etched in chlorine with trace of oxygen at 800°C. (*a*) Pyramidal and flat-bottomed pits. ×1700. (*b*) and (*c*) Apparently non-crystallographic features. ×1700. (*d*) A similar feature to (*b*) and (*c*) observed on an unetched octahedron. Electron micrograph. ×7500.

Fig. 3

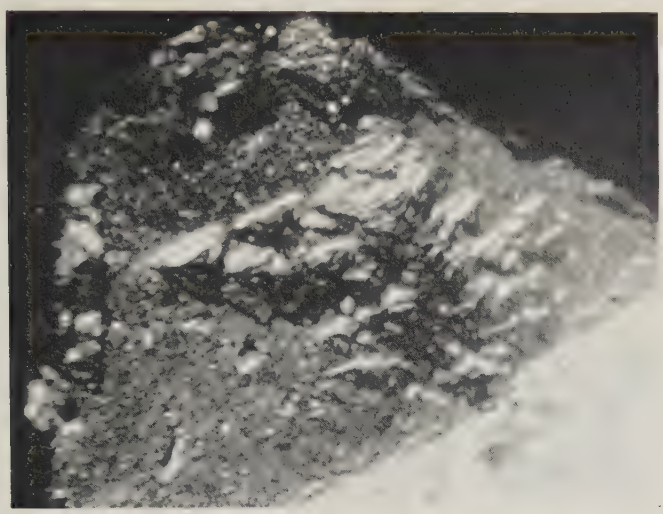

Pits in trigon orientation etched in blue ground at about 1450°C. (Surface layer of graphite also present.) ×50.

Fig. 4

Pits in trigon orientation etched in blue ground at about 1450°C. ×420. Dark ground illumination.

Fig. 5

Bottom of deep pits etched in blue ground. ×280. Dark ground illumination.

Fig. 3

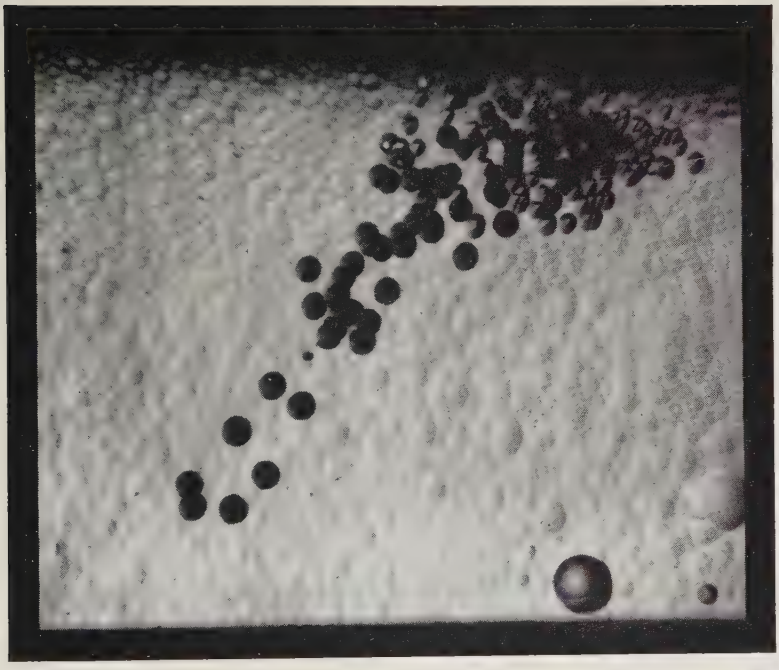

A typical avalanche in InSb ($\overline{1}\overline{1}\overline{1}$) face. $\times 130$.

Fig. 1

Pattern from silver iodide. This pattern is common to both cubic—[211] azimuth—and hexagonal—[11.0] azimuth—silver iodide.

Fig. 2

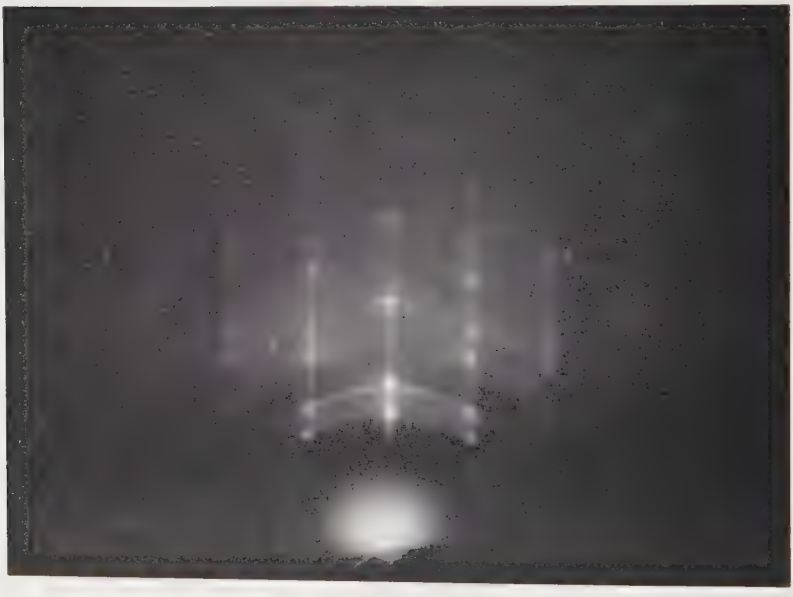

Pattern from a mainly cubic deposit of oriented silver iodide, [1$\bar{1}$0] and [110] azimuths.

Fig. 3

Pattern from hexagonal ice—[1$\bar{1}$.0] azimuth—oriented on silver iodide. Glancing angle of incidence of electron beam, 1·6°.

Fig. 5

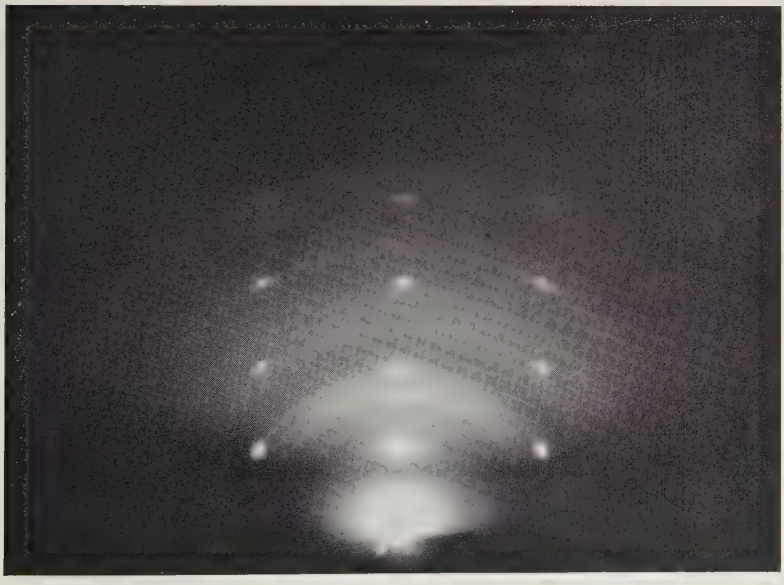

Pattern from hexagonal ice, [1$\bar{1}$.0] azimuth. The underlying silver iodide has been obscured by the ice deposit. Glancing angle of incidence, 0·8°.

Fig. 1

×50

Fig. 2

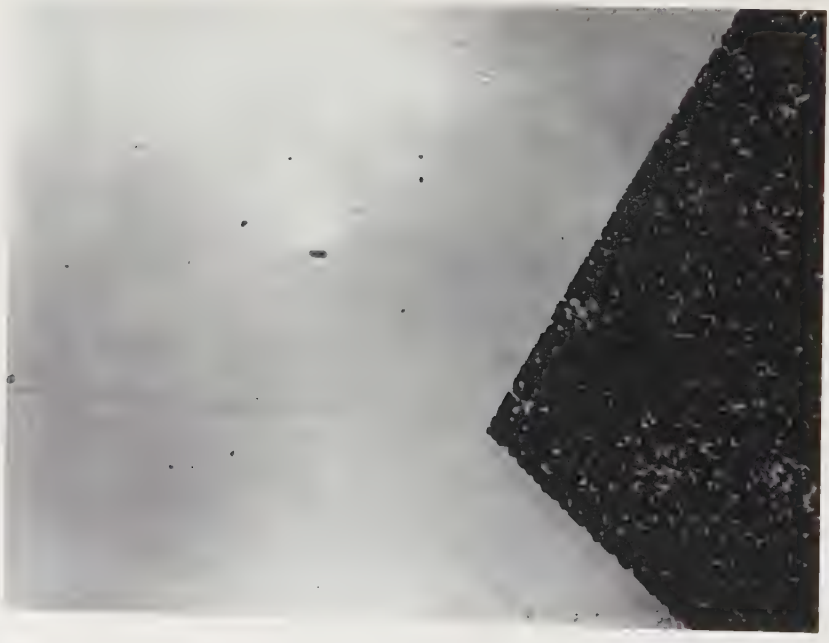

×255

Fig. 3

×3500

Fig. 4

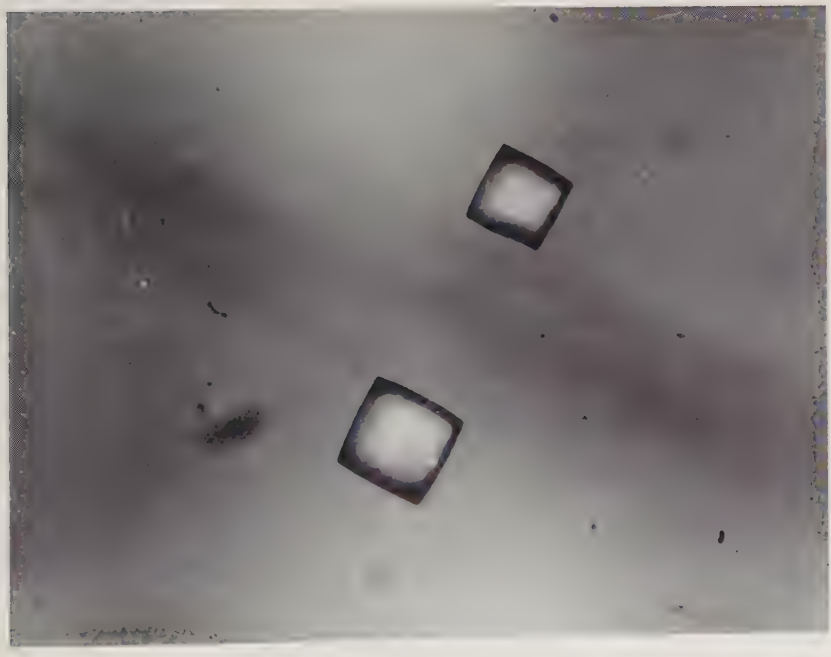

×3500

Fig. 5

×240

Fig. 6

×50

Fig. 7

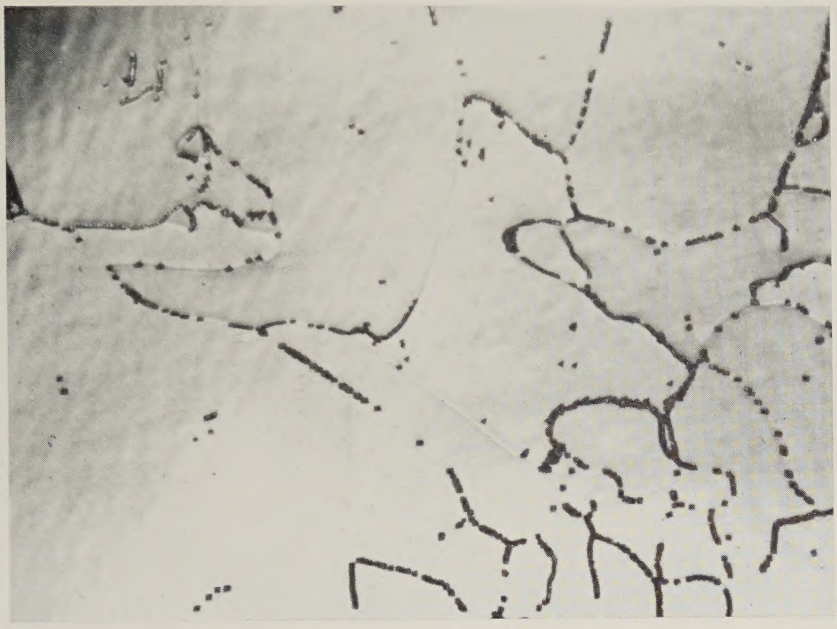

×50

Fig. 8

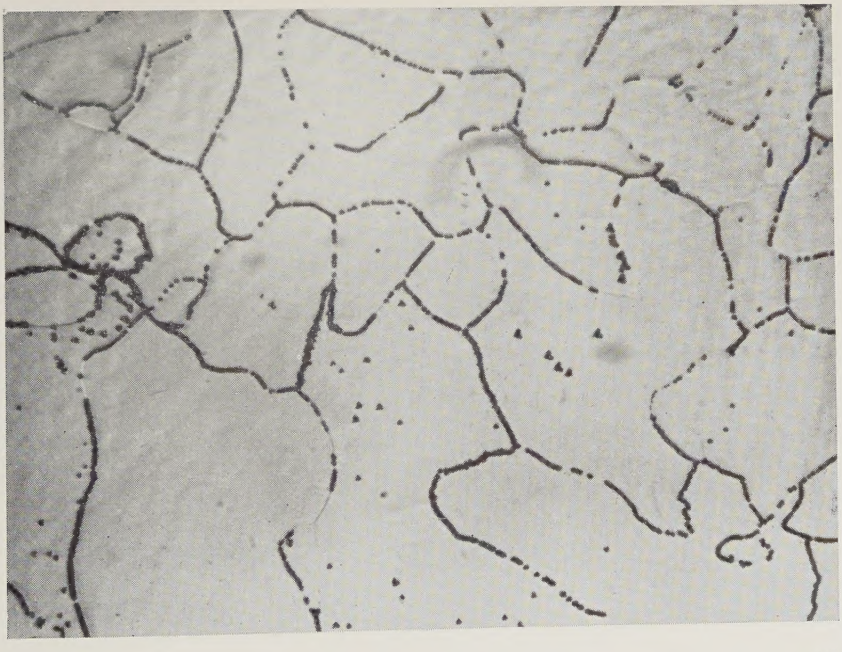

×50

Fig. 9

×50

Fig. 10

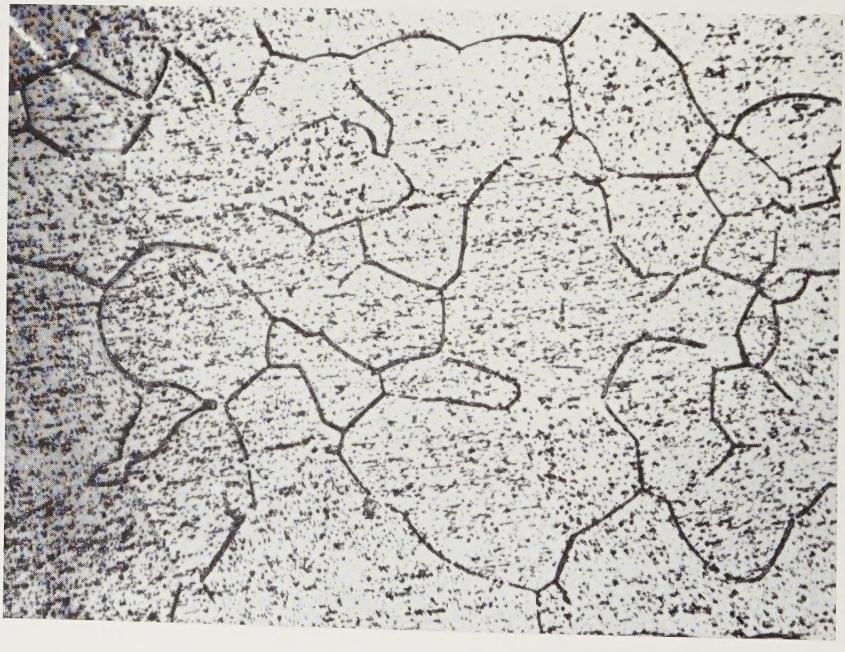

×50

Fig. 11

×50

Fig. 12

×50

Fig. 2

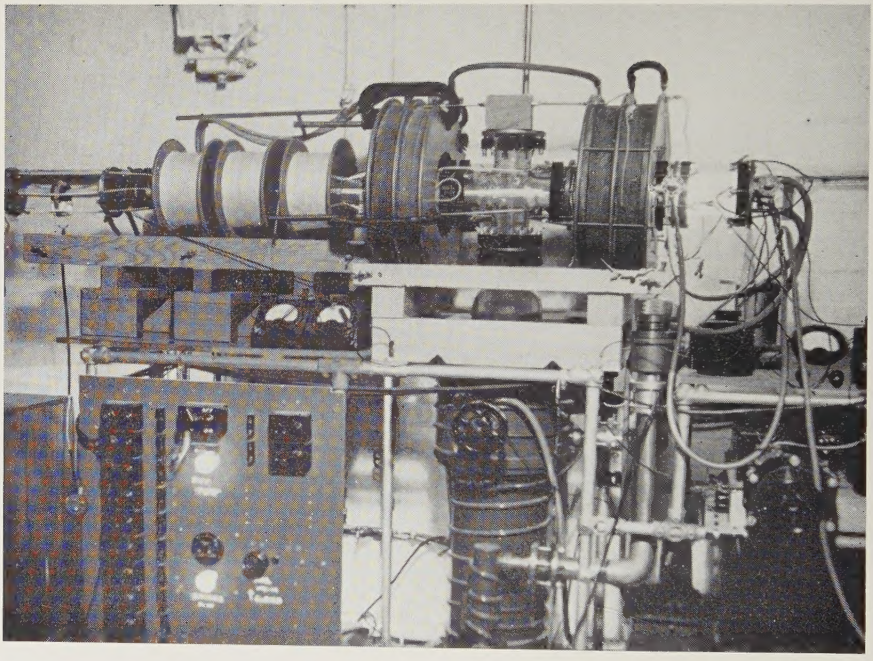

Photograph of a continuously running low energy beam.